

UNIVERSIDAD DE VALPARAÍSO

DOCTORAL THESIS

The origin of Brown Dwarfs

Author:

Alejandro Santamaría
Miranda

Supervisor:

Dr. Itziar de
Gregorio-Monsalvo
Dr. Adele Plunkett
Dr. Matthias R. Schreiber

*A thesis submitted in fulfillment of the requirements
for the degree of Doctor of Astrophysics
in the Instituto de Física y Astronomía*

September 3, 2019

Declaration of Authorship

I, Alejandro Santamaría Miranda, declare that this thesis titled, “The origin of Brown Dwarfs” and the work presented in it are my own. I confirm that:

- This work was done wholly or mainly while in candidature for a research degree at this University.
- Where any part of this thesis has previously been submitted for a degree or any other qualification at this University or any other institution, this has been clearly stated.
- Where I have consulted the published work of others, this is always clearly attributed.
- Where I have quoted from the work of others, the source is always given. With the exception of such quotations, this thesis is entirely my own work.
- I have acknowledged all main sources of help.
- Where the thesis is based on work done by myself jointly with others, I have made clear exactly what was done by others and what I have contributed myself

Signed:

Date:

“It’s a dangerous business, Frodo, going out your door. You step onto the road, and if you don’t keep your feet, there’s no knowing where you might be swept off to.”

J.R.R. Tolkien

“A reader lives a thousand lives before he dies. The man who never reads lives only one.”

George R.R. Martin

UNIVERSIDAD DE VALPARAÍSO

Abstract

Facultad de Ciencias

Instituto de Física y Astronomía

Doctor of Astrophysics

The origin of Brown Dwarfs

by Alejandro Santamaría Miranda

In the present thesis we study the problem of the formation of brown dwarfs, objects whose masses are in the range between planets and stars. There are four main formation theories for these substellar objects: turbulent fragmentation, disk fragmentation, ejection from filaments and photoevaporation. All these formation channels can form brown dwarfs but it remains an open question which is the one preferred by nature. Revealing this dominant formation mechanism was the main motivation of this thesis. In particular, we investigated if mass loss or accretion processes are a scaled-down versions of the same phenomena in the stellar regime.

We used several astronomical techniques such as interferometry and spectroscopy at different wavelengths to study the formation of brown dwarfs. For our observational surveys of forming brown dwarfs the star forming region of Lupus and ρ Ophiuchus were chosen as their close distance and their youth enhance the possibilities of detecting and analysing faint objects.

For objects in the earliest stages of their evolution we used ALMA for studying the cold dust envelopes which emit the released energy in the (sub)mm regime. ALMA was also used for the somewhat more evolved Class 0 and I sources, complemented with optical and infrared archival data. In one Class I/II source (Par-Lup3-4) we have used the emission of several molecular transitions to study the mass loss of a molecular outflow. We combined the ALMA emission line and continuum data with optical/infrared archival data. The further evolved Class II sources were studied using spectroscopic observations ranging from near ultraviolet to near infrared wavelengths as well as continuum emission in the (sub)mm and optical/infrared photometry. The most notable observational result is the discovery of eleven pre-substellar core candidates that are in gravitational contraction. We found an interesting Class 0/I candidate and resolved its structure. We measured the disk mass of the Class II sources and their properties are consistent with being scaled down versions of forming low mass stars.

We detected for the first time the base of a bipolar molecular outflow in a very low mass star whose properties are a scaled-down version of the outflow properties observed in the stellar regime.

We measured the accretion rate of the substellar companion to the stellar binary (SR 12) using several accretion indicators commonly used in the stellar regime. The companion's radial velocity and its separation within the binary system point out that it is not very probable that this source was formed by disk fragmentation, while the accretion rate is in agreement with an extension of the relation obtained for more massive objects.

Based on the mentioned scientific evidences (accretion rate, mass loss, the presence of isolated pre-substellar cores in gravitational contraction, and the relation between disk mass and central object) we conclude that it is highly probable that the main formation mechanism of brown dwarfs is turbulent fragmentation (also known as scaled-down version of star formation).

Resumen

En la presente tesis abordamos el problema de la formación de las enanas marrones, objetos cuya masa se encuentra a medio camino entre los planetas y las estrellas. Hay cuatro teorías principales de formación de objetos subestelares: fragmentación turbulenta, fragmentación en el disco, eyección y fotoevaporación. Actualmente todos estos mecanismos de formación pueden dar lugar a objetos subestelares pero nos es desconocido cual de todos ellos es el más eficiente. La principal motivación de esta tesis es sin duda conocer cual de los mencionados mecanismos es el dominante. Además, también nos preguntamos si características como la acreción o la pérdida de masa se encuentran menguadas respecto a los mismos fenómenos en el régimen estelar.

Para abordar este problema hemos utilizado diferentes técnicas astronómicas como son la interferometría y la espectroscopía en distintas longitudes de onda, así hemos podido cubrir los diversos aspectos evolutivos de la formación de las enanas marrones y de las estrellas de muy baja masa. Se escogió estudiar todos estos objetos en las regiones de formación estelar de Lupus y ρ Ophiuchus, que por su cercanía y juventud aumentaban las probabilidades de éxito de detectar y analizar estos objetos tan débiles.

Para los objetos en el estadio evolutivo más temprano hemos utilizado imágenes de polvo en el régimen (sub)milimétrico tomadas con el interferómetro ALMA, que es donde se encuentra el máximo de emisión. Para los objetos de Clase 0 y I utilizamos de nuevo ALMA para estudiar el polvo y complementamos estos datos con observaciones de archivo en el óptico e infrarrojo. En un objeto de Clase I/II (Par-Lup3-4) hemos utilizado la emisión de diferentes transiciones moleculares para estudiar los flujos moleculares que producen la pérdida de masa, complementando estas observaciones con datos del polvo en el milimétrico y telescopios ópticos e infrarrojos. Por último, para los objetos más evolucionados de Clase II hemos usado observaciones espectroscópicas en el ultravioleta e infrarrojo cercano así como en el visible para finalmente complementar estos resultados con datos del polvo en el submilimétrico. Entre los resultados principales hemos encontrado un total de once nuevos candidatos a núcleos pre-subestelares que están en contracción gravitacional. Hemos encontrado un interesante candidato de Clase 0/I cuya estructura resolvemos y de naturaleza muy posiblemente galáctica.. Además, hemos medido la masa de los discos de Clase II de enanas marrones y hemos encontrado que siguen las propiedades de las estrellas de baja masa escaladas al régimen subestelar.

Hemos detectado por primera vez la base de un flujo molecular en una estrellas de muy baja masa cuyas propiedades son una versión reducida de las propiedades esperadas en estrellas de baja masa.

Hemos medido la acreción de forma exhaustiva en una enana marrón compañera (SR 12 C) de un sistema binario usando los indicadores de acreción que se emplean para estrellas de baja masa. La velocidad radial y su posición en el sistema nos indican que es muy poco probable que se haya formado por fragmentación del disco protoplanetario y en cambio la tasa de acreción parece que está disminuida respecto a la acreción en estrellas.

Basándonos en las pruebas mencionadas anteriormente (acreción, pérdida de masa, la presencia de núcleos pre-subestelares en contracción y la relación entre masa de los discos y del objeto central) concluimos que el mecanismo de formación dominante es muy probable que sea la formación turbulenta.

Contents

Declaration of Authorship	iii
Abstract	vii
1 Introduction	1
1.1 The discovery of brown dwarfs: theory and observations	1
1.2 Brown dwarf formation theories	3
1.2.1 Gravoturbulent fragmentation	4
1.2.2 Photoevaporation (photo-erosion by nearby massive stars)	5
1.2.3 Dynamical ejection (ejection from multiple systems)	5
1.2.4 Disk fragmentation (ejection from fragmented disks)	6
1.3 Observational evidence	10
1.3.1 Earliest stages (Pre- and proto-BDs)	10
Searches based on sky surveys	11
Submillimetre mapping observations	13
1.3.2 Brown dwarf disks: accretion and outflows	14
Magnetospheric accretion	16
Molecular outflows	17
1.4 Motivation, goal and outline of this thesis	18
1.4.1 Motivation	18
1.4.2 Goal	19
1.4.3 Outline	20
2 The early stages of substellar formation in Lupus 1 and 3 clouds with ALMA	21
2.1 Introduction	21
2.2 Observations	23
2.2.1 AzTEC observations	23
2.2.2 Ancillary data	24
2.2.3 The sample	25
2.2.4 ALMA observations	25
2.2.5 Distances	27
2.3 Results	30
2.3.1 ALMA continuum detections	30
2.3.2 ALMA: Gas emission detections	33
2.3.3 ALMA: Mass estimates	33
2.3.4 AzTEC: Size and mass estimates	35
2.3.5 Spectral energy distribution	40
Optical/IR/Radio counterpart association	40

	Bolometric luminosity and temperature	40
	Classification	42
2.3.6	ALMA sources without optical/IR counterparts	42
2.3.7	ALMA sources with counterparts	43
	ALMA J153914.996-332907.62	43
	ALMA J154229.778-334231.86	44
	160658.7 -390405	44
	160826.8 -384101	44
	V*V1094 Sco	45
	Lup706	45
	Par-Lup3-4	45
	SONYC-lup3-7	46
2.3.8	VeLLOs	46
2.4	Discussion	46
2.4.1	Spatial distribution: detections vs non-detection	46
2.4.2	Detection rate of pre- and proto-BD candidates and large scale core properties	46
2.4.3	Evolution of the AzTEC starless cores: Final mass of the pre-BD candidates	47
2.4.4	Nature of ALMA detections without infrared counterparts	47
	Infall according to turbulent fragmentation	47
	r^{-2} density profile	52
2.4.5	The nature of J154229.778-334231.86	53
2.4.6	Disk masses	54
2.4.7	Is the formation of BDs a scaled-down version of the low mass star formation?	58
2.5	Conclusions	58
3	The bipolar molecular outflow of the very low-mass star Par-Lup3-4: Evidence for scaled-down low-mass star formation	61
3.1	Introduction	61
3.2	Previous observations of Par-Lup3-4	63
3.3	Observations	64
3.3.1	ALMA observations	64
3.4	Results	65
3.4.1	Continuum emission	65
3.4.2	Gas emission lines	66
	CO(2-1)	66
	CO(3-2)	70
	^{13}CO (3-2)	71
3.4.3	Outflow geometrical and dynamical properties	74
3.5	Discussion	77
3.5.1	Spectral index	77
3.5.2	A possible secondary molecular outflow?	78
3.5.3	SED Fitting	79
3.5.4	Characterizing the molecular outflow cavity	83
3.5.5	VLMs as a scale down version of low-mass?	85

3.5.6	Revealing the true nature of Par-Lup3-4	86
3.6	Conclusions	87
4	Accretion signatures in the X-shooter spectrum of the substellar companion to SR 12	89
4.1	Introduction	89
4.2	Observations	91
4.3	Characterizing SR 12 C	91
4.3.1	Fitting model templates	92
4.3.2	Observational template fitting	93
4.3.3	Radial velocity measurements	95
4.3.4	Identification of absorption lines	95
4.4	Accretion	95
4.4.1	Accretion estimated from $H\alpha$ emission	97
4.4.2	Accretion measured with the Ca II triplet	98
4.4.3	Accretion rate based on Paschen β	101
4.4.4	Accretion rate based on the OI line	101
4.4.5	Accretion rates derived from other Hydrogen lines	102
4.5	Discussion	102
4.6	Conclusion	104
5	General conclusions and future work	107
5.1	General conclusions	107
5.2	Future work	109
A	Lupus 1 and 3 survey: ALMA detections and non detections	111
B	Flux and wavelength for each source in the Lupus sample	115
C	AzTEC images of the Lupus sample	121
D	Equivalent width of photospheric features in SR 12 C	125

List of Figures

1.1	Low mass star formation stages	4
1.2	Photoevaporation a prestellar core	6
1.3	Dynamical ejection	7
1.4	Disk fragmentation	8
1.5	Disk fragmentation predictions	9
1.6	Color-color diagram	12
1.7	SED of a Class 0 protobrown dwarf	13
1.8	LABOCA Chameleon II region	14
1.9	ALMA cores without presubstellar counterparts	15
1.10	Pre-transitional Brown Dwarf Disk	16
1.11	Scheme of magnetospheric accretion	17
1.12	Bipolar outflow scheme	18
2.1	AzTEC maps of Lupus 1 and 3	26
2.2	Herschel temperature map of Lupus 1 and 3	26
2.5	ALMA continuum images of the Lupus 1 and 3 sample	33
2.6	ALMA continuum images of the Lupus 1 and 3 sample with two sources inside the ALMA primary beam	34
2.7	Spectral Energy Distribution of the Lupus 1 and 3 sample	37
2.8	Mass estimates of the Lupus 1 and 3 sample	38
2.9	Bolometric luminosity versus bolometric temperature of the Lupus 1 and 3 sample	41
2.10	Mass of the ALMA sample pre-substellar candidates in the Lupus sample	48
2.11	Turbulent fragmentation predictions for the pre-substellar candidates in Lupus	51
2.12	r^{-2} density profile of the pre-substellar candidates	53
2.13	SED J154229	54
2.14	Disk mass versus central object mass of the all the ALMA Class II BDs	57
3.1	ALMA continuum images of Par-Lup3-4 at 1.3 mm	66
3.2	ALMA gas images of Par-Lup3-4 at 1.3 mm	67
3.3	ALMA CO(2-1) channel emission map of Par-Lup3-4	68
3.4	^{13}CO , CO(2-1) and CO(3-2) spectra	69
3.5	Secondary outflow of Par-Lup3-4	70
3.6	ALMA CO(3-2) channel emission map of Par-Lup3-4	72
3.7	CO ($v=0$ 3-2) flux integrated ALMA map of Par-Lup3-4	73
3.8	ALMA ^{13}CO (3-2) channel emission map of Par-Lup3-4	74

3.9	^{13}CO velocity map	75
3.10	Jet and left bipolar outflow cavity of Par-Lup3-4	76
3.11	Position velocity diagram of the secondary outflow of Par-Lup3-4 using CO(v=0 2-1)	78
3.12	ALMA CO(3-2) velocity and integrated map using uv taper	79
3.13	ALMA ^{13}CO (3-2) channel emission map of the secondary outflow of Par-Lup3-4	80
3.14	SED and modeling results for Par-Lup3-4.	82
3.15	Molecular outflow versus wind mass-loss rate of Par-Lup3-4 and very low-mass sources	85
4.1	Theoretical spectrum fitted to SR 12 C spectrum	93
4.2	Observational template fitted to SR 12 C spectrum	94
4.3	Spectral features in SR 12 C spectrum	96
4.4	H α emission line	97
4.5	Near infrared and optical SR 12 C spectrum	99
4.6	Near ultraviolet SR 12 C spectrum	100
4.7	Comparison of the accretion rate with several indicators	102
4.8	Comparison of age, mass and accretion status of several substellar companions	104
4.9	Mass accretion rates vs stellar mass of stars and substellar companions	105
C.1	AzTEC maps centered at the position of the ALMA detections	123

List of Tables

2.1	Telescopes and filters of the archival data used for the classification of the sample.	24
2.2	Properties of the ALMA continuum detections at 1.3 mm wavelength.	28
2.3	Distances using Gaia Data Release 2	29
2.4	Derived properties from ALMA and AzTEC observations	35
2.5	AzTEC: Densities (critical and observed) and radii (critical and observed) at a temperature of 9 K for the ALMA non-detections	39
2.6	Bolometric temperature and bolometric luminosity of the ALMA sample	40
2.7	ALMA: Densities (critical and observed) and radii (critical and observed) at a temperature of 9 K	49
2.8	ALMA: Densities (critical and observed) and radii (critical and observed) at a temperature of 15 K	49
2.9	AzTEC: Densities (critical and observed) and radii (critical and observed) at a temperature of 9 K	50
2.10	AzTEC: Densities (critical and observed) and radii (critical and observed) at a temperature of 15 K	50
2.11	Estimated masses of the ALMA pre-BD core candidates within an ALMA beam, assuming a r^{-2} density profile from AzTEC	52
2.12	Disk masses of the Class II sources in the Lupus sample	55
3.1	Dust properties of the ALMA detection	64
3.2	Gas properties of the ALMA detection	66
3.3	Outflow geometrical and dynamical properties	76
3.4	Best-fit parameters from SED modeling.	80
4.1	Characteristics of the observed accretion tracers.	98
4.2	Accretion rates measurements	98
4.3	List of wide young substellar companions	101
A.1	List of the ALMA pointings based on the AzTEC detections. The position and the rms are measured in the phase center. We included the previous classification based on the AzTEC detections and the SED from the SOLA catalog. Class II and some Class I/II sources were obtained from the literature	113

List of Abbreviations

ACA	A tacama C ompact A rray
AGN	A ctive G alactic N ucleus
ALMA	A tacama L arge M illimeter A rray
AO	A daptive O ptics
APEX	A tacama P athfinder E Xperiment
ASTE	A tacama S ubmillimeter T elescope E xperiment
ATCA	A ustralia T elescope C ompact A rray
au	a stronomical u nit
BD	B rown D warf
CASA	T he C ommon A stronomy S oftware A pplications
CTIO	C erro T ololo I nter- A merican O bservatory
DENIS	D Eep N ear I nfrared S urvey of the S outhern S ky
DFOSC	T he D anish F aint O bject S pectrograph and C amera
ELT	T he E xtrremely L arge T elescope
ESA	E uropean S pace A gency
ESO	E uropean S outhern O bservatory
FoV	F ield of V iew
IAU	I nternational A stronomical U nion
IRAC	I nfrared A rray C amera
JCMT	J ames C lerk M axwell T elescope
JWST	J ames W ebb S pace T elescope
LABOCA	L arge A pex B olometer C amera
MIPS	M ultiband I maging P hotometer for S IRTF
PACS	P hotodetector A rray C amera and S pectrometer
PdBI	P lateau d e B ure I nterferometer
pwv	p recipitable w ater v apor
QSO	Q uasi- S tellar O bject
SCUBA	S ubmillimetre C ommon- U ser B olometre A rray
SED	S pectral E nergy D istribution
SEST	S wedish- E SO S ubmillimeter T elescope
SFE	S tar F ormation E fficiency
SFR	S tar F ormation R egion
SKA	S quare K ilometre A rray
SMA	t he S ubmillimeter A rray
SOLA	S oul of L upus with A LMA
SPIRE	S pectral and P hotometric I maging R eceiver
SSC	S ub S tellar C ompanion
VeLLO	V ery L ow L uminosity O bject
VLM	V ery L ow M ass

VLT	V ery L arge T elescope
WISE	W ide- F ield I nfrared S urvey E xplorer
WFI	W ide F ield I mager

Dedicado a mis padres

Chapter 1

Introduction

Brown dwarfs (BDs) are substellar objects that fuse deuterium. The masses of BDs ($\leq 0.08 M_{\odot}$) are in the range between low-mass stars and planets. These objects are interesting for various reasons. They represent the low-mass end of the stellar initial mass function and they fill the gap between Jupiter-like planets and stars, sharing common characteristics with both of them. Brown dwarfs have been found as companions to main sequence stars (Oppenheimer et al. 1995) or as single objects (Rebolo et al. 1995), and, more recently the possible formation of rocky planets around BDs (Dressing & Charbonneau 2013) shows that they may also host planetary systems. The atmospheres of BDs show similar features as those of gas giant planets, with the advantage that BDs can be studied in isolation without the presence of a host star.

Identifying the most efficient formation mechanism of BDs is one of the unsolved problems in Astrophysics. In this thesis, we provide observational constraints on the formation theories by presenting a multi-wavelength study that includes a systematic survey, as well as high-angular resolution and high-sensitivity studies of selected substellar objects.

1.1 The discovery of brown dwarfs: theory and observations

Brown dwarfs were predicted for the first time by Kumar (1963) in a theoretical study on the internal structure of very low-mass (VLM) stars (stars with masses between 0.1 to $0.3 M_{\odot}$) (Liebert & Probst 1987) or between 0.1 to $0.2 M_{\odot}$ cf.(Phan-Bao et al. 2014). He first termed them "black dwarf" stars, but the name that later replaced it was "brown dwarf", originally proposed by Jill Tarter in 1975, as part of her PhD thesis (as chronicled by Tarter (2014)). Other names were proposed in the literature, like Infrared Star, Sub-stellar Objects or Extreme Red Dwarf (Tarter 1986, 2014), but today the term "brown dwarf" is the most accepted one by the scientific community. Kumar (1963) proposed that BDs are contracting and have masses below a certain limit so that the temperature and density in the nucleus are too low to ignite hydrogen nuclear reactions and therefore the objects will not reach the stellar main sequence. The BD mass limit was initially predicted to be in the range between $0.07 M_{\odot}$ and $0.09 M_{\odot}$. Below this mass, the objects will contract until reaching a completely quantum mechanically degenerate configuration. Months after the first

study, [Hayashi & Nakano \(1963\)](#) made a more detailed theoretical study on the evolution of the internal structure of low-mass stars, establishing $0.08 M_{\odot}$ as the lower limit for burning hydrogen.

BDs represent the bridge that links planets and stars. On one hand they are able to fuse atomic elements, as stars, for a short period of time between 4 and 50 Myr ([Chabrier et al. 2000](#)). On the other hand the final size of a BD when it finishes the Hayashi contraction¹ is one Jupiter radius, irrespective of its mass. When BDs contract to their final size, they reach their maximum temperature and from that moment on they will slowly cool down. The boundary with planets is established by the deuterium-burning limit that was first set at $0.012 M_{\odot}$ ([Grossman & Graboske 1973](#)). According to the International Astronomical Union (IAU) the current limit separating planets and BDs ([Boss et al. 2007](#)) is at 13 Jupiter masses ($M_{\odot} = 1047 M_J$). So, the realm of BDs stretches between the fusion of deuterium and hydrogen.

Although the lower mass threshold is commonly accepted as the deuterium burning limit, some authors (e.g. [Chabrier et al. \(2005\)](#); [Whitworth \(2018\)](#)) set the limit at the minimum mass for opacity-limited fragmentation in clouds ($\sim 3.14 \pm 1.04 M_{Jup}$), which is the limit where a compact dusty core cannot be divided gravitationally into smaller cores. The fact that even the mass range for BDs is not fully established shows that the field is still in development and that many questions concerning BDs remain currently unanswered.

After more than thirty years of theoretical predictions, three BDs were discovered almost simultaneously by different teams using different methodologies in 1995. Teide 1 ([Rebolo et al. 1995](#)) was the first observationally confirmed BD with a spectral type M9 and a mass of $50 M_{Jup}$. It was classified as a BD from its location in the Hertzsprung Russell diagram. However, the spectral quality was not good enough to measure the lithium content. The presence of lithium ([Rebolo et al. 1992](#)) is used as a test to set the difference between BDs and VLM stars. While BDs are not able to reach the lithium burning temperature², VLM stars reach temperatures high enough to burn it. The lithium test was used to confirm the second BD, PPL 15 ([Basri et al. 1995](#)), with a mass of $0.078 M_{\odot}$ at the boundary between VLM stars and BDs. The third discovered BD was Gliese 229B ([Oppenheimer et al. 1995](#)), with the presence of methane in its atmosphere. It was a companion to a low-mass star with a mass of $0.56 M_{\odot}$.

Since 1995 a countless number of new BDs were discovered and today we know that they are as common as stars. They can be found in clusters, in the field, or as companions to stars. It is clear that BDs of different ages populate the entire Galaxy, but we still do not understand the dominant formation mechanisms. The aim of this thesis is to provide new observational constraints in the formation theories of BDs.

¹The Hayashi contraction is the path followed by a fully convective structure in the Hertzsprung-Russell diagram.

²The lithium burning temperature is 2.5×10^6 K

1.2 Brown dwarf formation theories

Several theories have been proposed to explain the formation of BDs, all of which were developed in the last two decades. These theories make different predictions that can be observationally tested as will be discussed in section 1.3.

Throughout this thesis there will be constant references to the different stages of formation of low-mass stars, whose scheme is shown in Fig.1.1. Low-mass stars are born inside cold molecular clouds that fragment in a hierarchy of clumps due to gravitational instabilities (Shu et al. 1987, and references therein). When the proper conditions of density and temperature are reached, these clumps initiate their gravitational collapse.

First a rotating prestellar core in isothermal contraction is formed (Andre & Montmerle 1994). **Prestellar cores** are cold (bolometric temperature between 10 to 20 K) and visible at (sub)millimetre wavelengths. There is no presence of a central protostar nor infrared emission (Andre et al. 2000, and references therein). The **protostellar** phase comprises the so-called Class 0 and Class I sources. The core is in adiabatic collapse accreting material from the parental envelope. Class 0 protostars are deeply embedded objects that can be detected in the far infrared. Bolometric temperatures are below 70 K (Chen et al. 1995). The massive envelope, observable in the (sub)millimetre regime, is infalling onto the central protostar while part of the gas and dust are expelled from the system through powerful and collimated molecular outflows to compensate for the angular momentum loss. The main accretion occurs in the Class 0 stage. This phase lasts $\sim 10^4$ yr (Andre & Montmerle 1994). In the Class I systems, the outflows are less powerful and have wider opening angles. The central protostar has more mass than the surrounding envelope and it turns out to be visible at near infrared wavelengths. The bolometric temperature spans a range between 70 and 650 K (Chen et al. 1995) and the lifetime of the Class I stage is $\sim 10^5$ yr (Andre & Montmerle 1994). A disk-like flat structure is formed during the protostar phase, due to the conservation of angular momentum. The next phase of evolution is the **Pre-main sequence phase**, which spans the so called Class II and Class III sources. A Class II source is characterized by an excess of emission at infrared wavelengths, which is originated by the dust from the disk surrounding the central protostar. At this stage the envelope has completely disappeared and the contribution of the disk is well visible in the Spectral Energy Distribution (SED). Several accretion indicators are visible at infrared and optical wavelengths. The duration of this phase is $\sim 10^6$ yr (Andre & Montmerle 1994). In Class III sources neither accretion nor outflows are observed, only a debris disk surrounds the central object, containing only small amounts of gas.

In the next subsections we will describe four BDs formation theories: photoevaporation, turbulent fragmentation, dynamical ejection, and disk fragmentation.

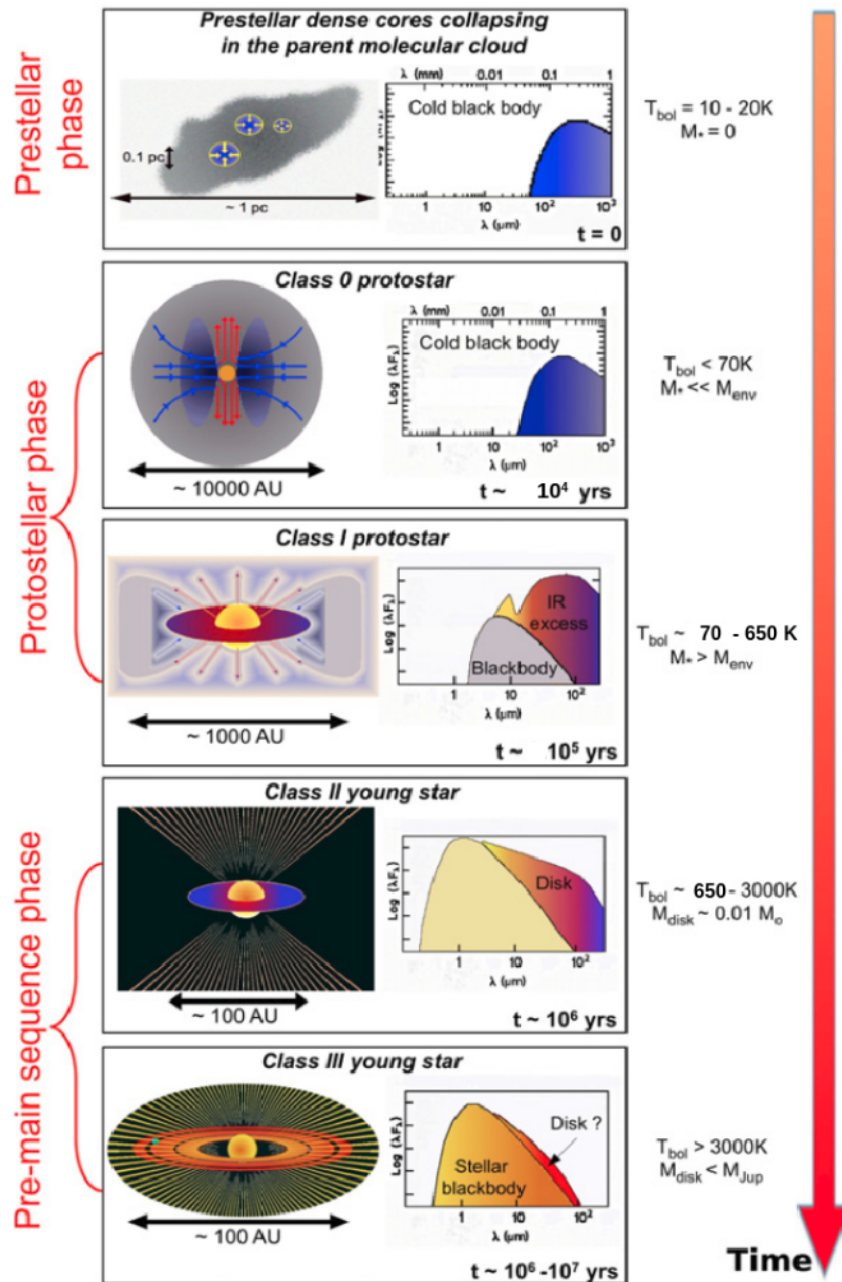


Figure 1.1: Scheme of the formation of a low-mass stars. This plot shows the three main evolutionary phases along with their corresponding SEDs. Adapted from Maury (2011).

1.2.1 Gravoturbulent fragmentation

The theory of turbulent fragmentation (Padoan & Nordlund 2002) was applied to the formation of substellar objects by Padoan & Nordlund (2004) and Hennebelle & Chabrier (2008). In this theory supersonic turbulence is responsible for the formation of dense cores below the Jeans mass, allowing BDs to form in a similar manner as stars are formed (see Fig. 1.1). An external force, e.g. two flows shocking, is needed to form the complex density field. The theory is based on two main hypotheses: the power spectrum of the turbulence can be described as a power law, and the size of the core is escalated to the thickness of the gas layer. In the literature, the formation

of BDs through turbulent fragmentation is also referred to as a scaled down version of star formation (see page 3). In Chapter 2 we use this theory and its formalisms to study a set of presubstellar³ core candidates.

Two open questions are related to the formation of BDs through turbulent fragmentation. Some authors criticize this theory stating dense cores can only be formed if the shocking flows come from all directions with similar velocity, preventing core stability (Lomax et al. 2016). The other caveat is the relation between the observed high number of transient cores versus unstable cores ($\sim 30 : 1$; Whitworth (2018)), which points to a low efficiency of this process to form substellar objects. Additionally, there are observational properties that turbulent fragmentation has not yet explained, such as the observed BD binary statistics.

1.2.2 Photoevaporation (photo-erosion by nearby massive stars)

Photoevaporation or photo-erosion of prestellar cores is a theory divided in three phases that needs two main ingredients: a massive star (OB type) and a prestellar core with enough mass to form an intermediate mass or a low-mass star (see Fig. 1.2). The ionization front from the OB star increases the surrounding temperature by several orders of magnitude, and erodes the outer part of the prestellar core. This is followed by a shock front that triggers the collapse to form a central protostar from the core. The final mass of the central source will be determined by the outcome of the competition between the mass that is accreted from the envelope and the mass that was eroded by the ionization front. The final mass can correspond to a VLM star, a BD, or a planetary mass object. The mathematical formalism of this theory was presented by Whitworth & Zinnecker (2004), but the idea was already proposed by Hester et al. (1996) from observations of the photoevaporation phenomenon in the Elephant Trunk star forming region (SFR).

Photoevaporation has two main caveats. i) It is very efficient at eroding the cores, which means that a large amount of material is not used in the star formation process, therefore it needs massive cores to form BDs. ii) It only works in regions where there are massive stars close to prestellar cores – as in clusters –, but it can not explain the formation of BDs in isolated SFRs without massive stars.

The timescale for this process is fast, and the most straightforward observational signature is the presence of BDs close to massive stars, with signs of wind/outflows in its vicinity.

1.2.3 Dynamical ejection (ejection from multiple systems)

This theory proposes that BDs are formed in multiple systems, as seen in Fig. 1.3. The cloud collapse provokes the embryos to be in competitive accretion (Bonnell et al. 1997). The dynamical interactions between the members of the system produce the ejection of the less massive embryos (Reipurth & Clarke 2001), which will not

³The term presubstellar cores refers to prestellar-like structures in the substellar regime



Figure 1.2: Artistic representation of the photoevaporation of a core. The stellar wind, in the direction bottom right to top left, is originated in a massive star that is not visible in the image. The wind removes most of the material of the prestellar core that is being transformed into a VLM star or a brown dwarf. Courtesy: NASA

have the chance to accrete enough material from the original gas reservoirs where they were born, and they hence become BDs. Therefore, this theory considers BDs as failed stars. Ejections should happen at the earliest (Class 0) stages of their formation, or at ages of $\leq \sim 10^5$ yr, and provoke source velocities of the order of ~ 0.1 km/s. Unfortunately this value is similar to the velocity dispersion found in SFRs, which complicates the use of this parameter as a probe of formation of BDs through this mechanism. The violent ejection may result in a very fast evolution from Class 0 to Class II, in which case Class I sources are not expected in these regions. Other observational predictions of this theory are faster rotations, smaller accretion rates and less infrared excesses due to encounters with other members that truncate the disks.

The dynamical ejection scenario has been supported by simulations (e.g. [Delgado-Donate et al. \(2003, 2004\)](#)), and it explains well the existence of BDs as wide companions of close binary stars. There was some discussion in the literature regarding the theoretical ejection velocity that varies from a few 0.1 km/s ([Reipurth & Clarke 2001](#)) to a few km/s ([Goodwin et al. 2004b,a](#); [Bate et al. 2003](#); [Bate & Bonnell 2005](#)).

One of the main problems that this theory can not explain is the current binary statistics, because it is expected to find a very low number of BD binaries as ejected members of multiple systems ([Goodwin & Kroupa 2005](#); [Hubber & Whitworth 2005](#)).

1.2.4 Disk fragmentation (ejection from fragmented disks)

The disk fragmentation theory ([Fig.1.4](#)) proposes that BDs form inside protoplanetary disks surrounding mainly Sun-like stars ([Stamatellos et al. 2007](#); [Stamatellos & Whitworth 2009](#)). The disk fragments quickly, on the free fall timescale (10^3 to 10^4 yr), and it is predicted that 63% of the BDs should be ejected *from the disk* in the process due to dynamical interactions with the fragmented sources ([Stamatellos & Whitworth 2009](#)). Those ejected BDs should be able to maintain a disk and accrete as well as those that migrate inside the disk remaining bound to the central

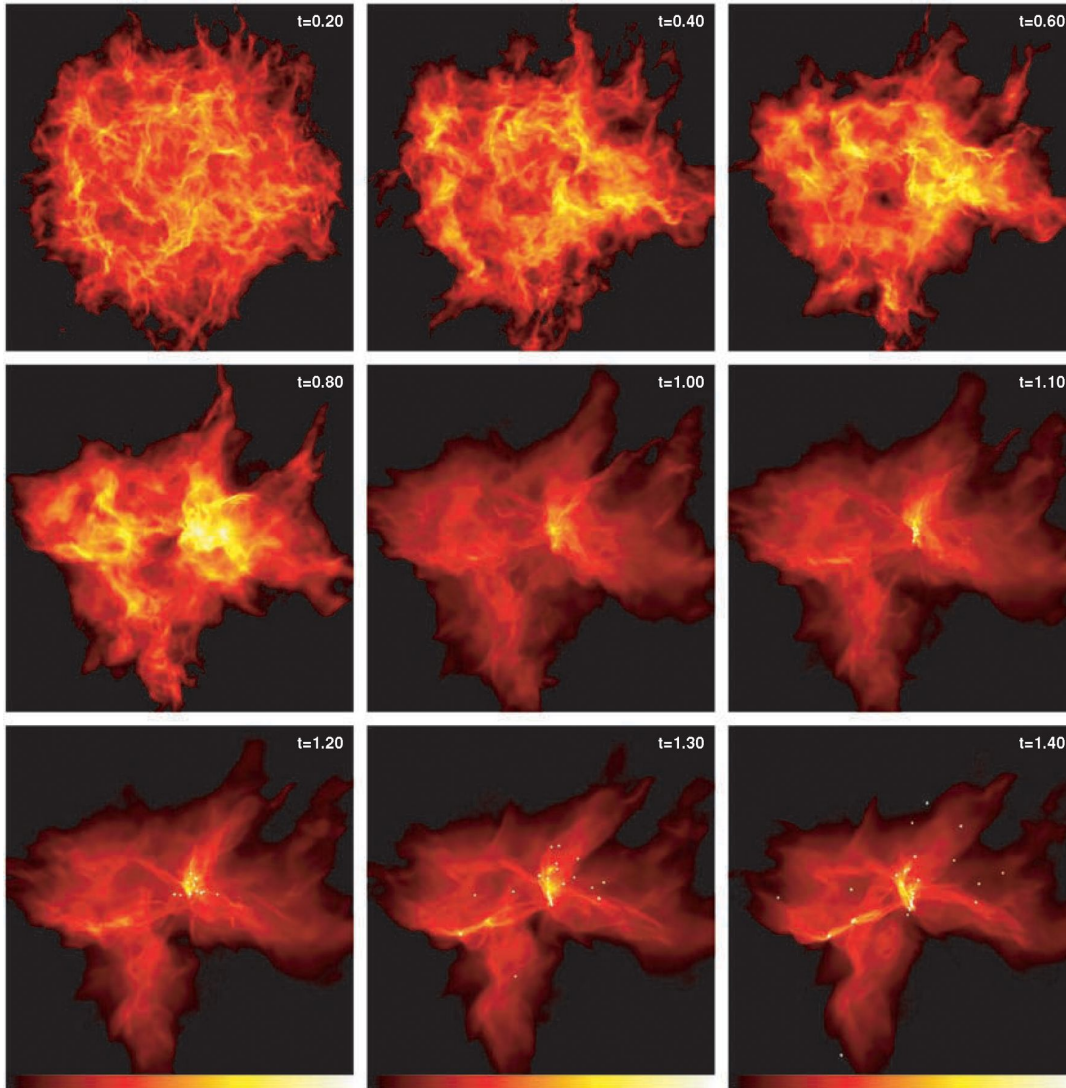


Figure 1.3: Simulation of an interstellar cloud collapse. First stars appear at 1.04 free fall time. At time 1.30 many brown dwarfs and low-mass stars were ejected due to dynamical interactions. Timescale in top right of each panel is in units of free-fall time. Adapted from [Bate et al. \(2003\)](#).

star. Disk fragmentation can also form planetary-mass objects and VLM hydrogen-burning stars.

Disk fragmentation is able to solve two main problems. i) This theory supports the observed statistics of the formation of BD-BD binaries. ii) Disk fragmentation is able to explain the BD desert⁴. The theoretical predictions point out that BDs formed very close to the central protostar, where the gas is still abundant, can accrete gas and transform themselves into VLM stars. Meanwhile BDs that are beyond this limit migrate to larger orbits due to dynamical interactions within the disk. Observations agree with this prediction, not finding close BD companions ($R \leq 5$ au) to Sun-like stars because BDs migrated to a larger orbit, while VLM or low-mass stars are closely bound to their companions.

Simulations from [Basu & Vorobyov \(2012\)](#) probed that clumps, formed via disk fragmentation, instead of Class II or III BDs are ejected from the disk with an ejection velocity of ~ 1 km/s. They also found that: i) some of the disk fragments can suffer from tidal forces that disrupt them during the ejection process, being dissolved and 2) the ejection mechanism is independent of environmental conditions such as temperature or metallicity, but related to properties of the massive disk such as the angular momentum.

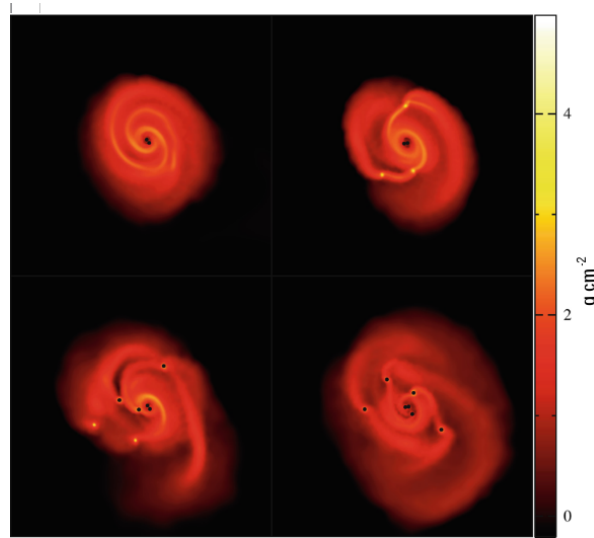


Figure 1.4: A system formed by two close M dwarfs stars. Five brown dwarfs are formed by gravitational disk instabilities. The size of the disk is 300 au and the timescales shown in the are 59, 60, 61 and 62 kyr. Taken from [Whitworth \(2018\)](#)

Disk fragmentation has two main conditions imposed from the gravitational instability theory. The disk needs to be massive enough with a Toomre parameter⁵ less than 1, in other words, the disk needs to be unstable. The second condition is that the proto-fragments need to cool down on the dynamical time-scale, otherwise they would dissolve.

⁴The BD desert is a theoretical range where BDs that may form closer to 5 au from the central protostar fall into that host star. Observations point out that less than 1 % of BDs are orbiting at a distance of 3-5 au to the central stars ([Kraus et al. 2008](#))

⁵Toomre parameter is defined as: $Q = c_s \kappa / \pi G \Sigma$, where c_s is the sound speed, κ is the epicyclic frequency and Σ is surface density.

Figure 1.5 shows precise predictions for objects formed by a) disk instabilities and b) by a collapsing isolated cloud (Stamatellos & Herczeg 2015). The accretion rate or the disk mass in comparison with the mass of the BDs allow to distinguish between the two different formation scenarios. The Stamatellos & Herczeg (2015) simulations show no correlation between the BD mass or the planet mass with the circumstellar disk mass of the host star nor the accretion rate of the host star. Additionally, the protoplanetary disk isolated the embryo BD from the environment, so the BD disk properties will be only related to the protoplanetary disk. It is expected that the accretion rate and the mass of the disk of BDs formed via disk fragmentation, ejected or not, is later than those formed in isolation.

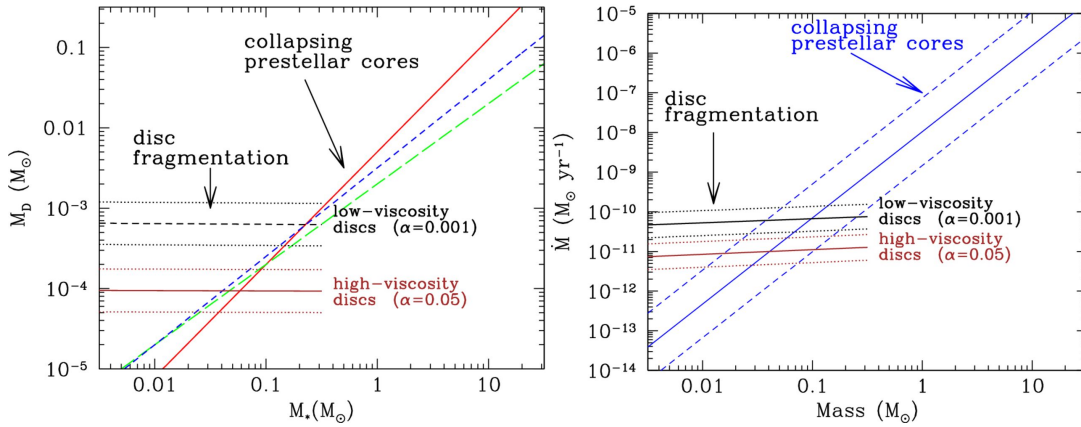


Figure 1.5: Theoretical predictions for BD formation (disk fragmentation or the collapse of prestellar cores). Left panel: Disk masses versus the mass of the host object. Right panel: Accretion rate versus the mass of the host object. In both cases, different disk viscosities were used ($\alpha = 0.01$ or $\alpha = 0.05$), showing $\pm 1\sigma$ uncertainty as dotted lines. Both figures show that if BDs are formed by disk fragmentation they are expected to have more massive disks and higher accretion rate than BDs formed in isolation. Figures obtained from Stamatellos & Herczeg (2015).

More recently, Mercer & Stamatellos (2017) included radiation feedback in the models and found that continuous radiative feedback suppresses the fragmentation and no BDs are formed. Then, BDs should be formed by episodic radiative feedback, although this is less efficient than expected in previous studies (Stamatellos & Herczeg 2015). The episodic accretion of the host star also provokes that planetary mass companions on wide orbits formed through disk instabilities are most likely ejected and are not gravitationally bound to the disk.

The coexistence of the four theories is completely possible, but it is important to discover which of them is the dominant one. There are some theoretical predictions on the percentage of BDs formed by each of these four scenarios. Bate et al. (2002), using hydrodynamical simulations of a molecular cloud, obtained that $\sim 22\%$ of the BDs are ejected from the filaments, and the rest is formed in gravitational unstable circumstellar disks (i.e., through disk fragmentation). BDs in disks are formed mainly by gravitational instability and the high accretion rate of the central star is responsible for the disk fragmentation. The aforementioned paper suggests that large disks around ejected BDs from disk fragmentation are not expected.

1.3 Observational evidence

In the last two decades, a significant observational effort was undertaken to test the main formation theories of brown dwarfs. In this section we put the most important observational studies in context. Since different observational characteristics are expected at the different stages of the evolution of brown dwarfs, we divide this section in two subsections: one related to the early embedded phases, and the second one focused on more evolved Class II sources.

Following the nomenclature provide by [Barrado et al. \(2018\)](#), we will refer to a Pre-BD as a BD in the earliest phase of its formation, i.e. a Pre-BD is a dense core that is not yet in hydrostatic equilibrium. We will call proto-BD a young BD in a evolutionary status analog to a classic Class 0/I low-mass protostar, which contains an embedded hydrostatic core that accretes the material from the surrounding envelope and that usually shows the presence of molecular outflows. We will also refer to VeLLOs (acronym for Very Low Luminosity Objects) ([di Francesco et al. 2007](#)) as sources that have internal luminosities (L_{int}) below $0.1 L_{\odot}$ and that are considered as candidates to proto-BDs or VLM protostars. The relation between BDs and VeLLOs is still a matter of debate.

1.3.1 Earliest stages (Pre- and proto-BDs)

The study of BDs at the earliest stages of their formation is fundamental to understand their origin. Since stars and brown dwarfs evolve very rapidly during the first million years, studies of their properties at early, deeply embedded stages shed light on their formation mechanism(s). Indeed, finding isolated presubstellar cores can be an indication of scaled-down formation of BDs.

The earliest stages must be studied mainly in the (sub)millimetre regime, where pre- and proto-BDs emit the bulk of their energy. The total mass reservoir of the envelope, with a temperature between 8.5 and 10 K ([André et al. 2012](#)), can be obtained through (sub)millimetre observations. The envelope mass should be below $250 M_{\text{Jup}}$ (assuming a Star Forming Efficiency (SFE) of 30 %), therefore a high sensitivity is needed in order to detect these faint objects.

The next stage is the proto-BD phase. This phase is characterized by the presence of a central object of substellar mass, which implies a spectral type higher than M6.5 or a dynamical mass below $75 M_{\text{Jup}}$; a Spectral Energy Distribution (SED) very similar to Class 0/I SEDs in low-mass protostars, emitting mainly from the infrared to the (sub)mm regime, with bolometric temperatures below 70 K for Class 0 objects and below 650 K for Class I, spectral index (α) between 0 and 3 in the range between 2 and 20 μm , and an age below 10^5 yr and 1 Myr for Class 0 and Class I objects, respectively. In addition, it is also expected to see similar phenomena to the ones found in low-mass protostars, like the presence of molecular outflows, envelopes or disk-like flattened structures.

Very few confirmed pre- and proto-BDs are found in the literature. Most BD studies of the last decade searched for BDs with the goal of expanding the census of confirmed sources, and subsequently characterizing them. Two different strategies have been used for this purpose. First, identification of young BD candidates searching in multiwavelength archival survey data (mainly from the infrared to the optical), with the subsequent characterization in the (sub)millimetre regime. The other strategy consists of mapping SFRs using high sensitivity single dish observations in the (sub)millimetre to detect clumps with total masses below $250 M_{\text{Jup}}$, assuming a 30 %SFE. Then, multiwavelength data are used to build the SED and classify the evolutionary stage of these clumps (presubstellar cores, Class 0, Class I or Class II). As a final step interferometric observations are needed to confirm the presence of a central compact core with an envelope and/or a jet and/or a molecular outflow. Interferometric observations with high resolution and sensitivity can rule out the transient nature of presubstellar cores with no optical/infrared counterparts, and also detect the presence of disk-outflow structures in the more evolved proto-BDs. In both cases, the detection of gas emission lines assures the galactic nature of these sources and confirms them as pre- and proto-BD candidates. These two strategies offer different results and are complementary. The searches based on sky surveys are very efficient in finding proto-BDs given that they select more evolved objects emitting in the infrared, but they are not effective in finding very young presubstellar cores without infrared counterparts. On the other hand, mapping star forming clouds in the (sub)mm seems to be a better methodology to find presubstellar cores, as well as proto-BDs, since it does not require infrared counterparts for the candidate selection. In both cases, observations at (sub)millimeter wavelengths are needed to study these sources.

We reiterate, one of the main goals in the field of the formation of substellar objects is to extend the number of confirmed pre- and proto-BDs and characterize them. This is also one of the main goals of this thesis.

Searches based on sky surveys

One of the best examples of systematic searches for young BDs is the one started a decade ago by [Barrado et al. \(2009\)](#). This study focused on the Taurus region. These authors used color-color diagrams (see [Fig.1.6](#)) based on observations with *Spitzer* to obtain a list of young BD candidates. They built SEDs using archival data from the optical to the far infrared and submillimetre (including *Herschel* data). The candidate list was then observed with various submillimetre to centimetre wavelength telescopes including CSO, IRAM-30 and the VLA, to study the presence of emission of cold gas and dust surrounding or/and associated with these candidates. As a result the Class 0/I proto-BD candidate J041757 was identified by [Barrado et al. \(2009\)](#), with an envelope mass between 1 and $10 M_{\text{Jup}}$ and a central core mass between 5 and $30 M_{\text{Jup}}$ that seems to be formed as a scaled down version of low-mass stars. In a follow up work, [Palau et al. \(2012\)](#) reported a second proto-DB candidate in Taurus (J042118) and the preBD candidate J041757-NE, close to J041757, with an envelope mass of $75\text{-}160 M_{\text{Jup}}$ and a gravitational mass of $\sim 140 M_{\text{Jup}}$. High resolution centimeter observations with the JVLA ([Morata et al. 2015](#)) detected thermal

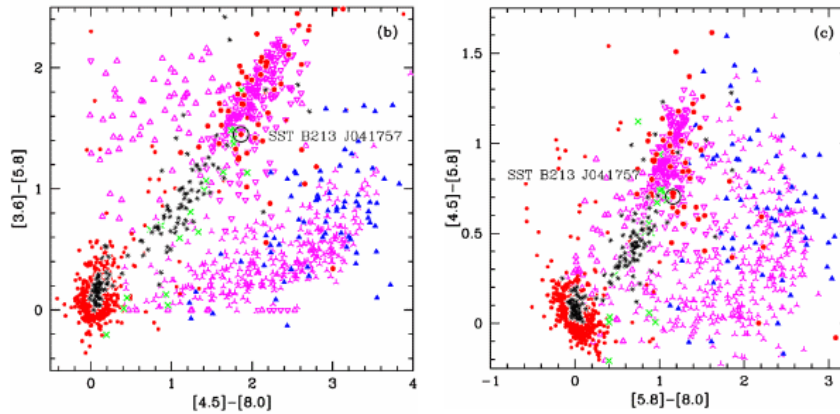


Figure 1.6: Adapted from (Barrado et al. 2009). Color-color diagram of Barnard 213 (Taurus). The Class 0/I and Class I/II are represented as red solid circles and blue solid triangles, respectively.

emission in J041757 coming from a jet along with other three more Class I proto-BD candidates in the same region (J041836, J041847, and J041938). The outflow rate of these four sources seems to be an extension of the properties found in low-mass stars. The outflow rate, the presence of a thermal radio jet and similar Class I characteristics as the ones found in stars point to a very similar formation scenario to low-mass stars. The observational characteristics of these objects can be similar to those of extragalactic sources, resulting in some possibility for mis-classification.

In addition to the previous proto-BD candidates in Taurus, there are several more in other regions but only two bonafide proto-BDs have been confirmed: L328-IRS and ICM348-SSM2; both SEDs are shown in Fig. 1.7. L328-IRS was first detected as a starless core using near infrared spectroscopy (IRAC/MIPS at *Spitzer*) and lately it was classified as a VeLLO (Dunham et al. 2008). The bolometric temperature of 44 K (Lee et al. 2009, 2013) shows that L328-IRS is as Class 0 source. Assuming a SFE of 30% and given the measured envelope mass of $90 M_{\text{Jup}}$, it does not seem possible that the proto-BD is massive enough to become a star. ICM348-SSM2E was first detected in continuum using the *Submillimeter Array* (SMA) (Palau et al. 2014). The envelope mass is less than $\sim 30 M_{\text{Jup}}$, and the mass of the proto-BDs is $46 M_{\text{Jup}}$. ICM348-SSM2E is very close to a star (IC348-SSM2) and it is possible that both objects are part of a common system. However, the authors concluded that also SSM2E seems to be consistent with a scaled down version of star formation.

There are other interesting proto-BD candidates in the literature. Some of the most relevant source names and the reference papers are L1014 (Ward-Thompson et al. 2002; Young et al. 2004; Bourke et al. 2005; Shirley et al. 2007), IRAM 04191 (André et al. 1999; Chen et al. 2012), L673-7 (Dunham et al. 2010), L1148-IRS (Kauffmann et al. 2005, 2008, 2011), and IRAS16253-2429 (Khanzadyan et al. 2004; Dunham et al. 2008; Hsieh et al. 2016; Tobin et al. 2012; Hsieh et al. 2019). The size of the sample of known proto-BDs is too small to infer any statistics and in most of the cases the final confirmation of the substellar nature of the candidates is still missing.

All these sources present common features such as a low bolometric luminosity,

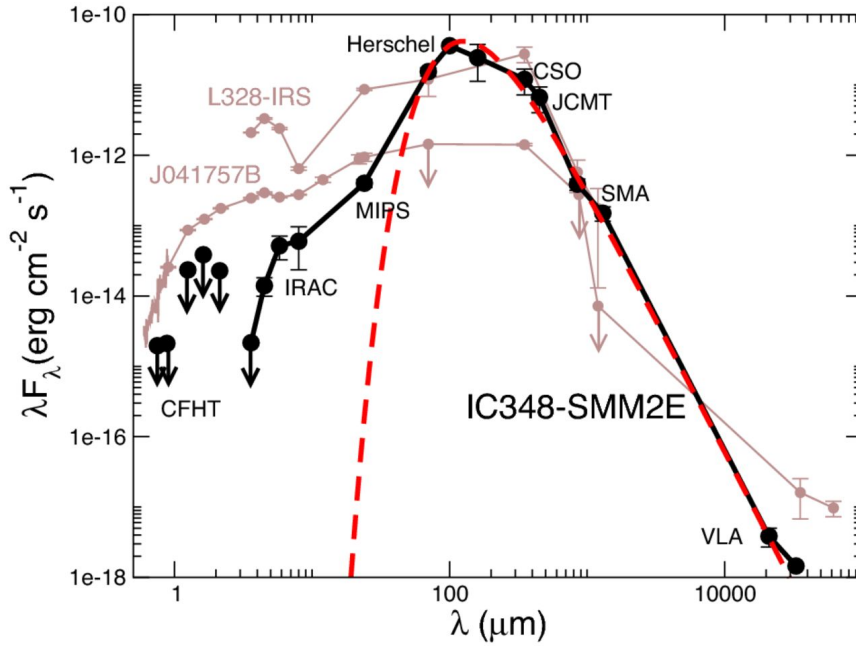


Figure 1.7: Spectral Energy Distribution of IC348-SMM2E (Palau et al. 2014). In brown line other protobrown dwarfs L328-IRS (Lee et al. 2009, 2013) and J041757-B candidate (Barrado et al. 2009)

almost all of them are VeLLOs, and the ones in the proto-BD phase show the presence of bipolar molecular outflows. A cold dust envelope is also present, with a mass exceeding $250 M_{\text{Jup}}$ in some cases.

Submillimetre mapping observations

The strategy based on the mapping of SFRs at large scales, with single dish telescopes, to identify clumps in the substellar regime without optical/infrared counterparts has been used as a method to detect very young substellar candidates. Several pre-BD candidates (less evolved sources) along with proto-BD candidates have been found with this method, although there is only one confirmed pre-BD, Oph B-11 (André et al. 2012). It was first detected as a candidate using continuum maps with the *Submillimetre Common-User Bolometer Array (SCUBA)* camera at *James Clerk Maxwell Telescope (JCMT)* (Pound & Blitz 1995; Greaves et al. 2003). Later observations with the *Plateau de Bure Interferometer (PdBI)* at millimetre wavelengths confirmed the presubstellar nature of the core with a mass of $\sim 0.02\text{-}0.03 M_{\odot}$ inferred from millimetre dust emission. A similar value ($\sim 0.015\text{-}0.02 M_{\odot}$) was obtained from N_2H^+ molecular line emission (André et al. 2012). No infrared counterpart was found; the unambiguous detection of N_2H^+ gas confirmed its galactic nature. Oph B-11 seems to be formed by gravoturbulent fragmentation, as a scaled down version of stars, and not by ejection from a disk (André et al. 2012).

Among the different studies searching for compact emission at the center of substellar clumps, we highlight two works that guided the methodology and line of research followed in Chapter 2. 15 clumps in Chameleon II were detected using *LABOCA*

bolometer ($870 \mu\text{m}$) at the Atacama Pathfinder EXperiment (*APEX*) telescope (see Fig. 1.8) (de Gregorio-Monsalvo et al. 2016). The mass of the clumps, calculated assuming a certain temperature and opacity, provided eleven cores in the substellar regime. Optical to far-infrared archival data were used to classify one of the cores as proto-BD candidate (ChaII-APEX-L), with a point-like source detection at 3.6 and $4.5 \mu\text{m}$. Seven of those clumps were resolved spatially and using the gravoturbulent fragmentation theory only one seems to be unstable, and therefore a good candidate for being a pre-BD (ChaII-APEX-M). A similar study has been performed in Barnard 30, in Orion, (Huélamo et al. 2017; Barrado et al. 2018), where ALMA observations were performed towards the set of clumps observed with *LABOCA/APEX*. Compact continuum emission was detected in five sources out of thirty using ALMA (see Fig. 1.9), two of them are in the Class II and Class I stage and three are starless clumps, which are VeLLOs and seem to be in undergoing gravitational contraction. The aforementioned work needs the detection of gas emission lines to confirm their galactic nature and exclude extragalactic contaminants.

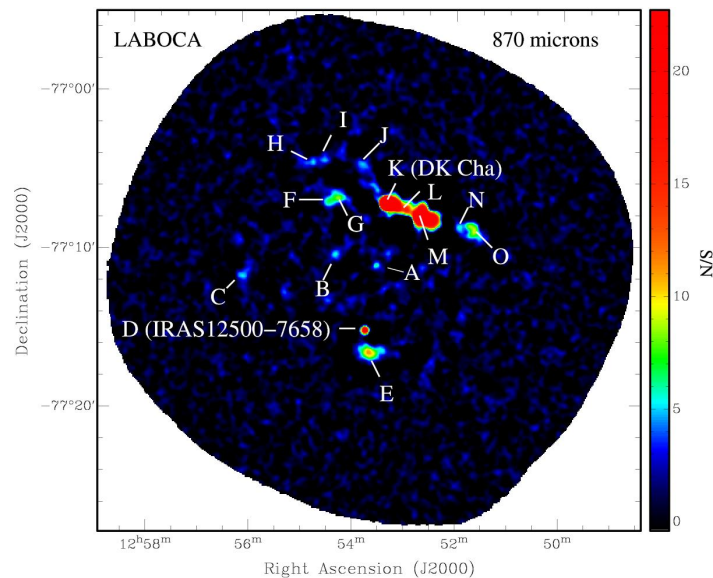


Figure 1.8: LABOCA $870 \mu\text{m}$ emission map of Chameleon II where several clumpy structures as pre- and proto-BD candidates are observable. These candidates have been obtained using the submillimetre mapping observations methodology. Obtained from de Gregorio-Monsalvo et al. (2016).

1.3.2 Brown dwarf disks: accretion and outflows

Class II BDs show some features similar to Class II low-mass stars such as the presence of disks, in which the accretion and mass loss phenomena are supposed to occur. Circumstellar material from gas and dust was first detected around Class II BDs using mid infrared photometry (Comeron et al. 1998). This material, later called "disks" (Natta & Testi 2001; Natta et al. 2002) present an SED in the mid infrared similar to a scaled down version of that observed in low-mass stars.

Other signs of similar evolution to stars have been found such as the presence of large dust grains. The micron size-dust grains, that are found, are bigger than those found

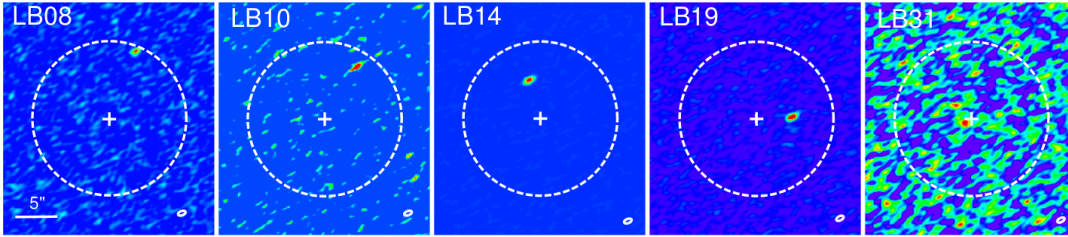


Figure 1.9: This five sources were detected in Barnard 30 with ALMA (Huélamo et al. 2017). The sources have different evolutionary status from pre-BD candidates (3) to Class II (1) candidate, including 1 Class I candidate. This study was first based on single dish observations *LABOCA*.

in the interstellar medium. The presence of these grains, such as olivine, is pointing to dust processing and dust settling in BD disks (Apai et al. 2004).

The first disk mass measurements were in the range between 0.4 to 5.7 M_{Jup} obtained from (sub)millimetre observation (Klein et al. 2003). More BD disks were observed in a study of 20 BD disks in Taurus in the submillimetre regime (Scholz et al. 2006), where no disk truncation was observed contrary to predictions from the ejection from protoplanetary disks scenario. Scholz et al. (2007), studying Upper Scorpius disks, noticed that the disks are flat in terms of flaring suggesting large grains are settled into the disk mid plain.

Interferometric ALMA observations of BD disks have been crucial, not only constraining the parameters such as the dust and gas disk masses or disk radii, but also allowing to obtain more information about the formation mechanisms of these objects. The first ALMA BD disk study (Ricci et al. 2012) presented a resolved gas-rich disk, with the presence of mm-size dust grains. The first resolved BD disk was discovered a year later using CARMA (Ricci et al. 2013). Three additional disks observed in Taurus (Ricci et al. 2014) suggested molecular gaseous disks in rotation, with sizes not compatible with dynamical ejection. They also found mm-size particles implying that grain growth should be common in more evolved BDs which might indicate that future planet formation around BDs is possible. Subsequent studies by Testi et al. (2016a) showed the possible environmental influence on the formation of BDs in Rho Ophiuchus. A similar survey in Upper Scorpius (van der Plas et al. 2016) presented a new relation between the stellar luminosity and the dust disk temperature in the substellar regime. The TBOSS survey with ALMA (Ward-Duong et al. 2018) includes BD disks in Taurus, and the same holds for Ruíz-Rodríguez et al. (2018) in IC 348 and Pascucci et al. (2016) in Chameleon. Very recent results (Rilinger et al. 2019) showed that the disk of two of the most massive BDs have sizes close to 100 au, which supports their formation via turbulent fragmentation instead of disk fragmentation/ejection. Recent results point out that 2M0444 seems to be a pre-transitional disk⁶ (Fig.1.10) based on SED fitting and mid-IR excess emission. Transitional disks have been commonly observed around low-mass stars and can be a key in the future understanding of planet formation around BDs. All these previous

⁶The pre-transitional disk defined as disk with an optically thick inner disk followed by a optically thin disk gap and a optically thick outer disk.

studies improved our understanding of BD disks and the formation mechanism of BDs.

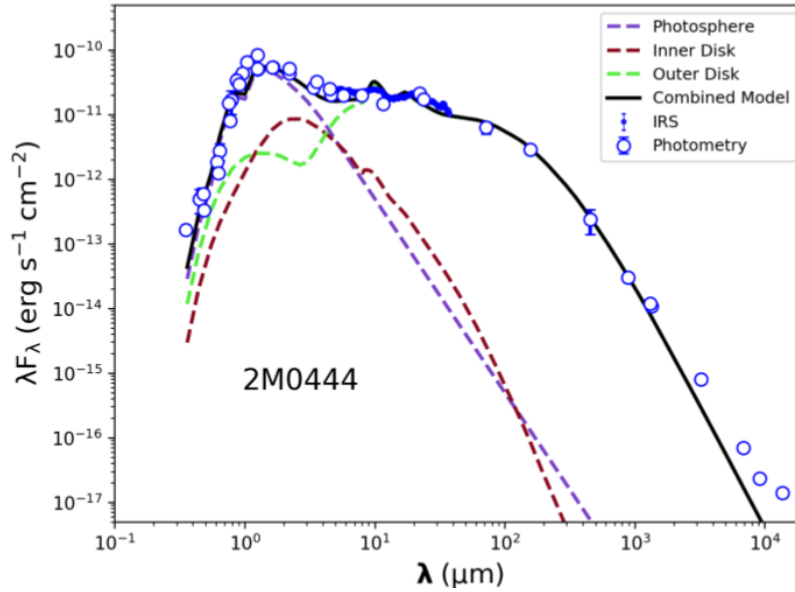


Figure 1.10: Spectral Energy Distribution of 2M0444, the total model is in black while the photosphere is a blue dashed line and disk emission in green. The inner disk is a red dotted line. Fig. 6 right panel from [Rilinger et al. \(2019\)](#)

Magnetospheric accretion

One of the most important characteristics of Class II sources is the magnetospheric accretion. The main accretion phase in low-mass stars occurs during the Class 0 and Class I stages, but envelope material is extinguishing the accretion signatures at optical and near infrared wavelengths. In more evolved sources as Class II sources we can clearly see signs of magnetospheric accretion such as narrow emission lines or ultraviolet continuum excess. In the magnetospheric accretion model (see Fig. 1.11) the material is transferred from the outer disk to the vicinity of the central object, where the disk is truncated due to the stellar magnetosphere, then the material falls into the star/BD along the magnetic field lines. During this process the material is heated up to thousands of K and dust is sublimated. When the gas shocks the stellar photosphere, the temperature rises to 10^4 K producing the emission lines at the ultraviolet/optical and infrared wavelength.

The detection of accretion in BDs began using $H\alpha$ ([Muzerolle et al. 2003, 2005](#)), and later other indicators have been used to study accretion in low-mass stars such as Paschen β , Brackett γ or the Calcium triplet ([Natta et al. 2004; Mohanty et al. 2005](#)).

In general terms the relation between the accretion rate and the central core mass seems to be an extension of the low-mass star regime ([Cahill et al. 2019](#)). The accretion rate in BDs is in the range between 10^{-9} and 10^{-12} M_{\odot}/yr . Measurements of accretion rates are critical to understand the dominant formation mechanism using the predictions of disk fragmentation (see Fig. 1.5). This prediction about the formation mechanism can also extend to BDs as companions of Sun-like stars in wide

orbits, such as FW Tau b, CT Cha b and GSC 06214-00210 B (Bowler et al. 2014, 2011; Wu et al. 2015b). To date the mass uncertainties in the case of wide substellar companions cause difficulties in determining whether they were formed by disk fragmentation or turbulent fragmentation.

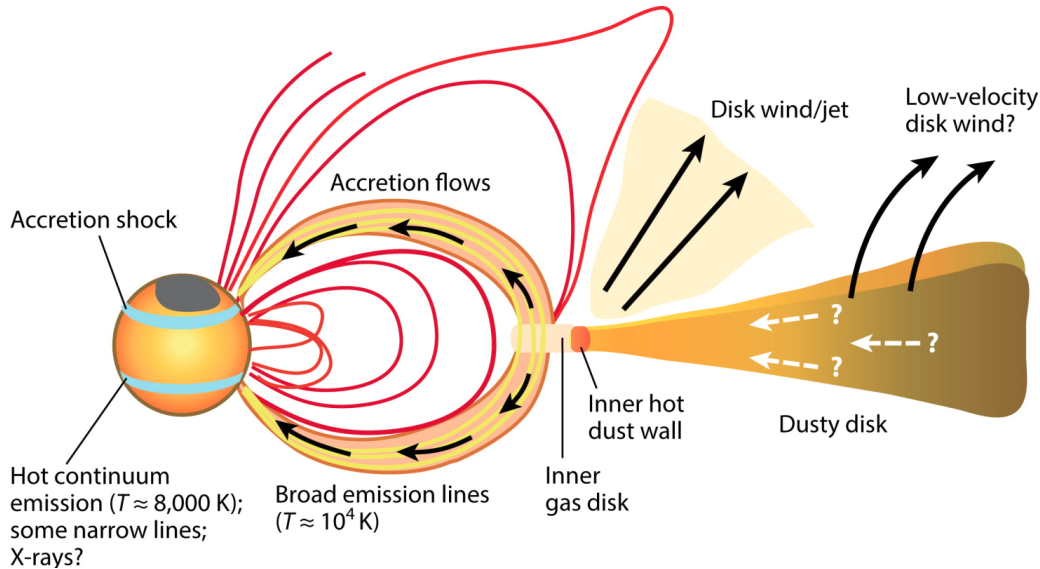


Figure 1.11: Current view of magnetospheric accretion in low-mass stars (Hartmann et al. 2016). Gas and dust moved to the inner disk where the dust is sublimated. Near-IR excess is originated by the dust reirradiation. Gas infall onto the protostar follows the magnetic lines. The gas shock with the photosphere is producing several emission lines and the ultraviolet excess.

Molecular outflows

Another interesting feature is the presence of outflows and jets that are formed due to the conservation of angular momentum as the disk material falls onto the central object.

The phenomenon is mainly characterized by two components: the high velocity component (jet) and the low velocity component (outflow or wind), although there are other components that are shown in Fig. 1.12. The interaction between the envelope and the disk wind creates a cavity (Li & Shu 1996). The cavity wall has the proper conditions to excite molecules that are observable at (sub)millimetre wavelengths. The first detection of jets in BDs and VLM stars occurred at optical wavelength. A supersonic jet was detected using forbidden emission lines in VLM stars (Fernández & Comerón 2001; Looper et al. 2010) and spectroastrometry was used to detect jets in BDs (Whelan et al. 2005b; Joergens et al. 2012b; Whelan et al. 2012) or VLM stars (Bacciotti et al. 2011). The BD and VLM star jets have similar properties to the jets in low-mass stars such as the presence of asymmetries (Joergens et al. 2012a) or bipolarity (Joergens et al. 2012b; Whelan et al. 2012).

The presence of molecular outflows in low-mass stars is very common in Class 0/I sources but less common in Class II systems. The number of molecular outflows

detected in the (sub)mm in BDs/VLM stars is limited to the following systems: L1014 IRS (Bourke et al. 2005), ISO-Oph 102 (Phan-Bao et al. 2008), L1148 IRS (Kauffmann et al. 2011), MHO 5 (Phan-Bao et al. 2011), FU TAU (Monin et al. 2013), IC348-SMM2E (Palau et al. 2014), and GM Tau (Phan-Bao et al. 2014). All of them possess very similar properties: very compact sizes that are between 500 to 1800 au, low velocity outflows between 1 and 4.6 km/s and outflow masses between 10^{-7} and $10^{-10} M_{\odot}$. The outflow velocities of low-mass stars are higher (10-100 km/s) and their outflow sizes are larger (0.01 pc) (Arce et al. 2007a). The measurements for BD/VLM outflows therefore seem to be consistent with young BDs/VLMs being down-scaled versions of forming low-mass stars. However, some of the previous outflow sizes and velocities for BD/VLM stars should vary due to the inclination correction that was not included in some of the studies (e.g. IC 348-SMM2E).

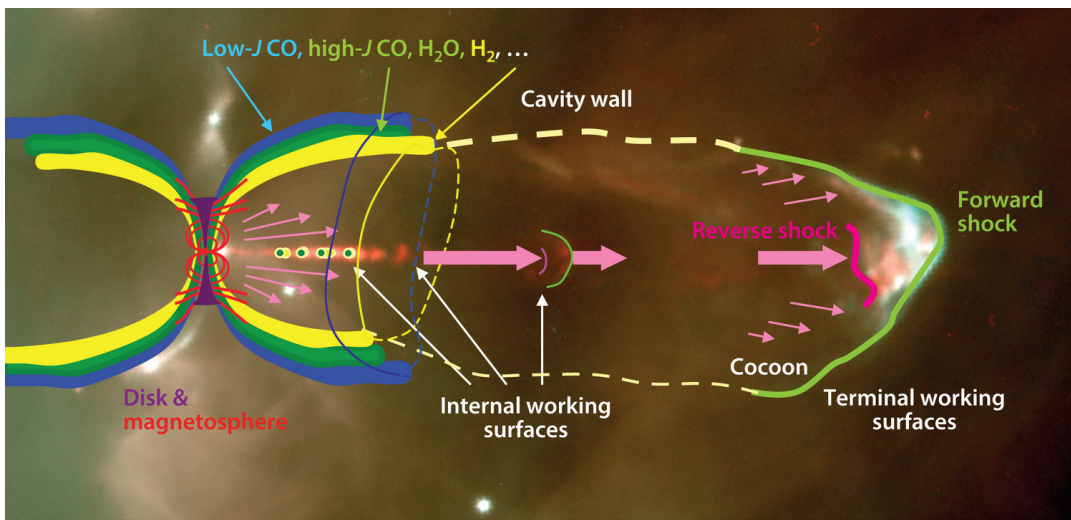


Figure 1.12: Adapted from (Bally 2016). Scheme of the protostellar outflow lobe in low-mass stars. Different structures are appreciable as the disk in purple, the cavity in yellow or the jet in pink. As they get older the opening angle wider and bow structures in the jet direction (Herbig Haro objects) appear. The cavity wall is produced by low velocity shocks that excites CO molecules. The front of the outflow is in green (Forward shock) and is ionizing the interstellar medium.

1.4 Motivation, goal and outline of this thesis

1.4.1 Motivation

In this thesis we aim at studying the formation of BDs through all the different evolutionary stages: from prestellar cores to Class II BDs. To accomplish this objective we combine radio (single-dish and interferometry) with optical observations pushing the current telescopes and instrumentation to the limit of their capabilities. This is required to detect faint objects with the best spatial and spectral resolution. We primarily use data from two telescopes: the Atacama Large Millimeter/Submillimeter

Array (ALMA) and the Very Large Telescope (VLT) with the X-SHOOTER spectrograph. Complementary data from other infrared, optical, and radio telescopes were used to build the SEDs of the sources we studied.

ALMA is an array of 66 high precision antennas that work together as an interferometer at Llano Chajnantor, at an elevation of 5000 m. The atmospheric conditions there, especially in terms of water vapor and phase stability, are excellent to carry out ground-based observations in the submillimetre regime. It is composed of two arrays: the extended 12m array and the Atacama Compact Array (ACA). The ACA is used for recovering large spatial scales, and it is formed by 12 antennas of 7 m that work in interferometric mode plus four antennas of 12 m for single dish studies. The extended 12 m array is formed by 50 antennas and provides high spatial resolution and very good sensitivity resolution. ALMA gives us the possibility for studying the cold universe, from thermal dust emission to molecular line emission.

The VLT telescopes, located in the north of Chile, have a size of 8.2 meters each, being one of the biggest optical telescopes in the world. The extraordinary weather conditions on Cerro Paranal, in terms of humidity and seeing allow for observations of faint substellar companions. A very stable atmosphere is needed to obtain an infrared spectrum for studying accretion with an appropriate signal to noise ratio. Additionally, accretion rates can vary fast so the best strategy is to obtain spectra at different wavelengths at the same time. The only instrument in Paranal that has such characteristics is X-Shooter.

The study presented in this thesis is written before the construction and commissioning of the next generation of telescopes such as The Extremely Large Telescope (ELT), Square Kilometre Array (SKA) or James Web Space Telescope (JWST). These telescopes and interferometers will extend our knowledge about the origin and evolution of brown dwarfs. These new optical/infrared telescopes will allow us to observe faint and low-mass Class 0/I proto brown dwarfs that are currently not detectable. The new radio interferometer (SKA) will provide better resolution and sensitivity to observe synchrotron emission and magnetic fields in BDs. The development of ALMA will be decisive in order to study most of the BD disks that have not yet been detected because of their faintness, as well as resolve them to study their inner structures and map in detail the molecular outflows associated with the earliest phases of BD formation. The original ALMA science drivers have been met with the current capabilities of this observatory, and new science drivers have just been formulated. The ALMA roadmap (Carpenter et al. 2019) has set recently three new science priorities that will motivate the technical upgrade in the next years, two of them very related to the topic of this thesis: detection of the origin of complex organic molecules in regions where stars and planets are formed, and resolving the inner region or protoplanetary disks (~ 1 au). With the new ALMA development plans detailed studies of the structure and properties of dust and gas surrounding young brown dwarfs are expected in the next decades.

1.4.2 Goal

The main questions we tried to address in this work with the performed studies are:

- What is the predominant formation mechanism of BDs?
- Are the wide substellar companions formed from disk fragmentation or from their own presubstellar core?
- Are the outflow properties of BDs and VLMs a downsized version of the ones observed in low-mass stars?
- Are the properties of VLM stars and BDs consistent with a scaled down-version of low-mass star formation?
- Is planet formation possible in BDs?

1.4.3 Outline

In Chapter 2 we present an ALMA survey at 1.3 mm for a set of pre- and proto BD candidates in Lupus 1 and 3. We first used a bolometric map of the dust in these regions (*AzTEC/ASTE*) of Lupus 1 and 3 to identify possible candidates to be observed with ALMA. We complemented the ALMA observations with optical/IR archival data to build the SED and subsequently determined the evolutionary stage of the sources. Several pre-substellar core candidates were identified as well as new proto-BD candidates. We also measured the disk masses of previously known Class II BDs.

In Chapter 3 we present the study of a bipolar molecular outflow in a VLM star called Par-Lup3-4. This source was previously observed in our ALMA survey and we performed follow up ALMA observations with higher resolution and sensitivity at 870 microns to characterize the outflow properties.

In Chapter 4 we present an accretion study of SR 12 C, a wide substellar companion very close to the planetary mass regime. The goal of this study was to trace the accretion of SR 12 C using several accretion indicators in the infrared, optical and near ultraviolet to constrain the origin of the source.

In Chapter 5 we summarize our results and present future lines of research.

Chapter 2

The early stages of substellar formation in Lupus 1 and 3 clouds with ALMA

Abstract

The dominant formation mechanism of brown dwarfs (BDs) is still uncertain and observational samples of pre-substellar cores to Class II objects are needed to test the formation mechanisms. We aim to identify a set of proto- and pre-BDs as well as class II objects with ALMA. Our target sample is formed by a selection of cores from AzTEC/ASTE maps and previously known Class II BDs in the Lupus 1 and 3 molecular clouds. We performed continuum observations with ALMA using Band 6 (1.3 mm). Optical/infrared archival data complement these observations. We detected 19 sources from 15 ALMA fields of views. Considering all pointings in our observing setup, the ALMA detection rate was 23.4 %, and the derived masses were between 0.30 to 124.02 M_{Jup} . We classified these sources according to their Spectral Energy Distribution as six Class II sources, two new Class I/0 candidates and 11 new possible pre brown dwarfs or deeply embedded protostellar candidates. We characterized an excellent candidate for a Class 0 proto-BD source (ALMA J154229.778-334231.86) and measured the dust disk mass of the bona fide Class II BDs. The pre-substellar cores seem to be in contraction, and we might be detecting the hint of a large scale collapse. The Class II BD disks follow the correlation between disk mass and the mass of the central object that is obtained from the low-mass star regime. We conclude that it is highly probable that the sources in the sample are formed as a scaled down version of low mass star formation.

2.1 Introduction

More than two decades have passed since the first BD object was discovered and a large number of BDs have been detected in several star forming regions (SFRs), including Taurus-Auriga (White & Basri 2003), λ Orionis (Barrado y Navascués et al. 2004; Bayo et al. 2011), σ Orionis (Caballero et al. 2007), Upper Scorpius (Bouy et al. 2007), ρ Ophiuchus (Alves de Oliveira et al. 2012), NGC 1333 and IC348 in Perseus (Scholz et al. 2013), and Chameleon I (Mužić et al. 2015). However, their formation mechanism is not fully understood.

Several mechanisms such as ejection, disk fragmentation, photoevaporation and turbulent fragmentation have been proposed to explain the formation of BDs. These mechanisms are properly described in Chapter 1.

One of the main goals in the field of the formation of substellar objects is to increase the number of known pre- and proto-BDs in pursuit of testing the different mechanisms and understanding which of them is the dominant one. The so far only confirmed pre-BD is Oph B-11 (André et al. 2012), and a few promising pre- and proto BD candidates are known such as two proto-BD candidates (J042118 and J041757) and one pre-substellar core candidate in Taurus (Palau et al. 2012). These candidates are embedded in large structures and their properties seem to be consistent with a scaled-down version of low-mass star formation. Finally, the search and study of Very Low Luminosity Objects (VeLLOs) have revealed sources that show proto-BD characteristics (Bourke et al. 2006; Lee et al. 2009; Barrado et al. 2009; Palau et al. 2012, 2014; Morata et al. 2015)

(Sub)millimetre observations are interesting for the study of pre- and proto-BDs because if they are formed as a scaled-down version of low mass stars they should be surrounded by cold envelopes, emitting the bulk of the released energy at these wavelengths. One would also expect to see similar phenomena to the ones that are found in Very Low Mass (VLM) stars, including disks and jets. Indeed circumstellar disks around BDs were identified by Natta & Testi (2001) and Natta et al. (2002) through the study of the BD Spectral Energy Distributions (SED) and the presence of jets, outflows, and accretion has been confirmed (Jayawardhana et al. 2003; Natta et al. 2004; Whelan et al. 2005a; Phan-Bao et al. 2008).

One of the first studies of a sample of 20 BD disks in the (sub)mm regime was presented by Scholz et al. (2006). Following this pioneering work, BD disks were observed using ALMA, not only constraining their system parameters such as the dust and gas disk masses or their radii, but also allowing to obtain more information about the formation of these objects. The first ALMA study of three BD disks was performed in Taurus (Ricci et al. 2014). Subsequent studies (Testi et al. 2016a) showed the possible environmental influence on the formation of BDs in ρ Ophiuchus. A similar survey in Upper Scorpius (van der Plas et al. 2016) discovered a new relation between the stellar luminosity and the temperature in the substellar regime. The TBOSS survey with ALMA (Ward-Duong et al. 2018) included BD disks in Taurus, and IC 348 and Chameleon have been studied by Ruíz-Rodríguez et al. (2018) and Pascucci et al. (2016), respectively. Finally, a similar study to the one that we present here that focuses on pre- and proto-BDs is that of Barnard 30 by Huélamo et al. (2017).

The low declination of the Lupus molecular clouds allows high elevation observations in the southern hemisphere. Night observations are available during August and September avoiding the altiplanic winter, whereas Taurus or Orion are high at night in January and February. Therefore, an international consortium (named SOLA, Soul of Lupus with ALMA) with a high representation at the Joint ALMA Observatory in Chile decided to investigate low-mass star and substellar object formation in Lupus. The consortium has high quality continuum data at 1.1 mm wavelength from Lupus 1

to Lupus 4, taken with AzTEC camera at the Atacama Submillimeter Telescope Experiment (ASTE) telescope located at the Atacama Desert in Northern Chile. These data in combination with Spitzer, Herschel, Akari and other public archival data enables the group to identify low-mass stellar and substellar objects in the early stages of their formation.

The Lupus molecular complex (Barnard 1927) is formed by nine molecular clouds. In this chapter, we focus on region 1 and 3. Despite both clouds belonging to the same complex, they show different properties. The mass of Lupus 1 is an order of magnitude larger compared to Lupus 3. Cambr esy (1999) derived a mass from extinction of $2.6 \times 10^4 M_{\odot}$ for Lupus 1 and $3 \times 10^3 M_{\odot}$ for Lupus 3; a similar result was obtained using ^{13}CO (Tachihara et al. 1996) with masses of $1.3 \times 10^3 M_{\odot}$ and $3.4 \times 10^2 M_{\odot}$ respectively. Lupus 1 is more isolated in the complex compared with Lupus 3 that is surrounded by other Lupus clouds (eg. Lupus 2, 4, 5, 6) (Comer on 2008, and references therein). The stellar populations are also different: Lupus 1 is mainly formed by early M giants (Comer on et al. 2009) and Lupus 3 is one of the regions with more T-Tauri stars (Wichmann et al. 1997). Furthermore, Lupus 3 has the highest star formation rate and column density of all with the other Lupus clouds (Comer on 2008, and references therein). Another remarkable point is the amount of substellar objects detected in Lupus in comparison to Taurus: four times more such objects have been identified in Lupus using similar selection criteria (Comer on 2008; Nakajima et al. 2000; Mer in et al. 2008).

In this chapter we present ALMA Band 6 observations of a sample of pre- and proto-BDs along with previously reported Class II BDs in Lupus. The main objective of this chapter is to shed light on the main formation mechanism of BDs. Due to ALMA's accurate pointing we are able to find optical/infrared counterparts which allows us to study the SED of each object. In section 2.2 we present the ALMA observations performed for the SOLA project. In section 2.3 we present the data analysis that includes ALMA continuum detections, mass estimates, the optical/infrared counterpart association, SEDs, bolometric temperatures and luminosities, and a brief description of each source. In the discussion 2.4 we compare our results with previous AzTEC results and also with the main formation theories; the detection rate and the evolution of the cores; and we compare the disk masses with other SFRs. Finally, conclusions and summary are presented in section 2.5.

2.2 Observations

2.2.1 AzTEC observations

Lupus 1 and 3 clouds were observed with AzTEC (1.1mm) mounted on the Atacama Submillimeter Telescope Experiment(ASTE). A subset of these data were presented by Tsukagoshi et al. (2011) and Tamura et al. (2015) who studied V*1094Sco, that will be discussed in this work, and bright submillimetre galaxies, respectively.

Table 2.1: Telescopes and filters of the archival data used for the classification of the sample.

Telescope/ instrument or survey	Filter ₁ (λ_1)	Filter ₂ (λ_2)	Filter ₃ (λ_3)	Filter ₄ (λ_4)	Pointing Error [arcsec]	Total Pointing Error [arcsec]	Reference
ESO 2.2m/WFI	R _c (657.1 nm)	I _c (826.9 nm)	Z (964.8 nm)		5-10	5.4-10.2	(1), (2)
ESO 1.54m/DFOSC	B _v (548.8 nm)	B _{r,c} (648.9 nm)	G _i (797.8 nm)		10-15	10-15	(3)
ESO 1m/DENIS	I (0.82 μ m)	J (1.25 μ m)	K (2.15 μ m)		\sim 1	2.23	(4)
CTIO/2MASS	J (1.235 μ m)	H (1.662 μ m)	K _s (2.159 μ m)		0.5	2.1	(5)
WISE	W1 (3.4 μ m)	W2 (4.6 μ m)	W3 (12 μ m)	W4 (22 μ m)	\leq 1	\leq 2.2	(6)
Spitzer/IRAC	1 (3.6 μ m)	2 (4.5 μ m)	3 (5.8 μ m)	4 (8.0 μ m)	\sim 1	2.2	(5), (7)
Spitzer/MIPS	1 (23.675 μ m)	2 (71.42 μ m)	3 (155.9 μ m)		\sim 1	2.2	(6)
Akari	f9 (9 μ m)	f18 (18 μ m)			2	2.8	(5)
Herschel/PACS	70 μ m	100 μ m	160 μ m		1	2.2	(8)
Herschel/SPIRE	250 μ m	350 μ m	500 μ m		1	2.2	(8)
APEX/LABOCA	868.9 μ m				3	3.6	(6)
AzTEC/ASTE	1.1 mm				2	2.8	(9)
ALMA	1.3 mm				2	-	

Notes

- (1) <https://www.eso.org/sci/facilities/lasilla/instruments/wfi/doc/2P2-MAN-ESO-90100-0001.pdf>;
- (2) (Astrometry precision based on catalogues, Fernando Comeron private communication);
- (3) <https://www.eso.org/sci/publications/messenger/archive/no.16-mar79/messenger-no16.pdf>;
- (4) [Epchtein et al. \(1994\)](#);
- (5) <https://old.ipac.caltech.edu/2mass/test/about2mass.html>;
- (6) <https://irsa.ipac.caltech.edu/data/SPITZER/docs/irac/iracinstrumenthandbook/30/>;
- (7) [Barrado et al. \(2018\)](#);
- (8) [Sánchez-Portal et al. \(2014\)](#);
- (9) [Umehata et al. \(2014\)](#)

The SOLA group has received these two maps of millimetre continuum observations, and using the entire maps we have revealed hundreds of continuum sources embedded within filamentary structures. The angular resolution obtained in the observation was 28 arcsec with a FoV of $7'.8$. and a noise level of $5.0 \text{ mJy beam}^{-1}$. For more information about these observations we refer to [Tsukagoshi et al. \(2011\)](#) and [Tamura et al. \(2015\)](#).

2.2.2 Ancillary data

The combination of the AzTEC maps and a subsequent search in our own catalog (López et al. in prep) enabled us to obtain a set of highly probable pre and proto substellar objects. In order to classify the detected objects (see Fig. 2.2 to see the position of the detected sources in a Hershel map) we searched in the archives of several telescopes or observatories. Filters used and the respective pointing error for each telescope/instrument are given in Table 2.1.

Optical data were obtained from the Wide Field Imager (*WFI*) at the 2.2-m MPG/ESO ([Baade et al. 1999](#)) and The Danish Faint Object Spectrograph and Camera (*DFOSC*) at the Danish 1.54 m Telescope.

The near Infrared wavelength range was covered by the two surveys: Deep Near Infrared Survey of the Southern Sky (*DENIS*) at the 1-m ESO telescope ([Epchtein et al. 1994](#)) and Cerro Tololo Inter-American Observatory/2MASS telescope (*CTIO/2MASS*) ([Skrutskie et al. 2006](#)).

Medium Infrared wavelength range data were obtained by the Wide-Field Infrared Survey Explorer (*WISE*) (Wright et al. 2010) and Infrared Array Camera (IRAC/SPITZER) (Fadda et al. 2004), both from NASA. This last telescope has another instrument, Multiband Imaging Photometer for SIRTf (*MIPS*), that is used for Far Infrared wavelength coverage. Additionally, two more space telescopes are used in this range: *ASTRO-F* (Murakami et al. 2007) from JAXA and *Herschel* (Pilbratt et al. 2010) from the European Space Agency (ESA). From *Herschel* we obtained data of two instruments: the Photodetector Array Camera and Spectrometer (*PACS*) (Poglitsch et al. 2010) and the Spectral and Photometric Imaging Receiver (*SPIRE*) (Griffin et al. 2010).

Millimetre and submillimetre radio wavelengths are also covered by the Large Apex BOlometer CAmera (LABOCA) (Siringo et al. 2009) at APEX observatory for Lupus 3.

Finally, other telescopes including the Australia Telescope Compact Array (*ATCA*), the Swedish-ESO Submillimetre Telescope (*SEST*) and the Submillimetre Array (*SMA*) were used, but no detections were obtained from any of these telescopes for Lupus 1 and 3, therefore we do not include them in the table above.

2.2.3 The sample

The AzTEC maps at 1.1 mm (see Fig. 2.1) of the Lupus 1 and 3 clouds that have revealed hundreds of continuum sources embedded within filamentary structures. The preliminary analysis for the ALMA proposal showed that many of these sources were VLM stars or substellar cold compact structures with a mass below $0.075 M_{\odot}$, assuming a temperature of 10 K and an emissivity index of $\beta = 2$. We searched counterparts at optical and near-Infrared wavelengths using the center of the AzTEC beam. Then we identified a set of pre- and proto-stellar candidates with masses potentially in the substellar regime. We complemented this sample with previously known substellar objects in Lupus 1 and 3 from Merín et al. (2008); Comerón et al. (2009); Mužić et al. (2014). We classified the initial sample as 33 pre-substellar objects, 6 Class 0 and I objects, 3 Class I/II and 22 Class II objects. Initial classification, phase center coordinates and rms are given in Appendix A.

2.2.4 ALMA observations

The observations were performed between the 31st of March and the 1st of April 2016, as part of the ALMA Cycle 3 program 2015.1.00512.S¹. We observed all 64 targets in our sample using single field interferometry in band 6, with a field of view (FoV) of 23 arcsec. A total of six individual data sets were obtained. The number of antennas for each data set ranged between 42 to 44. The total allocated time for this

¹This work makes use of the following ALMA data: ADS/JAO.ALMA#2015.1.00512.S. ALMA is a partnership of ESO (representing its member states), NSF (USA) and NINS (Japan), together with NRC (Canada), MOST and ASIAA (Taiwan), and KASI (Republic of Korea), in cooperation with the Republic of Chile. The Joint ALMA Observatory is operated by ESO, AUI/NRAO and NAOJ.

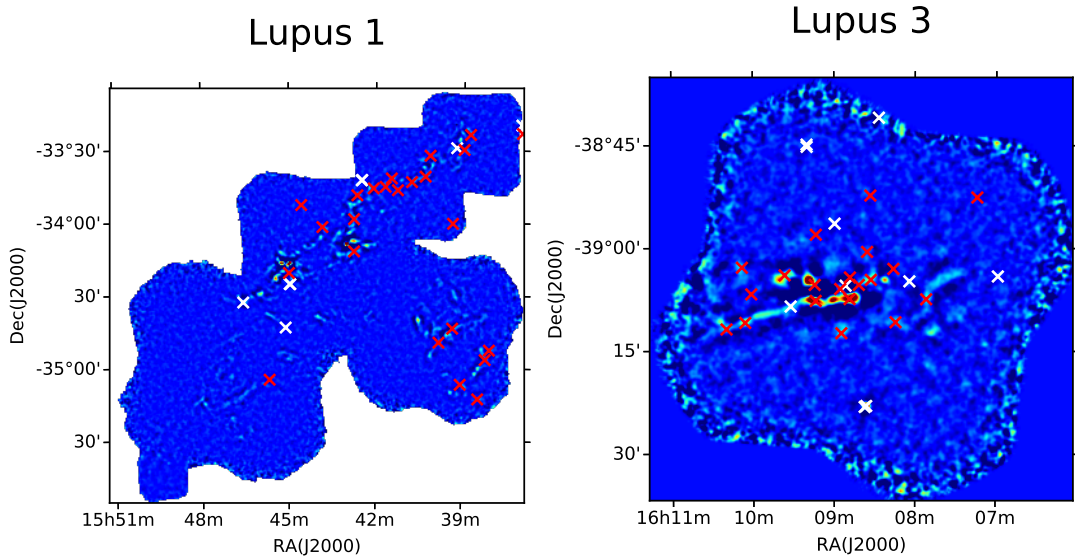


Figure 2.1: AzTEC maps of Lupus 1 molecular cloud (left panel) and Lupus 3 molecular cloud (right panel) overlaid with the ALMA pointings. White crosses represent detections and red ones non-detections.

program was 6.7 hours including overheads, with an average time on each science source of 4.7 minutes. Data were taken under good and stable weather conditions (precipitable water vapor (pwv) ranged from 1.1 to 1.7 mm).

The correlator was set up to observe five different spectral windows in dual polarization mode with the aim of detecting continuum emission. One of the basebands was configured to observe two spectral windows of 0.469 GHz bandwidth and 0.488 GHz channel width (~ 0.3 km/s velocity resolution) each, one of them centered at 230.538 GHz, the rest frequency of CO(2–1). The other three basebands were configured to observe three different spectral windows of 1.875 GHz each, and at a spectral resolution of 1.938 MHz (~ 2.5 km/s velocity resolution) centered strategically at 233.5 GHz, 217.0 GHz and 219.25 GHz to get serendipitous detections of

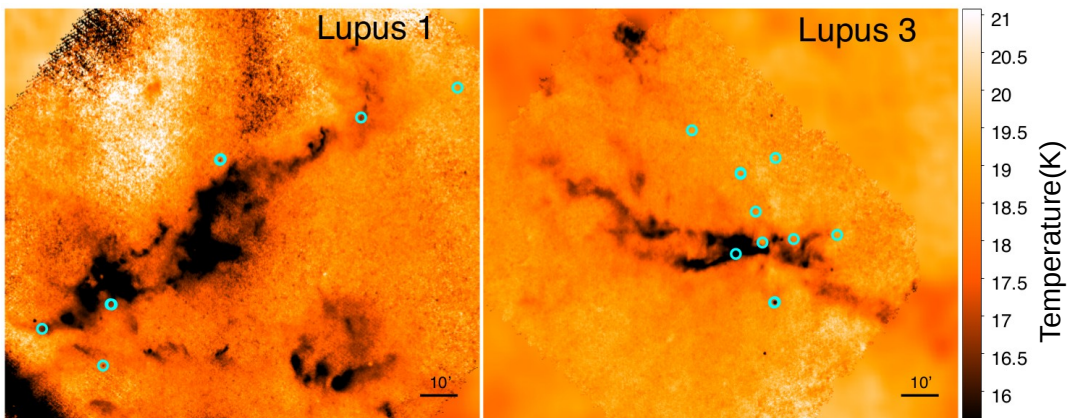


Figure 2.2: Herschel temperature maps for Lupus 1 and 3 clouds (Teixeira et al., in prep.). North is up and East to the left. The ALMA detections are displayed as cyan circles.

C¹⁸O(3-2), SiO(5-4), and DCN(3-2) and to have the best atmospheric transmission.

QSO J1517-2422 was used as bandpass calibrator for the whole sample. This QSO was used as a flux calibrator for one of the datasets while Titan was used for the remaining execution blocks. Two distinct phase calibrators were used. For the three datasets of Lupus 1, QSO J1610-3958 was used, and the QSO J1534-3526 was selected for the observations towards Lupus 3.

The Common Astronomy Software Applications package (CASA) was used for processing the data. Most of the dataset used the pipeline version 4.5.3 for calibration and image processing and only one of the executions was reduced manually using CASA version 4.6. The task CLEAN was used to produce continuum and spectral line images. We selected a Briggs weighting with Robust parameter value of 2 for producing all the images. Primary beam correction was applied before inferring physical parameters from the images. The achieved rms at the phase center was on average $\sim 70\mu\text{Jy}/\text{beam}$ for the continuum and $\sim 6\text{ mJy}/\text{beam}$ in a 0.3 km/s channel width for the spectral line data. The angular resolution of the images was $\sim 0.9''$. The absolute positional accuracy (using 2σ) of the ALMA images in our sample spans between 4 to 270 marcsec with an average value of 148 marcsec. Detailed values for each source are given in Tab. 2.2.

2.2.5 Distances

Our first approach was to adopt the distances that appear in Rygl et al. (2013) of 150 pc for Lupus 1 and 200 pc for Lupus 3. But with the new parallaxes obtained from the Gaia Data Release 2 (Gaia Collaboration et al. 2018) we were able to calculate distances more accurately. We measured the distances in two different ways: with and without a Bayesian approach.

For the measurement of Lupus 1 and 3 clouds we used a sample of spectroscopically confirmed members (Comerón et al. 2009) and we applied the python code kalkayotl from Javier Olivares that uses a Bayesian approach to obtain a precise distance as it is recommended in Bailer-Jones (2015). We also used this methodology to obtain the distance for single sources in both Lupus 1 and 3 as long as their parallaxes were available. Otherwise we assumed the mean distance for each cloud that we obtained as 153.35 ± 4.64 and 154.75 ± 9.59 pc for Lupus 1 and 3 respectively.

In this work, we compare disk masses with similar sources in the literature (section 2.4.6), and therefore we performed consistent distance estimates for other regions. As a first approximation we obtained the distance to sources in Chameleon, Taurus, Upper Scorpius and ρ Ophiuchus as $d = 1/\text{parallax}$ without using the mentioned Bayesian code. The distances for each source that is mentioned in this chapter are listed in Table 2.3.

Finally, there are five Class II BDs (153701.1-332, 160545.8-385, 160714.0-385, 160848.2-39 and 161210.6-390) in our survey whose distances from the literature are not the expected ones for Lupus 1 and 3. Therefore, these sources are not part of the complex. This is in the same line as a recent result using Gaia DR2 from Manara et al. (2018) where only 5 sources from 83 candidates in Lupus 5 and 6 are at a distance compatible with the other Lupus clouds.

Table 2.2: Properties of the ALMA continuum detections at 1.3 mm wavelength.

Name	RA(J2000) ¹	Dec(J2000) ¹	Astrometric accuracy	Separation from phase center	rms	Flux ²	Peak ³	Integrated ⁴	Image component size ⁴			Peak flux ⁴	Beam Size ⁴		
	[h m s]	[° ' "]				[mJy]	[mJy /beam]		deconvolved from beam				[mJy/beam]	Major	Minor
			[marcsec]	[arcsec]	[Jy/beam] ×10 ⁻⁴	[mJy]	[mJy /beam]	[mJy]	Major axis	Minor axis	Position angle		[arcsec]	[arcsec]	[deg]
									[marcsec]	[marcsec]	[deg]				
<i>ALMA</i> J153702.653 – 331924.92	15 : 37 : 02.653	–33 : 19 : 24.92	251	4.82	0.96	0.45	0.45	0.43 ± 0.09	–	–	–	0.48 ± 0.06	0.94	0.93	31.64
<i>ALMA</i> J153914.996 – 332907.62	15 : 39 : 14.996	–33 : 29 : 07.62	151	9.62	0.94	0.73	0.73	0.82 ± 0.08	–	–	–	0.74 ± 0.04	0.91	0.83	–83.66
<i>ALMA</i> J154228.675 – 334230.18	15 : 42 : 28.675	–33 : 42 : 30.18	75	9.71	1.44	2.84	2.25	3.33 ± 0.16	–	–	–	2.23 ± 0.07	0.94	0.93	9.38
<i>ALMA</i> J154229.778 – 334231.86	15 : 42 : 29.778	–33 : 42 : 41.86	44	10.12	1.06	4.06	2.81	4.50 ± 0.12	771 ± 38	641 ± 38	57 ± 13	2.85 ± 0.05	0.94	0.93	9.38
<i>ALMA</i> J154456.522 – 342532.99	15 : 44 : 56.522	–34 : 25 : 32.99	42	6.24	0.68	2.50	1.92	2.79 ± 0.11	838 ± 55	284 ± 77	79.2 ± 3.9	1.94 ± 0.05	0.91	0.83	–83.37
<i>ALMA</i> J154458.061 – 342528.51	15 : 44 : 58.061	–34 : 25 : 28.51	80	13.36	0.97	1.42	1.42	1.49 ± 0.06	–	–	–	1.44 ± 0.03	0.91	0.83	–83.37
<i>ALMA</i> J154506.515 – 344326.15	15 : 45 : 06.515	–34 : 43 : 26.15	180	11.97	0.89	0.26	0.58	0.49 ± 0.02	–	–	–	0.59 ± 0.01	0.95	0.82	–81.47
<i>ALMA</i> J154634.169 – 343301.90	15 : 46 : 34.169	–34 : 33 : 01.90	130	14.77	0.83	0.75	0.75	0.83 ± 0.02	–	–	–	0.76 ± 0.01	0.96	0.82	–81.93
160658.7 – 390405	16 : 06 : 58.604	–39 : 04 : 07.88	152	7.60	0.62	0.48	0.48	0.66 ± 0.04	–	–	–	0.49 ± 0.02	0.93	0.85	86.69
<i>ALMA</i> J160804.168 – 390452.84	16 : 08 : 04.168	–39 : 04 : 52.84	126	4.31	0.93	0.87	0.87	1.01 ± 0.05	–	–	–	0.87 ± 0.03	0.93	0.85	86.11
160826.8 – 384101	16 : 08 : 26.773	–38 : 41 : 01.48	44	9.06	0.59	1.57	1.57	1.58 ± 0.05	–	–	–	1.63 ± 0.03	0.93	0.85	86.80
<i>V * V1094Sco</i>	16 : 08 : 36.157	–39 : 23 : 02.74	4	15.82	2.28	244.05	73.64	218.2 ± 6.1	1756 ± 55	1089 ± 39	108.2 ± 2.7	61.8 ± 1.4	0.92	0.84	83.83
<i>Lup706</i>	16 : 08 : 37.316	–39 : 23 : 11.38	226	0.50	0.90	0.22	0.47	0.53 ± 0.04	–	–	–	0.46 ± 0.02	0.93	0.85	84.77
<i>Par – Lup3 – 4</i>	16 : 08 : 51.426	–39 : 05 : 30.82	196	0.36	0.51	0.31	0.31	0.41 ± 0.07	–	–	–	0.28 ± 0.04	0.93	0.84	84.26
<i>SONYC – Lup3 – 7</i>	16 : 08 : 59.530	–38 : 56 : 27.96	270	6.26	0.55	0.32	0.24	0.45 ± 0.04	–	–	–	0.32 ± 0.02	0.93	0.84	82.57
<i>ALMA</i> J160920.089 – 384515.92	16 : 09 : 20.089	–38 : 45 : 15.92	113	6.01	0.78	0.90	0.81	1.18 ± 0.11	–	–	–	0.82 ± 0.05	0.93	0.85	85.96
<i>ALMA</i> J160920.171 – 384456.40	16 : 09 : 20.171	–38 : 44 : 56.40	226	13.75	1.75	0.91	0.91	1.17 ± 0.22	–	–	–	0.90 ± 0.10	0.93	0.85	85.96
<i>ALMA</i> J160932.167 – 390832.27	16 : 09 : 32.167	–39 : 08 : 32.27	145	11.89	1.28	0.62	0.62	0.47 ± 0.04	–	–	–	0.65 ± 0.03	1.12	0.82	85.61
<i>ALMA</i> J161030.273 – 383154.52	16 : 10 : 30.273	–38 : 31 : 54.52	108	4.76	0.64	0.70	0.70	0.72 ± 0.03	–	–	–	0.71 ± 0.02	0.93	0.85	86.24

¹ J2000.0 Positions of the peak intensity in right ascension and declination.

² Flux density measured inside the contour at 3 σ level

³ Peak intensity

⁴ Integrated flux, deconvolved size, peak flux and beam size obtained from a Gaussian fitting using the CASA task imfit

Table 2.3: Distances using Gaia Data Release 2

Name	Distance [pc]
Lupus detection	
160658.0-390405	156.96 ± 3.37
160826.8-384101	165.27 ± 3.54
V*1094 Sco	153.71 ± 1.09
Lup706	191.13 ± 29.13
Par-Lup3-4	155.22 ± 14.45
SONYC-Lup3-7	151.12 ± 6.38
Lupus no detection	
153701.1-332	93.56 ± 3.49
153709.9-330	175.34 ± 6.50
153921.8-340	152.29 ± 8.64
154140.8-334	151.03 ± 8.02
160545.8-385	44.37 ± 0.20
160714.0-385	124.48 ± 4.20
160816.0-39	164.41 ± 5.25
160833.1-385	158.32 ± 3.50
160848.2-39	183.76 ± 4.90
161144.9-383	169.00 ± 4.65
161225.6-381	159.10 ± 3.20
161210.6-390	232.93 ± 30.27
ρ Oph	
SONYC-RhoOph-8	–
ISO-Oph023	–
ISO-Oph030	136.6 ± 3.6
ISO-Oph032	151.3 ± 4.7
ISO-Oph033	–
ISO-Oph035	–
CRBR 2322.3-1143	–
ISO-Oph042	165.9 ± 14.8
GY92-202	–
ISO-Oph102	142.12 ± 2.7
ISO-Oph138	–
GY92-264	–
ISO-Oph160	142.7 ± 18.4
ISO-Oph164	142.7 ± 10.2
GY92-320	138.9 ± 13.6
ISO-Oph176	151.7 ± 13.22
ISO-Oph193	140.0 ± 13.63
Upper Scorpius	
2MASS J16060391-2056443	137.1 ± 5.07
2MASS J16193976-2145349	–
2MASS J16100541-1919362	149.7 ± 7.0
2MASS J15591135-2338002	139.9 ± 7.0
2MASS J15560104-2338081	139.8 ± 5.4

2MASS J15555600-2045187	145.6 ± 4.5
Taurus	
2M0444	141.0 ± 2.7
CIDA1	135.7 ± 1.6
CFHT Tau4	147.1 ± 5.1
2MASS J04141188+2811535	131.1 ± 2.8
2MASS J04400067+2358211	120.5 ± 2.3
2MASS J04262939+2624137	155.9 ± 5.5
IRAS F04262+2654	–
2MASS J04230607+2801194	133.9 ± 2.4
2MASS J04414825+2534304	136.2 ± 3.7
2MASS J04390396+2544264	144.0 ± 4.4
V* GM Tau	138.3 ± 2.8
2MASS J04381486+2611399	145.4 ± 14.7
Chameleon	
J10561638-7630530	196.48 ± 4.07
J11062942-7724586	–
J11063276-7625210	187.13 ± 7.12
J11074656-7615174	194.22 ± 7.46
J11081850-7730408	179.32 ± 4.25
J11082570-7716396	185.65 ± 7.39
J11083952-7734166	–
J11095215-7639128	240.14 ± 12.70
J11105597-7645325	140.23 ± 14.33

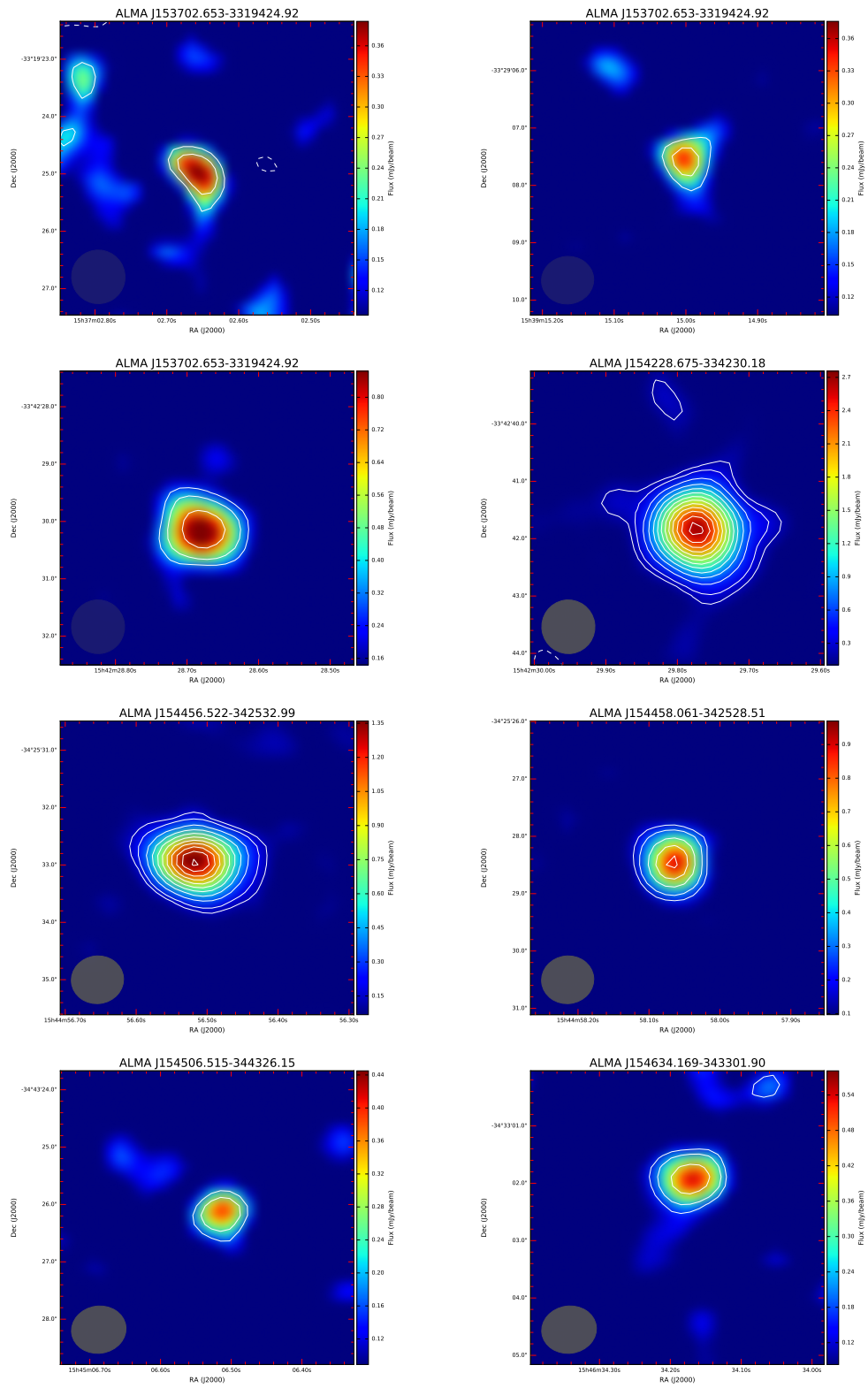
2.3 Results

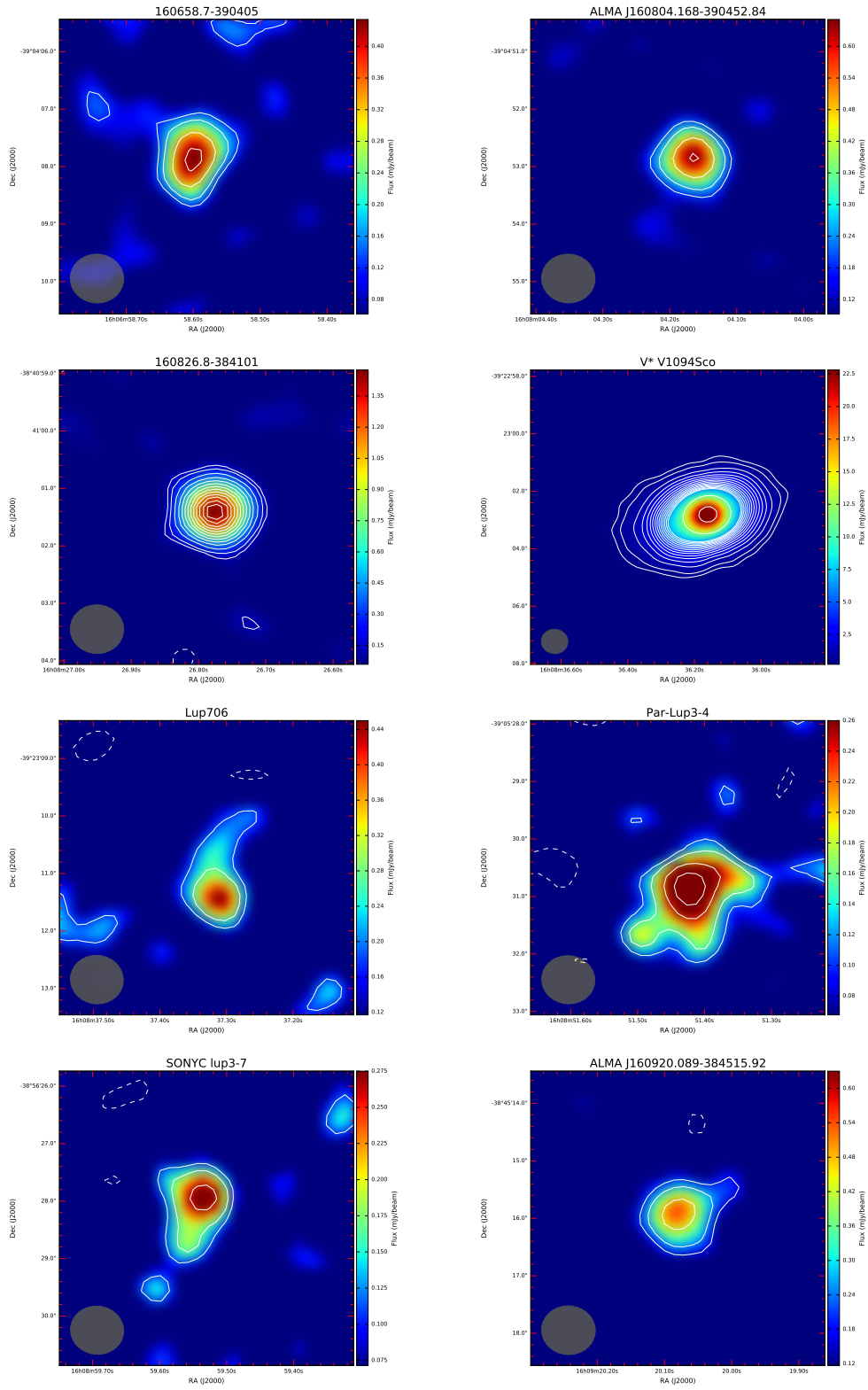
2.3.1 ALMA continuum detections

ALMA continuum images for each detection are shown in Figure 2.5. In total, 19 sources were detected in continuum emission, inside of 15 pointings among the 64 observed candidates. The flux density ranged between 0.22 and 244.05 mJy (see Tab. 2.2).

We adopt the naming convention recommended by ALMA for new discovered sources, but in the discussion we call each source as J#####, for example ALMA J154228.675-334230.18 is named as J154228, except for ALMA J160920.089-384515.92 that is J1609200 and ALMA J160920.171-384456.40 named as J1609201.

There are four ALMA pointings where we detect two sources inside the primary beam (J154228 and J154229, J154456 and J154458, J1609200 and J160920171, Lup706 and V*V1094 Sco) as can be seen in Fig. 2.6. Additionally, the number of spatially unresolved objects is 16.





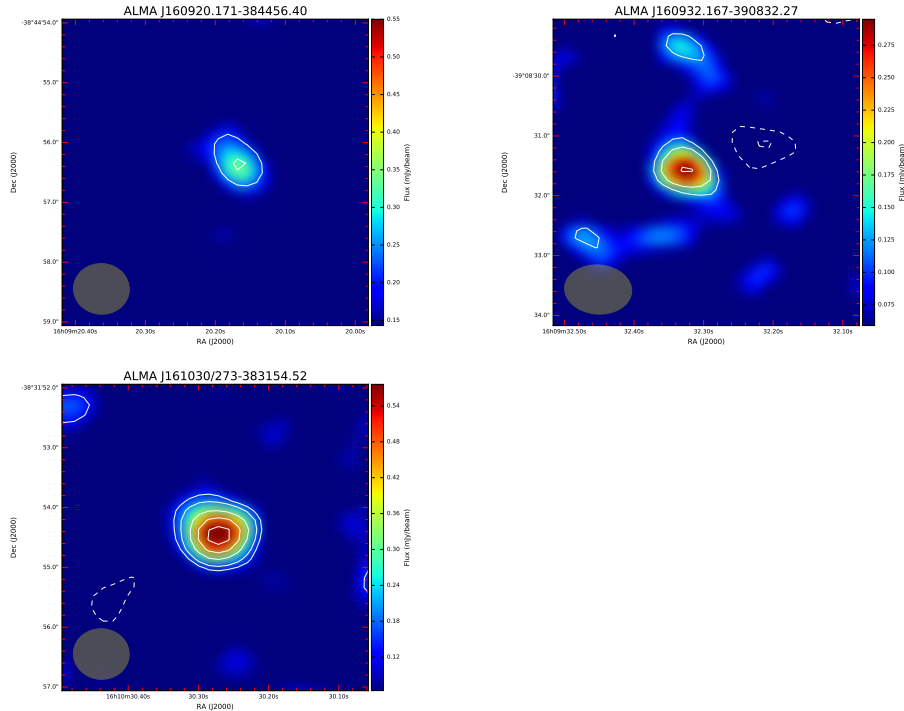


Figure 2.5: 1.3 mm ALMA continuum images of the 19 detected sources. White contours represent 2,3,5,7,...,29,50,100 σ . σ is the rms noise level of each respective map, given in Table 2.2. Dashed contours represent negative emission at -3 and -2σ . Beam size is represented by the grey ellipse in the bottom left corner. Primary beam correction is not applied.

The properties of the sources detected in continuum with ALMA are described in detail in Table 2.2 with additional information including the position, the separation from the phase center, the rms, the flux density and the peak intensity. Other values such as the integrated flux, the size, peak flux and beam size are also included in the table. These last values were obtained from a Gaussian fitting using the task IMFIT from CASA.

2.3.2 ALMA: Gas emission detections

Although the main goal of the observations, and therefore for this chapter, was obtaining continuum emission images, the CO(2-1) gas emission line was also included in the spectral setup. We only have a clear gas detection of the source Par-Lup3-4, a more complete description of the detection can be found in Chapter 3.

2.3.3 ALMA: Mass estimates

The total mass of the cores (see Tab. 2.4) is calculated assuming that the observed emission is optically thin and a mass ratio between gas and dust of 100. Given these

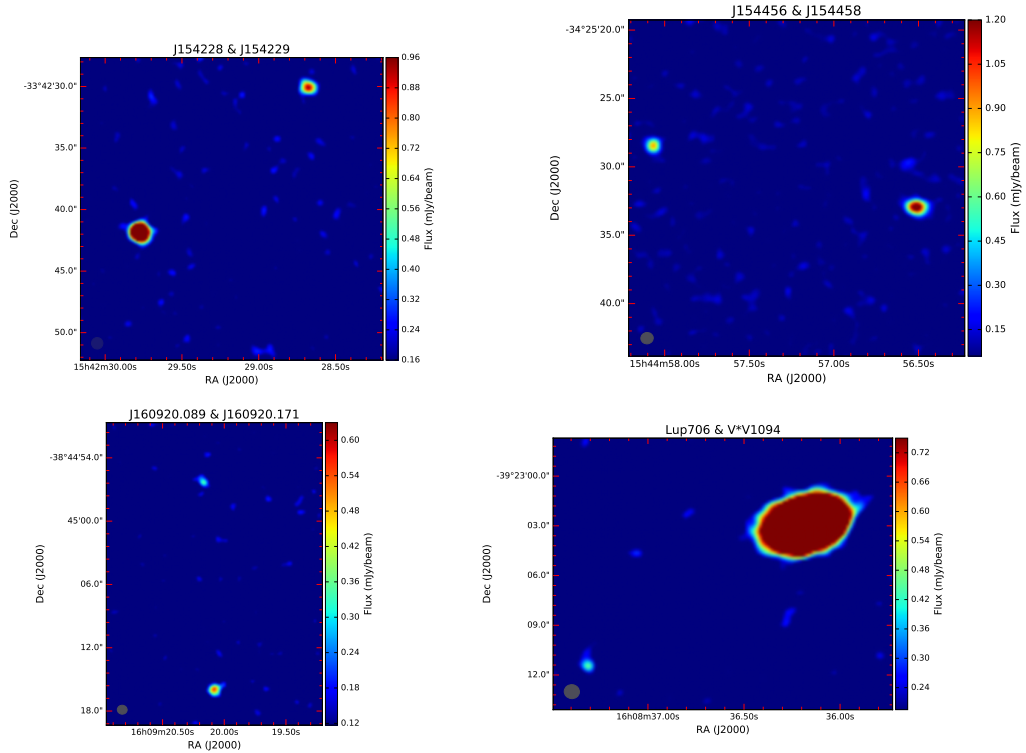


Figure 2.6: ALMA continuum emission maps at 1.3 mm wavelength for fields that show two sources inside the ALMA primary beam. Grey ellipse in the bottom-left corner represents the synthesized beam. Individual sources can be seen in more detail in Fig. 2.5

assumptions, we use the following formula from Hildebrand (1983):

$$M = \frac{S_{1.3} D^2}{B_{1.3}(T_d) \kappa_{1.3}}. \quad (2.1)$$

Here $S_{1.3}$ is the flux density in the region inside a 3σ contour level, D is the distance to the source as appears in Tab. 2.3, $B_{1.3}(T_d)$ is the Planck function at the observed wavelength (1.3 mm) at a certain temperature T_d , and $\kappa_{1.3}$ is the absorption coefficient obtained from Table 1 in Ossenkopf & Henning (1994) (column for thin ice mantles and density of 10^6 cm^{-3} , interpolated for a wavelength of 1.3 mm, which provides a value of $\kappa = 8.519 \times 10^{-3} \text{ cm}^2 \text{ g}^{-1}$ taking into account the aforementioned gas-to-dust ratio).

We used the SED (Fig. 2.7) for each source to classify its evolutionary state and then we adopted a temperature. For Class 0/I candidates we use a temperature of $15 \pm 1 \text{ K}$ based on the average temperature maps in Lupus 1 and 3 (Figure 2.2). These maps have been obtained from Herschel data (Teixeira et al., in prep.). Most of the ALMA detections in Lupus 1 lie in regions with temperatures close to 16.5 K, with only one source (the westernmost one) showing a value close to 19 K. In the case of the Lupus 3 sources, the reported temperatures vary between ~ 13 and 19 K, depending on their location within the cloud. Other examples of similar temperatures for Class 0/I in the literature can be found in Barrado et al. (2018) (15 K) for BDs or Stutz et al. (2010) ($17 \pm 1 \text{ K}$) for low mass stars. For less evolved (starless) sources

Table 2.4: Derived properties from ALMA and AzTEC observations

Name	Mass (ALMA) [M_{Jup}]	Mass (AzTEC) [M_{Jup}]	Size (AzTEC) [au]	Lupus cloud	Missing flux [%]
ALMA J153702.653-331924.92	0.86 ± 0.25	118.85 ± 28.65	5094	1	99.13
ALMA J153914.996-332907.62	0.63 ± 0.11	18.18 ± 2.80	3274	1	96.08
ALMA J154228.675-334230.18	5.43 ± 1.12	40.69 ± 9.81	< 2684	1	75.60
ALMA J154229.778-334231.86	3.53 ± 0.40	11.36 ± 1.75	3578	1	77.05
ALMA J154456.522-342532.99	4.78 ± 0.97	49.25 ± 11.87	3803	1	88.33
ALMA J154458.061-342528.51	2.71 ± 0.57	49.25 ± 11.87	3803	1	93.37
ALMA J154506.515-344326.15	0.50 ± 0.20	51.40 ± 12.39	3381	1	98.84
ALMA J154634.169-343301.90	1.43 ± 0.33	182.02 ± 43.88	7575	1	99.05
160658.7-390405	0.30 ± 0.04	-	-	3	-
ALMA J160804.168-390452.84	1.69 ± 0.43	-	-	3	-
160826.8-384101	1.08 ± 0.15	-	-	3	-
V*V1094 Sco	124.17 ± 7.16	82.11 ± 9.59	5032	3	-
Lup706	0.20 ± 0.10	148.88 ± 48.84	5032	3	99.85
Par-lup3-4	0.19 ± 0.05	-	-	3	-
SONYC-Lup3-7	0.18 ± 0.04	-	-	3	-
ALMA J160920.089-384515.92	1.75 ± 0.43	-	-	3	-
ALMA J160920.171-384456.40	1.77 ± 0.52	-	-	3	-
ALMA J160932.167-390832.27	1.21 ± 0.37	97.04 ± 25.64	4998	3	98.50
ALMA J161030.273-383154.52	1.36 ± 0.33	-	-	3	-

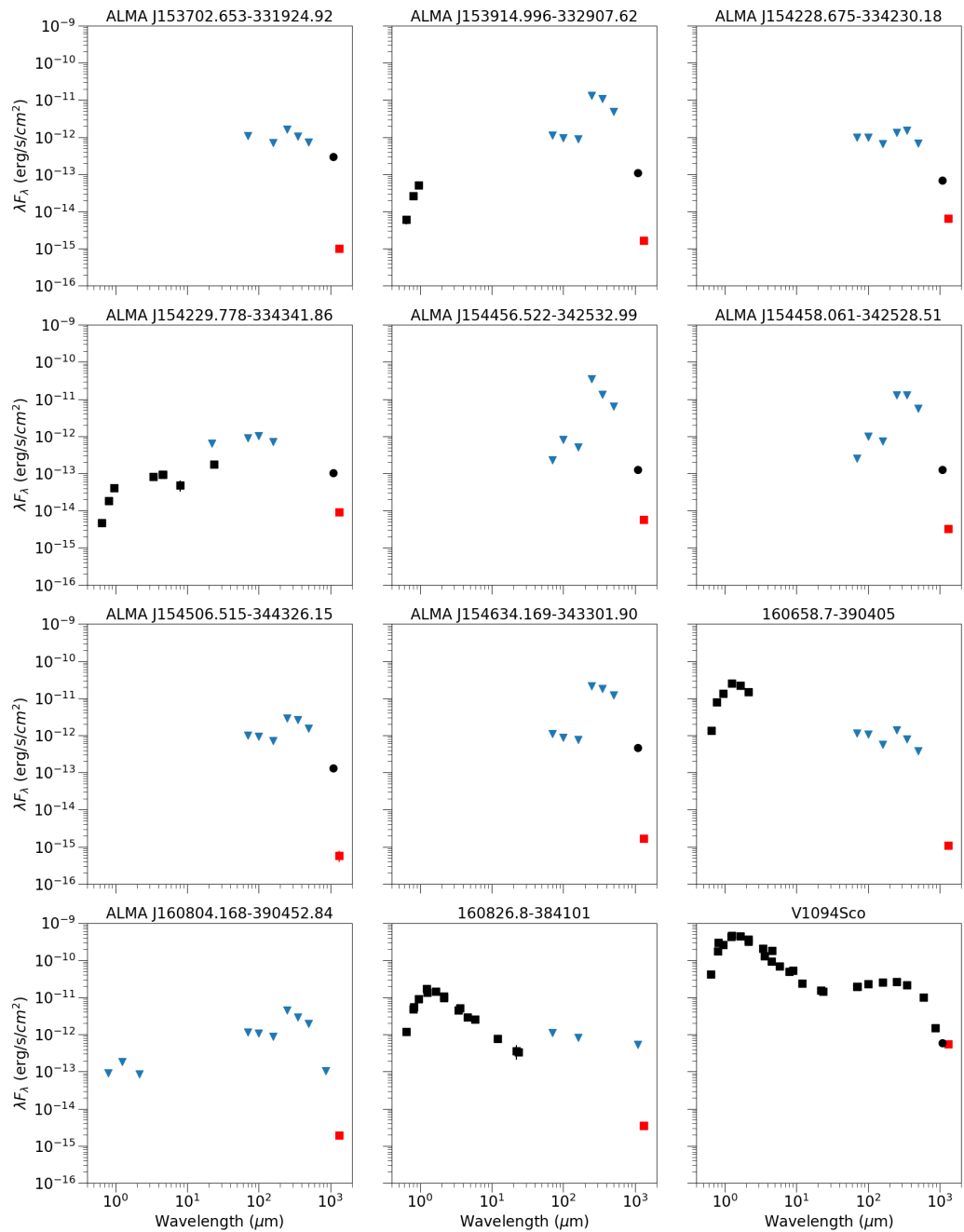
(ALMA detections without optical/IR counterparts) we use a temperature 9 ± 1 K as an intermediate value between ~ 8.5 - 10 (André et al. 2012, and references therein) or 7-13 K from previous works (Evans et al. 2001). For spectroscopically confirmed Class II BDs we used a temperature of 20 K (Pascucci et al. 2016). The temperature for V*V1094SCO came from the formula $T=25(L_*/L_\odot)^{0.25}$ K (Andrews et al. 2013) as it is in the solar-mass regime (see section 2.3.7).

Mass uncertainties have been calculated using the computed distance error, the flux error and the temperature error. The uncertainty in opacity is almost not affecting the derived mass value and therefore it is not included in the error propagation. Using the the opacity formula from Ward-Thompson et al. (2010), the masses would be larger by a factor of ~ 1.67 .

The range of masses is between 0.18 and 124.17 M_{Jup} . All the masses are in the planetary mass regime except for V*V1094 Sco which is a well known protostar with a protoplanetary disk surrounding it (Ansdell et al. 2016). The masses are represented in the Figure 2.8 excluding V*V1094 Sco.

2.3.4 AzTEC: Size and mass estimates

AzTEC masses are computed in the same fashion as described in Sec. 2.3.3. In Table 2.4 we show the mass estimates based on the ALMA continuum detections together with the mass estimation and the size of the AzTEC clumps, as well as a calculation of the missing flux in our ALMA observation. We also show the cloud membership for each object (eleven from Lupus 3 and eight from Lupus 1).



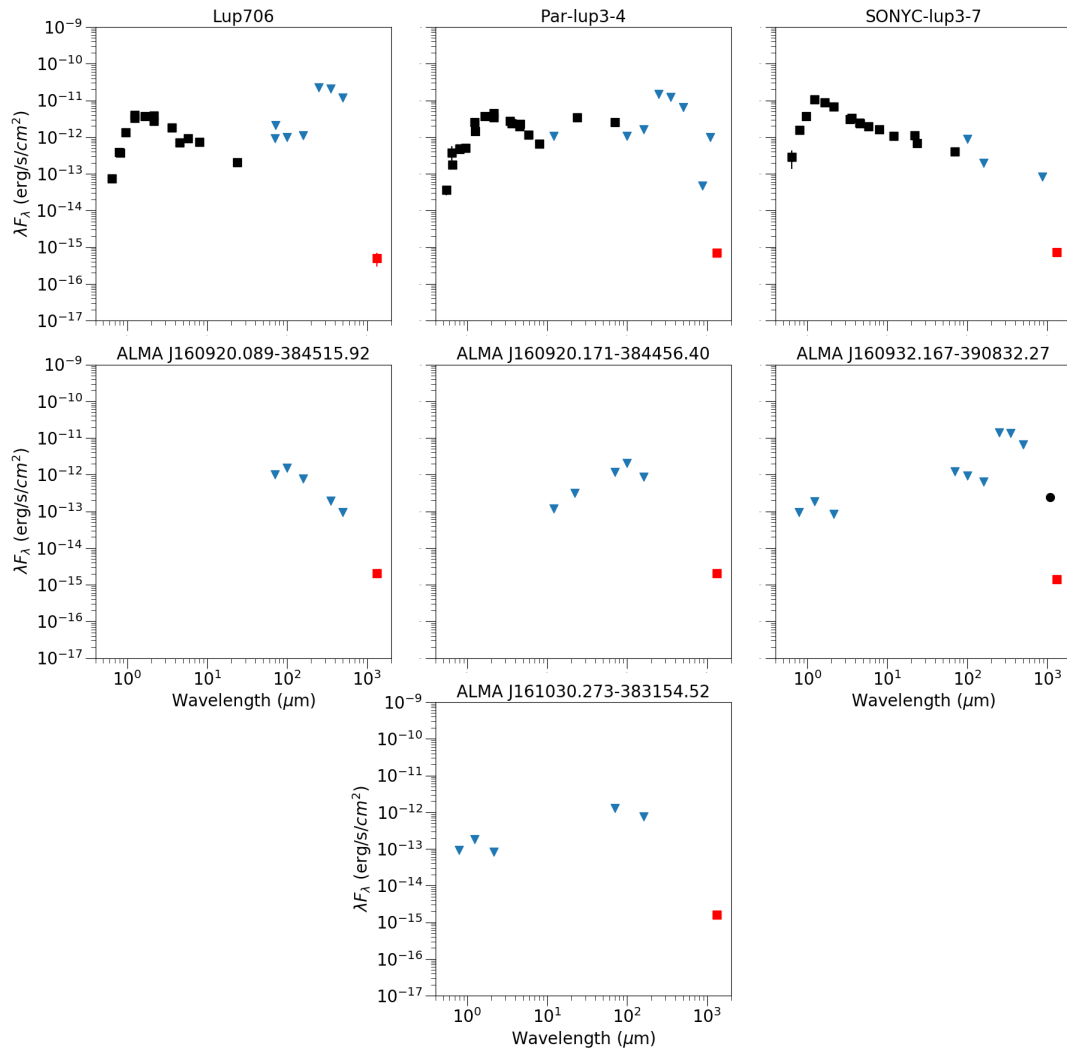


Figure 2.7: Spectral Energy Distribution for sources detected with ALMA at 1.3 mm. Red squares show ALMA fluxes. Black circles show AzTEC fluxes. Black squares show the fluxes from several telescopes WFI, DFOSC, DENIS, 2MASS, WISE, Spitzer, Akari, Herschel and LABOCA. Blue triangles represent upper limits.

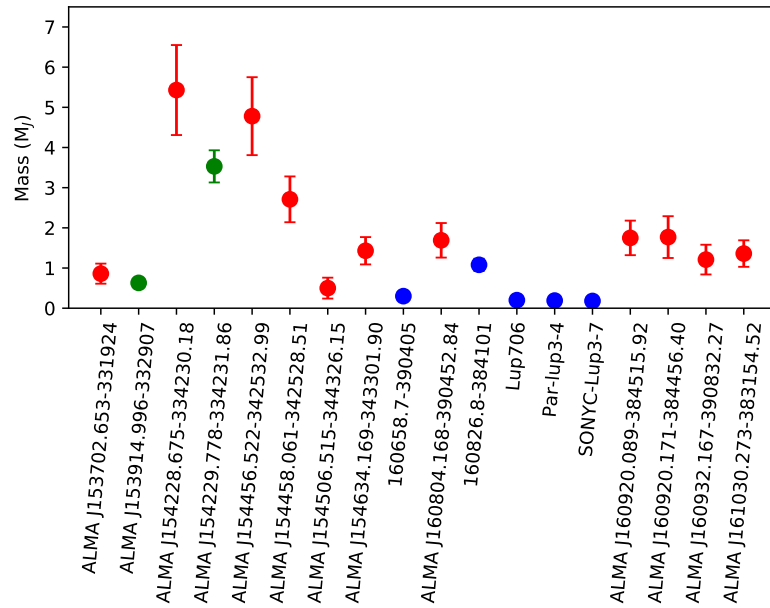


Figure 2.8: Mass estimates from the ALMA detections. We used a the temperature of 9 K for those sources without optical/IR counterparts (red points). $T = 15$ K for the three candidates classified as Class 0/I according to the SED (green points). $T = 20$ K for the the spectroscopically confirmed Class II objects (blue points).

In order to calculate the missing flux in the ALMA observations we first calculate the emission of the AzTEC clumps at the frequency of the ALMA observations. For that we assumed a emissivity index of $\beta = 2$. We use the same β value for the sources classified as Class II objects, although we warn this value could be smaller due to the possibility of dust processing. The missed flux estimation for V*V1094 Sco is not included in the table given the stellar nature of this source, which is not the scope of this paper. There is a large mass difference between the AzTEC clumps and the compact sources detected with ALMA, the latter providing much smaller mass values. The percentage of missed flux with ALMA ranges between 75.60 % to 99.85 %.

The masses of the AzTEC cores with no ALMA continuum detections are also given in Table 2.5. After a deeper review of the AzTEC map we conclude that they are stellar sources. Two out of the thirty three non-detections with ALMA are not spatially resolved clumps with AzTEC, while for the detected sources with ALMA there is no AzTEC clumps association/detection for 4 sources (160658.7-390405, SONYC-lup3-7, J1609200, J1609201) because they are more evolved sources and the parental cloud is expected to be almost dissipated or the parental cloud is too faint to be detected. The rest of the ALMA detections are associated with AzTEC spatially resolved clumps except for J154228, which is associated with a point-like source in the AzTEC maps. SONYC lup3-7 and J161030, detected with ALMA, where not covered by the AzTEC map.

Table 2.5: AzTEC: Densities (critical and observed) and radii (critical and observed) at a temperature of 9 K for the ALMA non-detections

Name	Mass [M_{\odot}]	n_{crit} [cm^{-3}]	n_{obs} [cm^{-3}]	R_{max} [au]	R_{obs} [au]	Dynamical state
AzTEC-lup1-99	0.0554	3.55×10^6	2.44×10^4	761.21	4003.20	stable
AzTEC-lup1-103	0.07	2.22×10^6	1.65×10^4	962.05	4926.37	stable
AzTEC-lup1-109	0.0854	1.49×10^6	1.48×10^4	1174.12	5457.73	stable
AzTEC-lup1-72	0.0968	1.16×10^6	1.74×10^4	1330.02	5395.62	stable
AzTEC-lup1-111	0.0675	2.39×10^6	1.54×10^4	926.94	4980.04	stable
AzTEC-lup1-57	0.0852	1.50×10^6	1.86×10^4	1171.31	5060.55	stable
AzTEC-lup1-67	0.109	9.24×10^5	1.35×10^4	1491.53	6098.73	stable
AzTEC-lup1-114	0.101	1.07×10^6	1.06×10^4	1386.20	6447.60	stable
AzTEC-lup1-84	0.0482	4.68×10^6	3.15×10^4	662.90	3512.48	stable
AzTEC-lup1-90	0.107	9.44×10^5	1.47×10^4	1476.08	5907.81	stable
AzTEC-lup1-40	0.13	6.43×10^5	2.16×10^4	1787.87	5542.84	stable
AzTEC-lup1-104	0.104	1.00×10^6	1.30×10^4	1432.54	6093.36	stable
AzTEC-lup1-101	0.11	8.99×10^5	1.19×10^4	1512.60	6384.73	stable
AzTEC-lup1-119	0.0616	2.87×10^6	1.90×10^4	846.89	4511.56	stable
AzTEC-lup1-124	0.106	9.69×10^5	1.05×10^4	1456.42	6582.55	stable
AzTEC-lup1-52	0.145	5.21×10^5	1.44×10^4	1987.30	6577.18	stable
AzTEC-lup1-54	0.275	1.44×10^5	9.62×10^3	3782.19	9315.25	stable
AzTEC-lup1-94	0.119	7.64×10^5	1.13×10^4	1640.40	6683.76	stable
AzTEC-lup1-71	0.0832	1.57×10^6	2.16×10^4	1143.23	4772.25	stable
AzTEC-lup1-123	0.048	4.72×10^6	2.31×10^4	660.09	3885.89	stable
AzTEC-lup3-15	0.12	7.62×10^5	1.11×10^4	1642.79	6724.35	stable
AzTEC-lup3-20	0.0768	1.84×10^6	1.27×10^4	1055.86	5544.33	stable
AzTEC-lup3-12	0.279	1.02×10^5	1.34×10^4	4263.63	8385.90	stable
AzTEC-lup3-10	0.0343	6.73×10^6	4.89×10^4	524.41	2708.12	stable
AzTEC-lup3-5	1.32	4.55×10^3	3.24×10^4	20158.08	10477.35	unstable
AzTEC-lup3-14	0.133	6.14×10^5	1.12×10^4	1830.03	6951.41	stable
AzTEC-lup3-19	0.0374	5.69×10^6	5.32×10^4	570.50	2708.12	stable
AzTEC-lup3-18	1.02	7.70×10^3	4.34×10^4	15506.70	8710.88	unstable
AzTEC-lup3-4	1.01	7.74×10^3	3.05×10^4	15459.03	9793.35	unstable
AzTEC-lup3-13	0.537	2.75×10^4	1.67×10^4	8201.49	9684.25	stable
AzTEC-lup3-9	0.216	1.70×10^5	1.95×10^4	3295.85	6790.43	stable
AzTEC-lup3-21	0.0934	9.11×10^5	1.83×10^4	1425.45	5239.06	stable
AzTEC-lup3-16	0.0785	1.77×10^6	1.45×10^4	1078.26	5349.32	stable

Table 2.6: Bolometric temperature and bolometric luminosity for those ALMA detections with more than three points in their SED.

Name	Temperature [K]	Luminosity [L_{\odot}]
J154229	$64.59^{+2.42}_{-1.68}$	$0.00436^{+0.00079}_{-0.00080}$
160658	2587	0.02043
160826	$1410.60^{+9.45}_{-4.59}$	$0.02678^{+0.00089}_{-0.00047}$
V*V1094 Sco	$2019.03^{+24.74}_{-138.76}$	$0.56004^{+0.00089}_{-0.00047}$
Lup706	$415.45^{+9.77}_{-13.86}$	$0.02896^{+0.00271}_{-0.00278}$
Par-Lup3-4	$405.63^{+21.24}_{-23.77}$	$0.01895^{+0.00062}_{-0.00061}$
SONYC Lup3-7	$1959.16^{+15.96}_{-14.35}$	$0.00953^{+0.00036}_{-0.00037}$

2.3.5 Spectral energy distribution

Optical/IR/Radio counterpart association

To associate the ALMA detections with optical/IR/Radio sources, we searched for counterparts at distances smaller than the total pointing error. The total pointing error is calculated as the square root of the quadratic sum of the pointing errors between ALMA and the counterpart's instrument. The pointing errors of instruments are between 1 and 10 arcsec. The pointing errors for each instrument are listed in Tab. 2.1.

After this selection by separation, we proceeded with an inspection of the images and constructed SEDs, checking if there are clear detections, and if the SED's shapes correspond to one of young stellar objects.

Bolometric luminosity and temperature

We calculate the bolometric luminosity (L_{bol}) and the bolometric temperature (T_{bol}) for each source (see Tab. 2.6). We selected those sources with more than three points in the IR/optical wavelength detected along the SED. This group of sources are: J14229, 160658, 160826, V*V1094 Sco, Lup706, Par-Lup3-4 and SONYC-lup3-7. To calculate L_{bol} we used formula (1) in [Enoch et al. \(2009\)](#), and for T_{bol} we used formula (2) from the same paper and the mean frequency from [Myers & Ladd \(1993\)](#). In addition, to properly classify Class 0, I or II/III objects we used the definition in [Chen et al. \(1995\)](#) where Class 0 systems have T_{bol} below 70 K, Class I sources have temperatures between 70 and 650 K, and Class II/III sources temperatures exceeding 650 K.

One source (J154229) is at the boundary between Class 0 and Class I objects. Par-Lup3-4 and Lup706 appear in the Class I regime, but both sources have been previously classified as Class II in the literature. These two sources are mentioned in [Alcalá et al. \(2014\)](#) having the lowest luminosities among all the Lupus YSOs. The

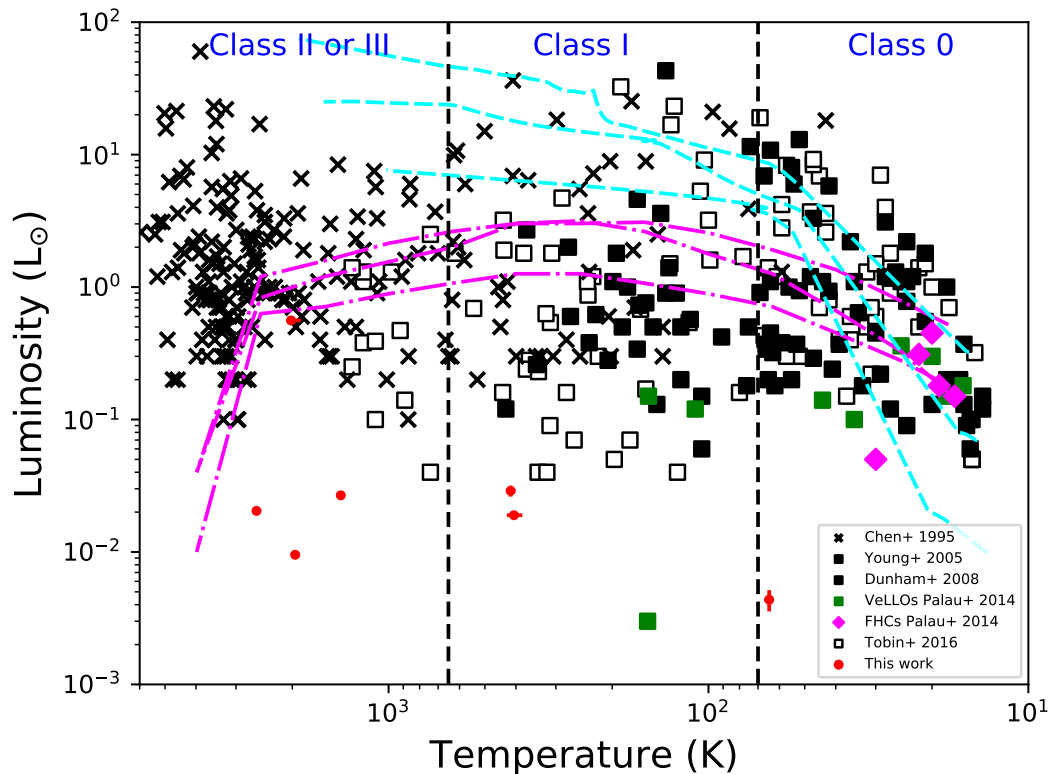


Figure 2.9: Bolometric luminosity versus bolometric temperature. Black squares represent sources from [Young & Evans \(2005\)](#) and [Dunham et al. \(2008\)](#) which show evidence of embedded low luminosity sources. Sources in Perseus from [Tobin et al. \(2016\)](#) are represented as open squares. Young Taurus ([Chen et al. 1995](#)) sources are displayed as black crosses. Green squares are known VeLLOs and the magenta diamonds are the First Hydrostatic Cores from [Palau et al. \(2014\)](#). The vertical dashed lines mark the Class 0–I and Class I–II bolometric temperature boundaries from [Chen et al. \(1995\)](#). The cyan short dashed lines represent the evolutionary tracks for the three models with different masses considered by [Young & Evans \(2005\)](#). The magenta, dotted and dot-dashed lines show the evolutionary tracks for three models considered by [Myers et al. \(1998\)](#). Red points including uncertainty represent values obtained in this papers.

subluminous nature of Par-Lup3-4 has been explained by [Huélamo et al. \(2010\)](#) using models that predict a disk inclination of $81 \pm 6^\circ$. The remaining sources (160658, 160826, V*V1094 Sco and SONYC-lup3-7) can be classified as Class II or III objects. Figure 2.9 shows the position in the $T_{\text{bol}}-L_{\text{bol}}$ diagram of the mentioned sources along with objects from previous studies in the regions of Perseus and Taurus.

The sources we study in this work have lower luminosities than other BD candidates from previous works, as shown in Fig 2.9, with the exception of one VeLLO from [Palau et al. \(2014\)](#). We are detecting the least luminous young pre-substellar candidates so far, thanks to the sensitivity of ALMA and the close proximity of the Lupus complex. This allows us to discover a new Class 0 substellar candidate, a type of object for which confirmed detections are really scarce (L328-IRS ([Lee et al. 2009, 2013](#)) or ICM348-SSM2E ([Palau et al. 2014](#))). Class I sources are also difficult to detect, and here we provide two new candidates to be added to the list of Class I candidate sources such as L1148-IRS ([Kauffmann et al. 2011](#)) or J042118 ([Palau et al.](#)

2012). The ALMA detection of the Class II sources is providing a new point in the SED that helps us to better constrain its position in the $T_{\text{bol}}-L_{\text{bol}}$ diagram.

Classification

We classified the sources according to their SED in the following categories: ALMA detections without optical/IR counterparts (pre-substellar phase), Class 0, Class I and Class II sources. For this classification we use the α_{IR} slope (Williams & Cieza 2011, and references therein), as well as the T_{bol} and L_{bol} values described in section 2.3.5. For all sources we double-checked previous classifications in the literature if available.

2.3.6 ALMA sources without optical/IR counterparts

The following eleven sources detected in our ALMA survey have no optical/infrared counterparts at a distance smaller than 3 arcsec: J153702, J154228, J154456, J154458, J154506, J154634, J160804, J1609200, J1609201, J160932, J161030. Five of these sources (J153702, J160804, J1609200, J1609201 and J161030) were serendipitously detected inside the ALMA primary beam at a distance greater than 3 arcsec from the nominal position of the spectroscopically confirmed Class II sources originally targeted. The remaining six sources (J154228, J154456, J154458, J154506, J154634, and J160932) are detected inside the ALMA primary beam of the observed pre-substellar candidates from our AzTEC catalog, and they have no optical/IR counterpart.

J153702 is located at a distance of 6.87 arcsec from the Class II object 153703.1-331927 (ALMA phase center). There are no Gaia detections at these positions, therefore we do not have proper motion information to check if they were gravitationally bound. J160804 is at a distance of 8.03 arcsec from the Class II source 160804.8-390449, the source that was originally targeted in our survey. Gaia proper motions measured for 160804.8-390449 suggest they are likely independent sources. J161030 is at a distance of 4.96 arcsec from 161030.6-383151, the source originally targeted by ALMA. There is no Gaia detection reported. J1609200 and J1609201 are two sources detected in the same ALMA field of view (see Fig. 2.6), located at 10.54 and 15.74 arcsec distance respectively from the phase center, which was the position of the Class II source 160920.8-384510. There are optical/infrared counterparts close to J1609201, including Gaia measurements, but the high precision astrometry of Gaia as well as the accurate absolute astrometry for this source reveals that the counterparts are not associated with J1609201. The Gaia counterpart is 2MASS 16092031-3844568 (Cutri et al. 2003).

The remaining sources are seen inside the ALMA primary beam centered at the AzTEC pre-substellar candidates of our sample. J154228 is located 9.7 arcsec from the ALMA phase center. The NED catalogue shows the closest object to the source has an extragalactic nature, but it is located at a distance of 3.72 arcsec, which makes its physical association unlikely given the absolute position accuracy of ALMA. J154456 and J154458 fall inside the same primary beam. The separation between

these two sources is 19.56 arcsec, and they are located at 6.2 and 13.4 arcsec respectively from the phase center. The closest optical object found is SSTS2 J154456.77-342532.3 at 3.1 arcsec and 16.4 arcsec distance from J154456 and J154458. The ALMA detection of J154456 is spatially resolved with a Gaussian deconvolved size of 0.8 ± 0.06 arcsec \times 0.3 ± 0.08 arcsec. J154506, J160932, and J154634 are located at a distance of 12.0, 11.9, and 14.8 arcsec respectively from their phase center. Extended cloud emission is seen in CO(2-1) surrounding J154634 at velocities between 3.4 to 5.3 km/s, but no compact gas detection is observed at the position of this source.

At the distance of Lupus, we found that the ALMA compact continuum emission mentioned above provides substellar masses below $10 M_{\text{Jup}}$, well inside the substellar regime independent of the values of temperature or opacity coefficient we adopt. We checked possible extragalactic contaminants in the NASA/IPAC Extragalactic Database and we found no clear detections associated with any of the detected positions. All these sources except J153702 and J161030 are located well inside or quite close to the Lupus dust filaments as seen in the Herschel and AzTEC maps (see Fig. 2.1 and 2.2). Therefore, they are probably associated with the Lupus molecular clouds and we classify them as pre-BD candidates or deeply embedded proto-BD candidates. Future gas detections at the position of these candidates and at a velocity near the V_{LSR} of the respective Lupus molecular cloud will confirm the galactic nature and the membership of each source to the complex.

2.3.7 ALMA sources with counterparts

The sources described in this subsection have either optical and/or infrared counterparts. Using the classification tools described above (SED, α_{IR} slope, T_{bol} and L_{bol}) we make an attempt to classify their state of evolution, considering the uncertainty in their physical association to the Lupus clouds, and the incomplete SEDs for most of them. We obtain one new Class 0/I proto-BD candidate, two Class I proto-BD candidates (or pre-BDs if their optical counterparts are not associated with them), a new Class II substellar candidate and the confirmation of six Class II substellar objects previously known.

ALMA J153914.996-332907.62

J153914 has not been previously reported in the literature. We detect an ALMA continuum point-like source with a 7σ detection (Fig. 2.5) of $0.63 M_{\text{Jup}}$. This source has WFI optical counterparts at 0.71 arcsec distance from the ALMA detection. There are no IR counterparts associated with this source, which complicates the confirmation of the physical association of the WFI source with the ALMA source. If confirmed, this source would be a Class I proto-BD candidate. On the contrary, if there is not such an association then it would be classified as a pre-BD or deeply embedded proto-BD candidate. Future infrared observations are needed to disentangle this dichotomy.

ALMA J154229.778-334231.86

J154229 (Fig. 2.5) is detected and spatially resolved in this work for the first time. We report a 26σ detection and a size of 0.77×0.64 arcsec, with a mass is $3.53 \pm 0.40 M_J$. We found several counterparts at other wavelengths (WFI, WISE, IRAC/SPITZER, MIPS/SPITZER). All the counterparts are compatible among them. Offsets are provided in Appendix B. In the NED catalogue there is a nearby source located at 0.24 arcsec distance and classified as infrared source (IrS), whose extragalactic nature is not confirmed. The J154229 SED is compatible with a subluminescent Class I source, but the bolometric temperature indicates that it is most likely a Class 0 object, very close to the boundary to Class I. Therefore we classify it as a proto-BD candidate in a transition stage between Class 0 to Class I (see Tab. 2.6). J154229 SED is similar to the Taurus proto-BD Class 0/I candidate J041757-B found in Lupus by Palau et al. (2012).

The pre-BD candidate J154228 is located inside the same primary beam at a distance of 17.9 arcsec. As a first order approximation using the projected distance and assuming that one of the sources was ejected from the other one at an ejection velocity of ~ 1 km/s (Basu & Vorobyov 2012) we obtain that these sources could have been bound 13×10^3 years ago. This age is completely in agreement with brown dwarf formation theories, but it needs to be observationally confirmed.

160658.7 -390405

This source was classified for the first time by Comerón et al. (2009) as a Class II object with $T_{\text{eff}}=2800$ K, a mass of $0.06 M_{\odot}$ and an age younger than 1 Myr. The ALMA detection (Fig. 2.5) is near the position of the WFI object (at 3 arcsec distance), which according to the criterion established in section 2.3.5 points to a physical association. Emission at 1.3 mm is detected at 7σ and the disk mass is $0.30 \pm 0.04 M_J$ at a distance of 156.96 ± 3.37 pc. The bolometric temperature obtained from the SED is ~ 2878 K, which lies in the Class II regime in agreement with previous classifications.

160826.8 -384101

This is a spectroscopically confirmed Class II source in Lupus 3 (Comerón et al. 2009). The central object has an $T_{\text{eff}}=2900$ K and a mass of $0.06 M_{\odot}$ (Comerón et al. 2009). ALMA continuum emission at 1.3 mm is detected at 26σ (Fig. 2.5) and it is not spatially resolved. The disk mass is $1.08 \pm 0.15 M_J$ at a distance of 165.27 ± 3.54 pc. The bolometric temperature is ~ 1411 K, in the Class II range. The NED database classifies this object as an Infrared source (IRs), however the classification in this database does not necessarily imply that it is an extragalactic source, but simply that it has been detected in the infrared regime by Spitzer.

V*V1094 Sco

V*V1094 Sco is a Class II YSO in the stellar mass regime (Frasca et al. 2017) discovered by Krautter et al. (1997). Our high signal-to-noise ratio image spatially resolves the dust disk. We estimated a disk mass of $124 \pm 7 M_J$ and the disk temperature is 22.53 K, at a distance of 153.71 ± 1.09 pc. The object is extensively discussed in several papers (Baraffe et al. 2015; Alcalá et al. 2017; Frasca et al. 2017). The central protostar has $T_{\text{eff}} = 4205 \pm 193$ K with a mass of $1.10 M_{\odot}$ and it is classified as K6 (Frasca et al. 2017). We found several counterparts from the optical to the IR (WFI, DENIS, 2MASS, WISE, Spitzer-MIPS, Spitzer-IRAC, Spitzer-MIPS, SPIRE, PACS, LABOCA, akari). A previous study in the mm using AzTEC shows that the disk should be between the planetesimal formation phase and the sedimentation in the midplane stage (Tsukagoshi et al. 2011).

Lup706

This is a spectroscopically confirmed Class II substellar object, previously discovered and classified as a BD (López Martí et al. 2005). We report a 5σ non spatially resolved detection (Fig. 2.5). The integrated flux is $531 \pm 35 \mu\text{Jy}$. The mass of the disk is $0.20 \pm 0.10 M_J$ at a distance of 191.13 ± 29.13 pc. The distance could show that it is not part of the complex, but taking the error of the distance into account it remains a possible cloud member. The distance in the field of view between Lup706 and V*V1094 Sco is 15.92 arcsec, although in Tab. 2.3 the minimum distance between both sources is 7.2 parsec, therefore the possibility that Lup706 formed in the protoplanetary disk of V*V1094 and subsequently ejected seems to be minimal. The central object has T_{eff} of 2750 K and a mass of $0.06^{+0.03}_{-0.02} M_{\odot}$ and is classified as M7.5 BD (Alcalá et al. 2014; Mužić et al. 2014). Lup706 has been classified as a Class II object (Alcalá et al. 2014, 2017), the same classification that we obtained from the SED. Although the bolometric temperature is ~ 415 K, below the Class II source limit, it is possible that, as we see in Par-Lup3-4, the inclination of the surrounding disk is responsible for this low temperature. Future SED modelling could give us more information about the inclination angle.

Par-Lup3-4

Par-Lup3-4 (Fig. 2.5) was discovered by Nakajima et al. (2000) and confirmed spectroscopically (Comerón et al. 2003). It is at the boundary between VLM stars and BDs, with a mass of $0.13 M_{\odot}$, M4.5 spectral type and $T_{\text{eff}} = 3089 \pm 246$ K (Alcalá et al. 2017; Manara et al. 2013; Frasca et al. 2017). We report a more than 5σ detection which is spatially unresolved. The mass of the disk is $0.19 \pm 0.05 M_J$ at a distance of 155.2 ± 14.45 pc. We also detect CO(2-1) gas emission associated with this source at velocities close to the V_{LSR} of Lupus, which confirms its association to the molecular cloud. Par-Lup3-4 is classified as Class II source in the literature, with an almost edge-on disk (Huélamo et al. 2010). The bolometric temperature is ~ 405 K, in the Class I regime, but the source is under-luminous (Comerón et al. 2003).

SONYC-lup3-7

This is a spectroscopically confirmed Class II substellar source in Lupus 3 discussed in Alcalá et al. (2014) and Mužić et al. (2014). Our ALMA data (Fig. 2.5) show a non resolved object detected at 4 sigma with a disk mass of $0.18 \pm 0.04 M_{\text{Jup}}$ at a distance of 151.12 ± 6.38 pc. The bolometric temperature obtained from the SED is ~ 1959 K. Alcalá et al. (2014) and Mužić et al. (2014) found that the central object has a temperature of 2600 to 2850 K and a mass of $0.03 \pm 0.01 M_{\odot}$. We also classify the source as a Class II, based on its SED.

2.3.8 VeLLOs

VeLLOs are sources in which the internal luminosity is below $0.1 L_{\odot}$. We used the formula $L_{\text{int}} = 3.3 \times 10^8 F_{70}^{0.94} L_{\odot}$ (Dunham et al. 2008), where F_{70} is the flux at $70 \mu\text{m}$. For almost all the objects in our sample we only have upper limits for that specific wavelength. Using these upper limits we find that all the sources are below the threshold, so we can classify the whole sample as VeLLOs.

2.4 Discussion

2.4.1 Spatial distribution: detections vs non-detection

The spatial distribution of the Lupus 1 objects is shown in Fig. 2.1. Almost all the sources are in the main filament. Only 2 non-detected and one core detected with ALMA are not located in the main filament. There are also several non-detections in a secondary dust filament. The source ALMA153702 is out of the filament, but was serendipitously detected when we pointed to a spectroscopically confirmed Class II BD. For Lupus 3 the distribution is slightly different (right panel in Fig. 2.1). There are several sources along the main filament, including ALMA detections without optical/IR counterparts such as J160804 or 160932. However, there are also some of the ALMA detections located at the outskirts of the filament (J1609200, J1609201 and J161030). Finally, 9 surveyed positions are located at a considerable distance from the center of the filament, distributed along the whole map. We do not see any specific preferred area where AzTEC sources detected with ALMA tend to cluster.

2.4.2 Detection rate of pre- and proto-BD candidates and large scale core properties

The ALMA detection rate of the whole sample was 23.4 % (15 of the 64 pointings), being 12.5 % (5 of 40) if we reduce the sample to the initial classification of 33 pre-stellar and 7 Class 0 and I objects we surveyed. The ALMA experiment was entirely designed to detect faint sources even in the worst case scenario where all the emission was extended in an area equivalent to the ALMA largest angular scale

(~ 11 arcsec). Thus, we built our sample with AzTEC cores whose peak intensities were in the range of 30-100 mJy, with a Gaussian convolved beam size of ~ 30 arcsec. We adopted a very conservative approach in which the emission from the dusty envelope/disk surrounding a very young brown dwarf could have a size as large as the ALMA LAS (11 arcsec), i.e., ~ 1650 au at ~ 150 pc, and an uniform distribution over that envelope. Considering the ALMA synthesized beam of our observations (~ 0.85 arcsec) and also that our observations have sufficient rms-noise level to detect sources at 5σ level, this means that in the case of non-detections it was a matter of source size more than sensitivity, suggesting the AzTEC clump material is distributed mainly at large scales. This is in agreement with the fact that we are filtering most of the extended emission in our ALMA observations.

2.4.3 Evolution of the AzTEC starless cores: Final mass of the pre-BD candidates

Following the starless core scenario we do an estimation of the final masses of the central compact object assuming a core formation efficiency in the substellar regime of 30% (and a temperature of 9 K), similar to the one observed in low mass cores (Motte et al. 1998). Therefore, for the pre-BD candidates with AzTEC counterparts, we add 30% of the AzTEC clump mass to the mass obtained from our ALMA detection (Fig 2.10). As a result we obtain that all these pre-BD candidates might be in the substellar regime with final mass values of 40.5 ± 9.6 , 19.0 ± 3.5 , 21.2 ± 4.1 , 19.1 ± 4.0 , 17.6 ± 4.1 , 62.1 ± 14.6 , $33.6 \pm 8.6 M_{\text{Jup}}$ for J153702, J154228, J1544458, J154506, J154634 and J160932, respectively. We conclude that the seven ALMA compact sources detected inside the seven AzTEC clumps of our sample and without counterparts at shorter wavelengths, could yield future substellar objects.

2.4.4 Nature of ALMA detections without infrared counterparts

Infall according to turbulent fragmentation

The theory of turbulent fragmentation (Padoan & Nordlund 2004), is based on collapse due to externally driven supersonic turbulence. The critical mass for the collapse of a Bonnor-Ebert sphere (Bonnor 1956) is defined as:

$$M_{\text{BE}} = 3.3M_{\odot} \left(\frac{T}{10\text{K}} \right)^{3/2} \left(\frac{n_{\text{crit}}}{10^3 \text{cm}^{-3}} \right)^{-1/2}, \quad (2.2)$$

where T is the temperature in K and n_{crit} is the critical density in cm^{-3} . For the next calculations we will assume the Bonnor-Ebert mass is the one from AzTEC cores or ALMA compact detections. The uncertainty in the Bonnor-Ebert mass sphere is estimated considering the mass uncertainty in Tab. 2.4 and the temperature error with a fixed value of 1 K, as it was done in Sect. 2.3.3. The critical radii (R_{crit}) can be simplified as

$$R_{\text{crit}} = \left(\frac{M_{2.83} \times 10^{16}}{n_{\text{crit}}} \right)^{1/3}, \quad (2.3)$$

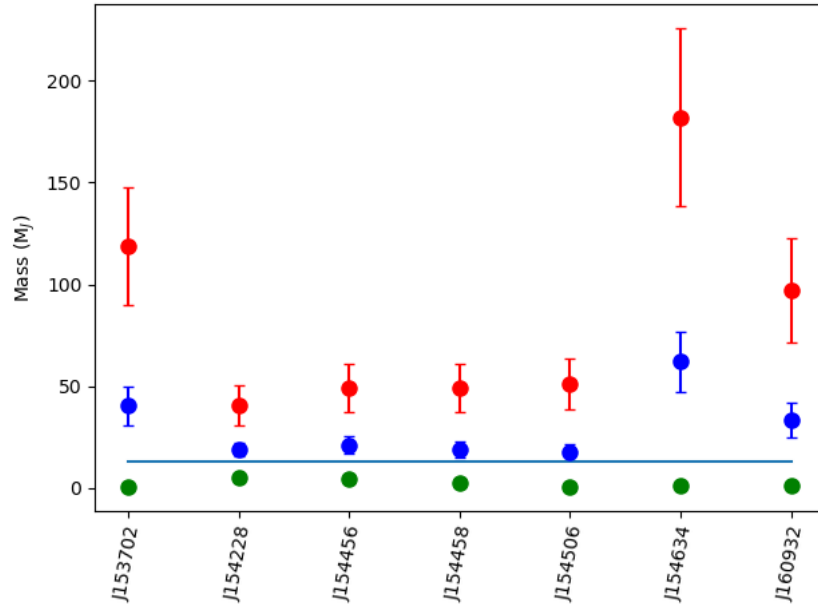


Figure 2.10: Mass of the ALMA pre-substellar candidates without optical/infrared counterparts at a temperature of 9K. Red points are the AzTEC mass. Green points are the ALMA mass. Blue points are the assumed final mass as a combination of the ALMA mass and the AzTEC mass assuming a core efficiency of 30%. Horizontal line marks the limit between planets and BDs.

where M is the mass of the source in solar masses.

The observed density (n_{obs}) is the ratio between the hydrogen column density and the linear size of the source, and it is calculated considering the mass of the source estimated from the observations and the size of the emitting region. For those ALMA sources that are not spatially resolved we use the synthesized beam size as an upper limit to their size.

According to this theory, cores with a density smaller than the critical one ($n_{\text{obs}} < n_{\text{crit}}$) should be stable transient cores. On the contrary, if the density of the core is greater than the critical density ($n_{\text{obs}} > n_{\text{crit}}$), the core is gravitationally unstable and expected to be in the pre-stellar phase. The relation between the average radius of the source (R_{obs}) and the maximum radius size to reach the critical density value (R_{crit}) is also used to infer the energetic state of sources. Spatially resolved sources with R_{obs} smaller than R_{crit} indicate that the core is unstable. For non-resolved sources, R_{crit} sets a boundary between stable cores ($R_{\text{obs}} > R_{\text{crit}}$) and unstable ones ($R_{\text{obs}} < R_{\text{crit}}$).

We calculate the critical density and the observed density for the ALMA compact sources without optical/infrared counterparts (pre-BD candidates) using two values of temperature: $T=9$ K, more characteristic of pre-substellar cores (Table 2.7), and $T=15$ K for deeply embedded protostars (Table 2.8), as we did in Sect. 2.3.3. We do the same calculation for the hosting AzTEC clumps (see Table 2.9 and 2.10).

The unresolved ALMA sources are supposed to be collapsing if their radius is smaller than the values given in Table 2.7. For the resolved source J154456 we obtained a density and size that indicates that it is infalling.

Table 2.7: ALMA: Densities (critical and observed) and radii (critical and observed) at a temperature of 9 K

Name	n_{crit} [cm ⁻³] ± %	n_{obs} [cm ⁻³] ± %	R_{max} [au]	R_{obs} [au]	Dynamical state ¹
J153702	$1.2 \times 10^{10} \pm 511$	$> 6.3 \times 10^7$	13 ± 21	< 72	stable?
J154228	$3.0 \times 10^9 \pm 373$	$> 1.2 \times 10^9$	94 ± 47	< 49	unstable?
J154456	$3.8 \times 10^8 \pm 366$	$1.7 \times 10^9 \pm 101$	70 ± 85	43	unstable
J154458	$1.2 \times 10^9 \pm 384$	$> 2.5 \times 10^8$	40 ± 51	< 67	unstable?
J154506	$3.5 \times 10^{10} \pm 721$	$> 4.3 \times 10^7$	7 ± 17	< 68	stable?
J154634	$4.2 \times 10^9 \pm 410$	$> 1.2 \times 10^8$	21 ± 29	< 68	stable?
J160804	$3.0 \times 10^9 \pm 451$	$> 1.4 \times 10^8$	25 ± 37	< 69	stable?
J1609200	$2.8 \times 10^9 \pm 440$	$> 1.1 \times 10^8$	26 ± 37	< 75	stable?
J1609201	$2.8 \times 10^9 \pm 531$	$> 1.5 \times 10^8$	26 ± 46	< 69	stable?
J160932	$1.1 \times 10^{10} \pm 654$	$> 5.7 \times 10^7$	13 ± 28	< 75	stable?
J161030	$4.7 \times 10^9 \pm 439$	$> 1.1 \times 10^8$	20 ± 29	< 69	stable?

¹ Stable vs. infalling described in Section 2.4.4, the question mark shows that we are showing upper-limits.

Table 2.8: ALMA: Densities (critical and observed) and radii (critical and observed) at a temperature of 15 K

Name	n_{crit} [cm ⁻³] ± %	n_{obs} [cm ⁻³] ± %	R_{max} [au]	R_{obs} [au]	Dynamical state
J153702	$2.6 \times 10^{11} \pm 687$	$> 2.9 \times 10^7$	3 ± 8	< 72	stable?
J154228	$6.6 \times 10^9 \pm 366$	$> 1.8 \times 10^8$	92 ± 19	< 49	stable?
J154456	$8.6 \times 10^9 \pm 345$	$7.6 \times 10^8 \pm 92$	19 ± 22	43	stable
J154458	$2.7 \times 10^{10} \pm 396$	$> 1.1 \times 10^8$	11 ± 14	< 67	stable?
J154506	$7.9 \times 10^{11} \pm 1091$	$> 1.9 \times 10^7$	2 ± 7	< 68	stable?
J154634	$9.5 \times 10^{10} \pm 463$	$> 5.5 \times 10^7$	6 ± 9	< 68	stable?
J160804	$6.8 \times 10^{10} \pm 560$	$> 6.4 \times 10^7$	7 ± 13	< 69	stable?
J1609200	$6.4 \times 10^{10} \pm 534$	$> 5.1 \times 10^7$	7 ± 12	< 75	stable?
J1609201	$6.2 \times 10^{10} \pm 729$	$> 6.6 \times 10^7$	7 ± 17	< 69	stable?
J160932	$2.4 \times 10^{11} \pm 968$	$> 2.6 \times 10^7$	4 ± 11	< 75	stable?
J161030	$1.1 \times 10^{11} \pm 532$	$> 5.1 \times 10^7$	5 ± 10	< 69	stable?

Table 2.9: AzTEC: Densities (critical and observed) and radii (critical and observed) at a temperature of 9 K

Name	n_{crit} [cm ⁻³] ± %	n_{obs} [cm ⁻³] ± %	R_{max} [au]	R_{obs} [au]	Dynamical state
J153702	$8.5 \times 10^5 \pm 483$	$2.4 \times 10^4 \pm 33$	1559 ± 2512	5094	stable
J154228	$7.2 \times 10^6 \pm 483$	$> 5.7 \times 10^4$	534 ± 860	< 2684	stable?
J154456	$4.9 \times 10^6 \pm 483$	$2.4 \times 10^4 \pm 33$	646 ± 1041	3803	stable
J154506	$4.5 \times 10^6 \pm 483$	$3.6 \times 10^4 \pm 33$	674 ± 1086	3381	stable
J154634	$3.6 \times 10^5 \pm 483$	$1.1 \times 10^4 \pm 33$	2388 ± 3847	7575	stable
J160932	$1.3 \times 10^6 \pm 529$	$2.1 \times 10^4 \pm 45$	1273 ± 2247	4998	stable

Table 2.10: AzTEC: Densities (critical and observed) and radii (critical and observed) at a temperature of 15 K

Name	n_{crit} [cm ⁻³] ± %	n_{obs} [cm ⁻³] ± %	R_{max} [au]	R_{obs} [au]	Dynamical state
J153702	$1.6 \times 10^7 \pm 462$	$1.0 \times 10^4 \pm 24$	441 ± 679	5094	stable
J154228	$1.4 \times 10^8 \pm 462$	$> 2.4 \times 10^4$	151 ± 232	< 2684	stable?
J154456	$9.2 \times 10^7 \pm 462$	$1.0 \times 10^4 \pm 24$	183 ± 281	3803	stable
J154506	$8.5 \times 10^7 \pm 462$	$1.5 \times 10^4 \pm 24$	191 ± 294	3381	stable
J154634	$6.8 \times 10^6 \pm 462$	$4.8 \times 10^3 \pm 24$	676 ± 1040	7575	stable
J160932	$2.4 \times 10^7 \pm 564$	$8.9 \times 10^3 \pm 37$	360 ± 678	4998	stable

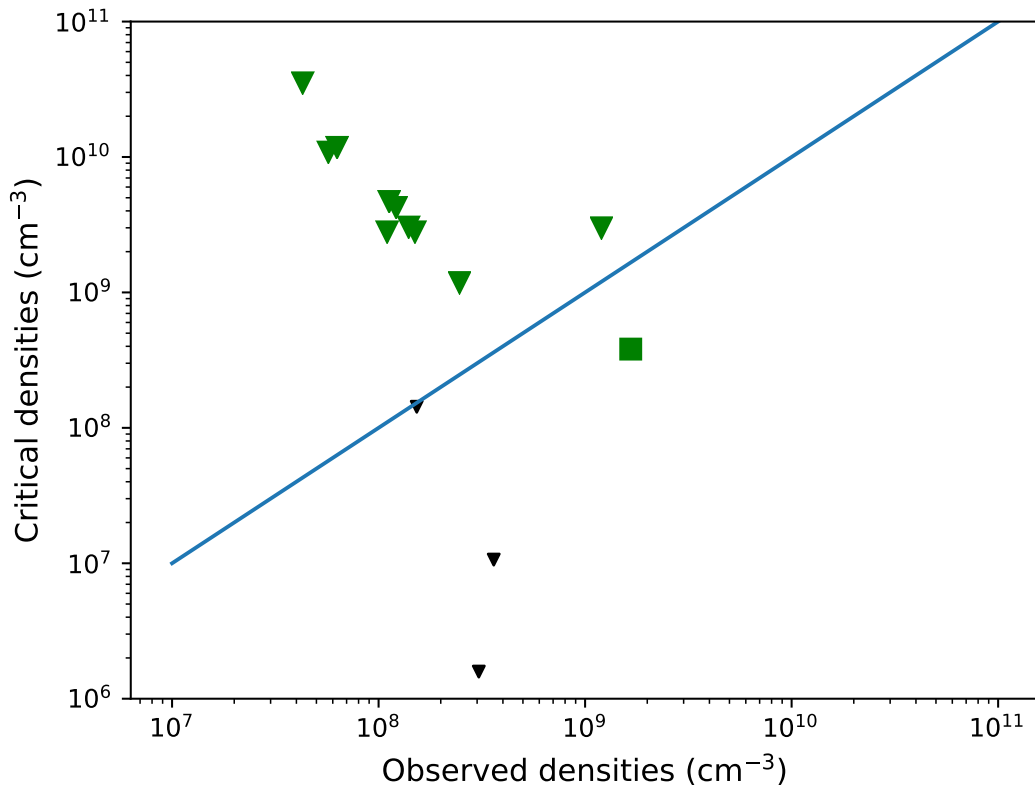


Figure 2.11: Critical densities [cm^{-3}] vs Observed densities [cm^{-3}] at an adopted temperature $T = 9$ K. Green shows the sources studied in this work and the square is the source J154456. Black shows the sources in [Huélamo et al. \(2017\)](#). Triangles represent upper limits. Below the blue line the cores should be unstable, and therefore collapsing.

For the larger scale AzTEC cores we obtain that for the ones that are spatially resolved the observed densities are one to two orders of magnitude smaller than the critical densities regardless the temperature we use (9 or 15 K) and even if we include 1σ uncertainty. Their radius are also larger than the R_{crit} . All of this suggests they are stable, transient cores. The unresolved AzTEC core hosting J154228 could be unstable if its radius is smaller than 534 au.

We did the calculation of the energetic state in the rest of the AzTEC cores where no ALMA detection was obtained, concluding that all the cores in the substellar regime are stable.

In Fig. 2.11 we compare our results with those from [Huélamo et al. \(2017\)](#), by computing the source masses in their work using a temperature of 9 K instead of the 15 K that appear in the original paper. With a temperature of 15 K and the uncertainties related to the mass (factor of 4) it is not completely clear if the cores in Barnard 30 are in collapse. However, using a temperature of 9 K, the pre-substellar core candidates in Barnard 30 clearly lie in the unstable regime. On the other hand, only one of our pre-substellar candidates is in the infalling regime. Our Cycle 3 observations were more sensitive, which might explain our ability to make detections in the non-collapsing regime.

Table 2.11: Estimated masses of the ALMA pre-BD core candidates within an ALMA beam, assuming a r^{-2} density profile from AzTEC

Name	AzTEC (9 K)		ALMA Mass(9 K)		Ratio ¹
	Mass [M_{Jup}]	Radii [au]	Estimated [M_{Jup}]	Observed [M_{Jup}]	
ALMA J153702.653-331924.92	118.85 ± 28.65	5093	1.67 ± 0.40	0.86 ± 0.25	1.94
ALMA J154228.675-334230.18	40.69 ± 9.81	2684	0.75 ± 0.18	5.43 ± 1.12	0.14
ALMA J154456.522-342532.99	49.25 ± 11.87	3803	0.56 ± 0.13	4.78 ± 0.97	0.12
ALMA J154506.515-344326.15	51.40 ± 12.39	3381	1.03 ± 0.25	0.50 ± 0.20	2.06
ALMA J154634.169-343301.90	182.02 ± 43.88	7575	1.64 ± 0.40	1.43 ± 0.33	1.15
ALMA J160932.167-390832.27	97.04 ± 25.64	4998	1.46 ± 0.39	1.21 ± 0.37	1.21

¹ Estimated ALMA mass/ Observed ALMA mass

r^{-2} density profile

Although in the previous section most of the AzTEC pre-substellar cores are stable, the fact that we are detecting very compact and unresolved sources with ALMA guides us to think of another explanation. [Huélamo et al. \(2017\)](#) proposed for the first time that this kind of configurations in substellar objects (stable large scale cores with a compact source inside) could be the “tip of the iceberg” of a larger-scale collapse. Thus, the ALMA compact sources would be formed as a product of gravitational contraction, where an r^{-2} density profile is developed with a finite infall velocity ([Naranjo-Romero et al. 2015](#); [Gómez et al. 2007](#); [Mohammadpour & Stahler 2013](#); [Larson 1969](#)).

Using this r^{-2} density profile and the flux detected with AzTEC we estimate the expected mass inside the ALMA beam with an average value of 0.91 arcsec (~ 139 au). Results can be seen in Table 2.11, where we give the ratio between the estimated and the observed masses. There are four sources that have a ratio close to 1, so the estimated mass from this profile seems to be consistent with the observed one, and hence it seems that this set of pre- or deeply embedded proto-BD candidates are the product of a gravitational collapse. Two sources are not close to ratio 1, and these are the same sources that seem to be unstable using the turbulent fragmentation theory. The difference between the sources with a ratio close to 1 and the other two might be related to their evolutionary stage: the two sources with ratio 0.14 and 0.12 showed a Bonnor-Ebert isothermal profile meaning that they are less evolved, while the other four sources are slightly more evolved and close to begin the formation of a proto-BD.

In Figure 2.12 we compare the mass derived from the ALMA observations (at $T = 9$ K) and the mass estimated from an r^{-2} density profile. The estimated mass error is based on the ALMA mass error and the AzTEC mass error. We include in the plot in red the Barnard 30 pre-BD candidates ([Huélamo et al. 2017](#)) that have a factor 4 of uncertainty in the mass estimation. The results in Barnard 30 are very similar to the ones that we find here where all the cores detected by ALMA without optical/IR counterparts seems to be in gravitational contraction. Thus, both studies reach a very

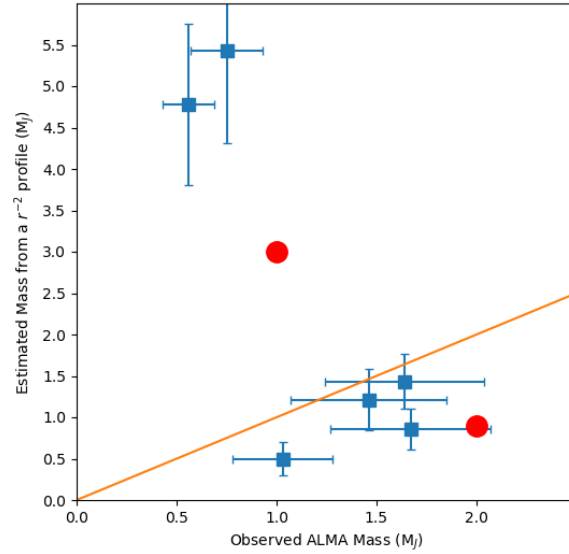


Figure 2.12: Observed mass for the pre-stellar or deeply embedded proto-BD candidates vs a r^{-2} density profile. Using this r^{-2} density profile and the flux detected with AzTEC we estimate the expected mass inside the ALMA beam. Blue points represents the sources in this work detected with ALMA. Red points represents sources from (Huélamo et al. 2017). The ratio between the observed and the estimated masses is close to ~ 1 for all the sources (see Section 2.4.4)

similar conclusion: the objects detected with ALMA seem to be at the beginning of the large scale contraction expected in a scaled-down version of low-mass star formation for BDs.

2.4.5 The nature of J154229.778-334231.86

J154229 is the only proto-BD candidate whose SED is almost complete. To discard the extragalactic nature of J154229 as an Active Galactic Nucleus (AGN), we compared its SED (see right panel in Fig. 2.13) with an average SED of radio loud and radio quiet AGN with different extinction values, following Palau et al. (2012). The differences, especially in the optical and in the millimeter, point out that it is not very probable that J154229 is an AGN. Then, we compared the SED of J154229 with two other proto-BD candidates J1041757 and J1042118 in Taurus (Barrado et al. 2009; Palau et al. 2012) (see left panel in Fig. 2.13). The very similar shapes of all three SEDs shows that J154229 is very likely a proto-BD. One of this sources, J1041757, has a cold dust envelope with a size of 1000 au and a mass of $5M_{\text{Jup}}$, while the envelope of J154229 is three times larger (~ 3500 au) and more massive ($11.36 M_{\text{Jup}}$). This difference may suggest that J15299 is slightly younger than J1042118. We conclude that due to the similarities in the SED, J154229 is a very interesting candidate to be a proto-BD.

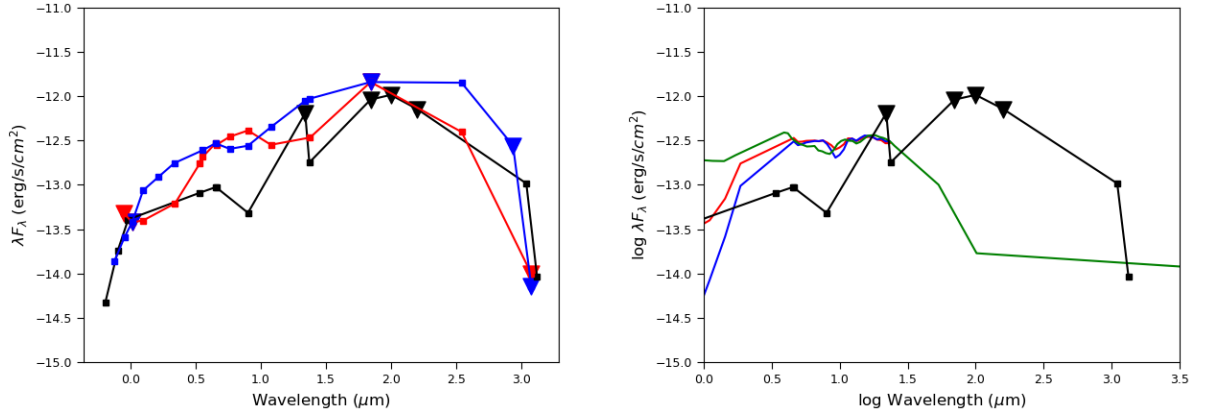


Figure 2.13: Left panel: Spectral Energy Distribution of J154229.778-334231.86(black) compared with other proto-BD candidates J1041757(blue) and J1042118(red). This figure is based on Fig. 8 from Palau et al. (2012). Triangles represent upper limits. Right panel: Spectral Energy Distribution of J154229.778-334231.86(black) compared with average SEDs for radio quiet AGN(red) with an extinction value of 5 in V band, radio quiet AGN(blue) with a extinction value of 10 in V band and radio loud AGN(green) from Shang et al. (2011). This figure is based on Fig. 9 from Palau et al. (2012). Triangles represent upper limits.

2.4.6 Disk masses

The properties of disks of more evolved BDs can also shed light on the formation of substellar objects as well as the possibility of planet formation in these sources. Theoretical predictions (Stamatellos & Herczeg 2015) indicate that, for the same source mass, the disk masses are higher in sources formed by disk fragmentation compared to sources formed as scaled-down version of low mass stars. We aim to compare the properties of the disk masses in different SFRs. Thus, we estimated the dust disk masses of the Class II sources in our sample along with previous Class II BDs observed with ALMA in several SFRs.

The mass of the central object for each source was obtained from the literature. For SONYC-lup3-7 we used the value given in Alcalá et al. (2014), and for the remaining sources values were obtained from Comeron et al. (2009). We calculated the dust disk mass as described in section 2.3.3, but using a value of $\kappa = 0.8519 \text{ cm}^2 \text{ g}^{-1}$ and the distances in Tab. 2.3. The masses we obtained range between 0.42 to $3.42 M_{\oplus}$ (see. Tab 2.12). We calculated upper limits for the Class II sources in Lupus 1 and 3 that were not detected with ALMA. A list of the sources is provided in Table A. We included those objects whose distance is compatible with the average distance derived for Lupus 1 and 3 (see Sect. 2.2.5) as well as BDs in our sample that are not part of Lupus.

Having inferred the disk masses of our Class II substellar sources associated with Lupus, we compared them with BD disks previously observed with ALMA. We searched all the available Class II substellar sources with published ALMA detections, and then we recalculated the masses using the fluxes provided in the literature and the above values of temperature and opacity (Ossenkopf & Henning 1994). The

Table 2.12: Name and disk mass for the spectroscopically confirmed Class II sources in the sample. Temperature is constant at 20K.

Name	Mass [M_{\oplus}]
160658	0.94 ± 0.09
160826	3.42 ± 0.18
Lup706	1.55 ± 0.48
Par-Lup3-4	0.42 ± 0.21
SONYC-lup3-7	0.55 ± 0.09

masses of the central objects were obtained from the literature without incorporating any distance correction. We derived distances (see Tab.2.3) for these sources in other SFRs as $d = 1/\text{parallax}$ from Gaia DR2 (Gaia Collaboration et al. 2018) discarding sources whose relative parallax error exceeds 10 %.

We found sources in several SFRs (ρ Ophiuchus, Upper-Scorpius, Chameleon, Taurus) that need to be discarded because of their distances. From ρ Ophiuchus (Testi et al. 2016a) the sources SONYC-RhoOph-8, ISO-Oph023, ISO-Oph033, ISO-Oph035, CRBR 2322.3-1143, GY92-202, ISO-Oph138 and GY92-264 are discarded because there is no Gaia DR2 parallaxes. ISO-Oph160 was also discarded because the parallax error exceeds 10 %.

From Upper-Scorpius (van der Plas et al. 2016) we chose sources with spectral type later than M6. Then, we discarded J16193976-21453498 because of its distance and usd155601B because we do not have the central mass and luminosity of this BD from the literature.

For Taurus we collected sources from two different works: Ward-Duong et al. (2018) and Ricci et al. (2014). From the latter work we included three BDs, however the error in the flux is not provided in the article so we used 2 times the rms. From Ward-Duong et al. (2018), we selected sources in the substellar regime (spectral type later than M6) (Ward-Duong et al. 2018) choosing the flux obtained with the Natural Weighting algorithm from all the available fluxes. IRAS F04262+2654 was discarded because there is no Gaia DR2 parallax.

From Chameleon (Pascucci et al. 2016) we incorporated disk masses selecting sources with spectral type later than M6 discarding J11062942-7724586 and J11083952-7734166 because there are no Gaia parallaxes. J11095215-7639128 and J11105597-765325 are also discarded because of the distance error.

The disk masses from different SFRs, including Lupus 1 and 3, are shown in Fig. 2.14, which represents an extension of Fig.6 in Testi et al. (2016a). We compared the disk masses and the masses of the central objects. In general, we can say that the Lupus disk masses that we have measured here cover the same mass range as the ones that we are seen in other SFRs. Unfortunately, all the sources from Testi et al. (2016a) with small central mass and small disk mass are not part of the ρ Ophiuchus region or have not been detected by Gaia DR2 and therefore are not included in the plot. It seems that this figure is mainly biased to massive/more luminous disks, as long as we do not included any BD whose distance is not obtained from Gaia.

Additionally, the sources not detected with Gaia are above the detection limit. The observed dispersion may not be related to the age of each region. The ages of Taurus, Lupus and Chameleon are between 1 and 3 Myr (Pascucci et al. 2016), similarly to ρ Oph with an age between 1 to 2 Myr (Alves de Oliveira et al. 2010), while the age of Upper Scopus is between 5 to 10 Myr (Slesnick et al. 2008), and there is no appreciable separation between both age populations, whereas we should expect that as a disk evolves it becomes less massive. Therefore, it is more likely that the dispersion is related to selection effects. Nevertheless, the sample is too small and biased to draw final conclusions about the origin of the detected mass dispersion. Regarding the formation mechanism, we included the predictions from Stamatellos & Herczeg (2015) about disk fragmentation and ejection as black lines in Fig. 2.14. Only $\sim 19\%$ of the sources are in the expected range. The red and blue lines represent the expected scaling relations between disk mass and stellar mass extended from the stellar regime and our measurements seem to be in general agreement with these relations. We conclude, with caution, that disk fragmentation seems not to be the main formation mechanism while the formation of BDs as a scaled-down versions of low-mass stars seems to be plausible.

The largest dust disk mass detected among the objects in our Lupus sample is $3.42 M_{\oplus}$. The minimum mass expected for planet formation is around $10 M_{\oplus}$ (Testi et al. 2016a). Thus, planet formation in the substellar regime seems not to be possible unless planets are already formed. Recent results from studies of protoplanetary disks (Andrews et al. 2018) suggest planets are formed much earlier than previously thought. This can explain the low dust disk masses that we measured if we assume that the planet formation in BDs follows a similar mechanism than planets in the stellar regime.

Finally, a word of caution should be included concerning our tentative conclusion. The relation between temperature and luminosity is still debated (van der Plas et al. 2016; Ward-Duong et al. 2018; Pascucci et al. 2016) given that the models make some assumptions that may or may not be correct. The luminosity, temperature and disk radii are intrinsically related. As it was seen for some sources in ρ Oph (Testi et al. 2016a) the radii can be smaller than expected. This will affect the disk temperature. Therefore, we finally choose a fixed temperature of 20K without any uncertainty. If we use $T=25(L/L_{\odot})^{0.25}$ instead, the disk masses are ~ 3 times larger. Another key point is that the central masses of some of the SFRs might be incorrect due to incorrect distance measurements. In this work we used masses from the literature without applying any mass correction based on the distance obtained from the last Gaia data release.

Future observations with better angular resolution as well as future modelling are required to fully understand the dominant formation mechanism and to decide whether planet formation is possible in these disks.

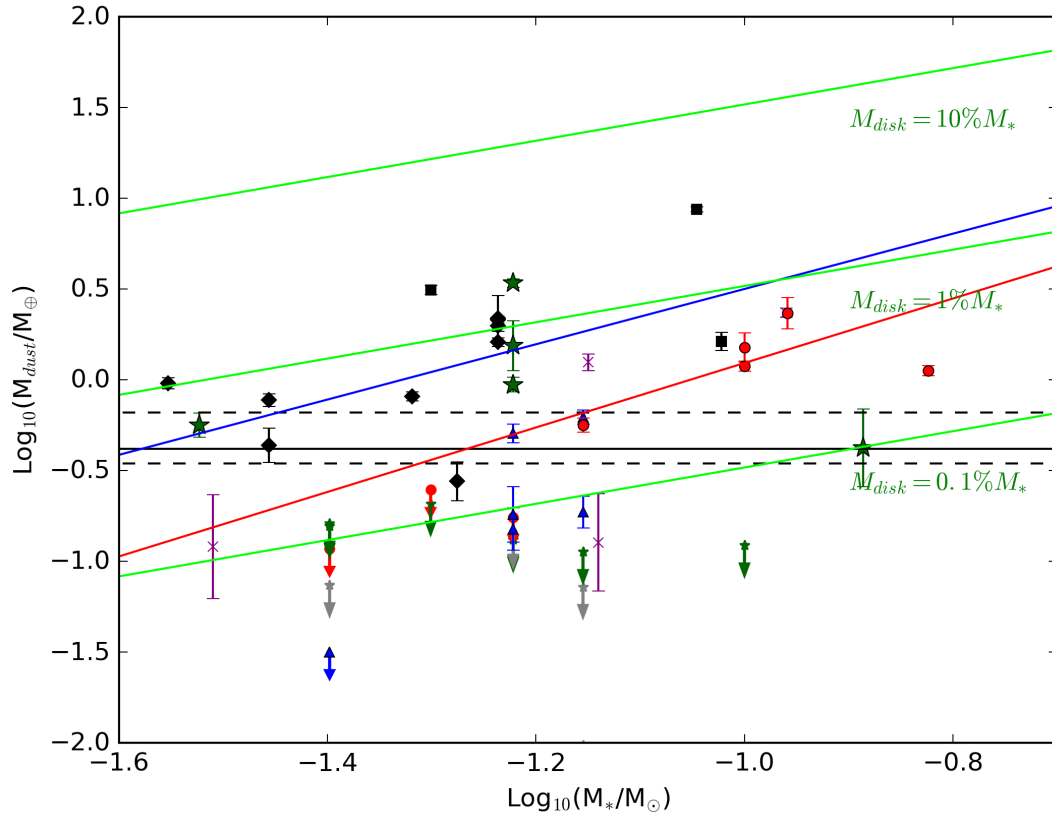


Figure 2.14: Disk masses as a function of the central object Mass (M_*) for the Class II BDs. Green stars are the sources in this paper including upper limits. Grey stars are the upper limits of the sources in our sample that have distance measurements that disagree with the distance to the Lupus clouds. Red circles and red arrows are upper limits for BDs in ρ Oph from Testi et al. (2016a). Blue triangles are for BDs in Upper Scorpius from van der Plas et al. (2016). Black is for the objects in Chameleon I, squares for the BDs in Ricci et al. (2014) and diamonds for the BD in Pascucci et al. (2016). Purple crosses are the BD disks from Ward-Duong et al. (2018) in Taurus. All the objects were observed with ALMA and masses were recalculated using $T=20$ K for consistency. Horizontal black lines are the predictions for disk fragmentation in Stamatellos & Herczeg (2015), while the red and blue lines are the scaling relations between disk mass and stellar mass for protostellar disks given in Andrews et al. (2013)

2.4.7 Is the formation of BDs a scaled-down version of the low mass star formation?

BDs seem to follow a similar formation scheme to low-mass stars and the Lupus sample presented here covered all the evolutionary stages in the substellar object formation.

The compact pre-substellar core candidates that were detected seem to be at the beginning of a large scale collapse. The envelopes, detected with AzTEC, confirm the substellar nature of the candidates. These cores are in gravitational collapse and formed in isolation as it is expected in a scaled-down formation of low-mass stars. Four of the pre-substellar candidates are slightly more evolved. Alternatively, in the most extreme scenario, using the turbulent fragmentation theory, at least one of the candidates is in collapse. The Class II BDs in Lupus, as well as in other SFRs seem to follow the scaling relation between the stellar mass and the disk mass obtained in the stellar regime, and only a small percentage seems to be formed by disk fragmentation. However, the sample is small and still biased to more massive disk. In general terms, it seems that a BD and VLM star formation can be interpreted as a scaled down version of low-mass star formation.

Our detection rate is similar to previous works. Given that our sample was bigger it is natural that we find a larger total number of candidates. We expect that observations with either increased sensitivity or larger angular scale will increase the number of detected sources and help to finally confirm their nature (see Sect. 2.4.2).

As a final remark, although we checked each source in the NASA/IPAC Extragalactic Database to check the classification as possible extragalactic sources, we cannot fully ensure their galactic nature. The sources are mainly located in the cloud filament and are probably associated with the cloud but only future gas detections at the velocity of the cloud will confirm the membership of each source to the complex.

2.5 Conclusions

In this work we present ALMA Band 6 observations (1.3 mm) for a sample of pre- and proto-BD candidates, as well as Class II substellar objects in the Lupus 1 and 3 star forming regions. Target selection was based on sources found in AzTEC (1.1 mm) maps and complemented with Class II BDs from the literature. We supplement our observations with optical/IR archival data. The main objective of this work was to test/constrain BDs formation theories by identifying pre- and proto-BDs and classifying them according to their evolutionary state. The main results are:

- We detected sources in 15 of the 64 ALMA pointings. The total number of compact sources detected is 19. We report masses between 0.33 and 118.14 M_{Jup} . The ALMA detection rate was 23.4 %. The non detection of most of the sources can be related to the source size, with largest spatial scales dominating the emission.

- The number of newly classified candidate objects is 13. We classified 11 sources as pre-BDs or deeply embedded protostar candidates because they do not have optical/infrared counterparts. We classified one Class 0 and one Class I candidate based on their SED.
- We detected continuum emission in 6 more Class II sources previously selected from the literature and we measured the disk mass, which spans values between 0.42 and $3.42 M_{\oplus}$.
- We studied the nature of the eleven sources that we classified as pre-substellar cores or deeply embedded protostar candidates. First, we compared the observed density with the critical density from a Bonnor-Ebert isothermal sphere, obtaining that one of the sources seems to be collapsing. Second, we explored an alternative path comparing the observed mass with the mass that should be obtained from an r^{-2} density profile, and we concluded that all the pre-substellar cores candidates are the result of a gravitational collapse.
- We estimated the final mass of the sources without infrared/optical counterparts assuming a core efficiency of 30 % between the masses derived from AzTEC and ALMA, and find that all the sources remain in the substellar regime.
- The Class 0 candidate (J154229) is at the boundary between Class 0 and I, and due to the SED completeness it is one of the best candidates in the sample. Its SED is similar to that of other Proto-BDs and different from the average SED of AGN.
- We compared disk masses for the objects that we classified as Class II with previous studies in other SFRs, obtaining similar results. Only $\sim 19\%$ of the sources are in agreement with the predictions from disk fragmentation while all the sources follow the trend extended from the stellar regime.

Future observations are needed to confirm the nature of these candidates. Optical/infrared spectroscopic studies for J153914 and J154229 are needed to confirm them as proto-BDs. In addition, the detection of gas associated with any of the candidates in the sample will finally confirm their membership to the Lupus molecular complex.

We conclude that it is highly probable that the dominant mechanism for the formation of these sources is a scaled-down version of low-mass star formation.

Chapter 3

The bipolar molecular outflow of the very low-mass star Par-Lup3-4: Evidence for scaled-down low-mass star formation

Abstract

The formation mechanism of brown dwarfs (BDs) is uncertain and the same applies for Very Low Mass (VLM) stars. One possibility to provide observational constraints on formation theories is through studying the properties of their jets and outflows. However, the number of well studied molecular outflows in very low-mass sources is very small. In this chapter we characterize the bipolar molecular outflow of the very low-mass star Par-Lup3-4 with the aim to provide observational constraints on current theories of the formation of very low-mass stars and brown dwarfs. We detect the dust continuum with ALMA Band 6 and 7 as well as different CO isotopologues (CO (3-2), ^{13}CO (3-2) and CO (2-1)). Our observations reveal the base of a bipolar molecular outflow as well as a secondary compact moving structure perpendicular to the outflow. The outflow mass is $9.54 \times 10^{-7} M_{\odot}$ with an outflow rate of $4.27 \times 10^{-9} M_{\odot}/\text{yr}$. The spectral index between ALMA Band 6 and Band 7 is consistent with grain growth. The secondary moving structure may be an envelope remnant or a secondary outflow with uncertain origin. The properties of the molecular outflow are consistent with the formation of Par-Lup3-4 being a scaled-down version of low-mass star formation.

3.1 Introduction

Very Low Mass (VLM) stars are the bridge between low mass stars and BDs. VLM stars are especially useful to constrain the formation mechanism of BDs.

The properties of VLM sources, that include VLM stars and BDs, are expected to be scaled-down from the low-mass star regime, including the presence of disks (Natta & Testi 2001; Natta et al. 2002), dust grain growth (Apai et al. 2004), magnetospheric accretion (Muzerolle et al. 2003, 2005), or mass-loss (Bourke et al. 2005).

Outflows and jets are ubiquitous structures that accompany forming low-mass stars (Arce et al. 2007b), especially during the Class 0 and I evolutionary phases. As the

material is accreted from the envelope or the protoplanetary disk onto the protostar, a fraction of the material is expelled due to angular momentum conservation. The gas can be ejected in high-velocity collimated jets or in low-velocity disk winds (Hartmann et al. 2016, and references therein).

Low mass star outflows typically have a size between 0.1-1 parsecs, velocities between 10-100 km/s and a maximum outflow mass-loss rate of $10^{-6} M_{\odot}/\text{yr}$ (Bontemps et al. 1996).

In recent years, the presence of jet-like structures and molecular outflows has been reported in several young VLM sources, including Brown Dwarfs (BDs) and VLM stars, mostly based on optical/infrared spectral and astrometric observations. Examples for well-studied low-mass objects with jets are LS-R CrA 1 (Whelan et al. 2009), 2M1207 (Whelan et al. 2012), ISO 143 (Joergens et al. 2012a), ISO-217 (Joergens et al. 2012b), and ISO-Oph 200 (Whelan et al. 2018).

Jets and outflows in VLM sources have also been detected at cm and mm wavelengths. In the cm regime, Morata et al. (2015) discovered the presence of compact free-free emission in four sources. In the (sub)mm regime several VLM sources have been reported to host jets/outflows in different evolutionary phases: the Class 0/I proto-BDs L1014-IRS (Bourke et al. 2005; Huard et al. 2006), and L1148-IRS (Kauffmann et al. 2011); and Class II sources ISO-Oph 102 (Phan-Bao et al. 2008), MHO 5 (Phan-Bao et al. 2011), GM Tau (Phan-Bao et al. 2014). Common and notable characteristics of outflows from these sources include a very small scale (between 600 to 1000 au) and a low outflow velocity (below 5 km/s). Other characteristics, like the ratio between wind mass-loss and accretion rate (Phan-Bao et al. 2014) have been studied to search for trends among VLM sources with evolution, but observational uncertainties are still large.

VLM sources are very faint and difficult to detect, resulting in the few studies of mm-wave molecular outflows that appear in the literature, being limited by sensitivity. Phan-Bao et al. (2014) detected only three out of eight VLM outflows surveyed. Moreover, there are no sufficient studies (to our knowledge) on the details at the base of the outflow near the driving source; nor have the inner cavity walls near the launch region been seen in great detail.

ALMA's high sensitivity and high spatial resolution capabilities can provide unprecedented details of mass-loss phenomena in VLM sources.

In this work, we present ALMA observations to characterize the outflow of Par-Lup3-4, a VLM object located in the Lupus 3 molecular cloud. We detect the source in Band 6 and 7 continuum and three gas emission lines, i.e. CO(2-1), CO(3-2) and ^{13}CO (3-2). These observations reveal details of the outflow structure surrounding Par-Lup3-4, which are consistent with the outflow of Par-Lup3-4 being a scaled-down version of outflows associated with the formation of more massive stars.

3.2 Previous observations of Par-Lup3-4

Par-Lup3-4, located in the Lupus 3 molecular cloud, is a VLM star with a mass of $0.12 M_{\odot}$ and spectral type M5 (Comerón et al. 2003). The source appears underluminous when compared to similar sources in the same star-forming region, and this is likely due to its edge-on disk orientation.

Stellar parameters of Par-lup3-4 were estimated using VLT/X-Shooter, including a temperature of 3197 K and a luminosity of $0.003 L_{\odot}$ (Natta et al. 2014, assuming a distance of 200 pc) as well as a mass accretion rate of $\log \dot{M}_{\text{acc}} = -9.1 \pm 0.4 M_{\odot}/\text{yr}$ and a mass-loss rate of $3.2 \times 10^{-10} M_{\odot}/\text{yr}$ (Bacciotti et al. 2011).

A jet from this source was first detected by Fernández & Comerón (2005). A bright knot at $1''.3$ was detected in H α and [S II]. Assuming a jet velocity of 150 km/s, the disk tilt should be 8° or 12° with a velocity of 100 km s^{-1} with respect to the plane of the sky. The small jet inclination implies a high disk inclination, assuming that they are perpendicular. A Herbig Haro (HH) object, HH 600, is associated with the jet. In Comerón & Fernández (2011) the jet is studied with FORS2 in a very similar fashion to Fernández & Comerón (2005). The knot that was at $1''.3$ moved to $2''.55$ in 7.2 years; it was not detected in H α in the second epoch, and it was fainter in [S II] by around 30%. Comparing with previous observations, the radial velocity of the jet is $168 \pm 30 \text{ km/s}$ in the plane of the sky, giving a jet inclination of $6^{\circ}7 \pm 1^{\circ}4$. A detailed study of the optical jet can be found in Whelan et al. (2014), who show a very low velocity of $\pm 20 \text{ km/s}$ that extends to $\pm 3''$, in agreement with the kinematics derived in the previous studies. They also obtained a better estimation of the ratio $\dot{M}_{\text{out}}/\dot{M}_{\text{acc}} = 0.05^{+0.10}_{-0.02}$, which supports theoretical predictions of jet launch (Ferreira 2013; Frank et al. 2014).

The disk around Par-Lup3-4 was studied in detail by Huélamo et al. (2010) through the analysis of its Spectral Energy Distribution (SED) together with high-angular resolution adaptive optics (AO) assisted observations in the infrared. The SED was built with data covering the spectral range from the optical to the sub-mm regime, and displayed a double peak emission typical of Class II edge-on disks and Class I sources.

The early classification as Class I was discarded due to high angular-resolution infrared observations, which revealed no thick envelope around Par-Lup3-4. The SED was modeled using Monte Carlo simulations. Several parameters were obtained, the most important one being an disk inclination of 81° , compatible with the value obtained by (Fernández & Comerón 2005). The maximum derived grain size is $>10 \mu\text{m}$ which may be indicative of dust processing.

Recently, Ansdell et al. (2016) and Ansdell et al. (2018) reported the detection of dust continuum emission from Par-Lup3-4 with ALMA, neither the gas disk nor the bipolar molecular outflow cavity was detected.

We adopt a distance of 155.22 pc, which we derived using a Bayesian analysis from Gaia Data Release 2 (Gaia Collaboration et al. 2018) (see Chapter 2).

Table 3.1: Dust properties of the ALMA detection

Name	Robust	rms [mJy/beam]	Flux	Peak	Gauss flux	Gauss peak	Beam Size		
			density [mJy]	intensity [mJy/beam]	density [mJy]	intensity [mJy/beam]	Major axis [arcsec]	Minor axis [arcsec]	PA [$^{\circ}$]
Band 6	2	0.051	0.31	0.31	(0.41 \pm 0.07)	0.28	0.93	0.84	84.26
Band 7	1.5	0.017	0.59	0.59	(0.57 \pm 0.02)	0.60	0.41	0.36	86.92

3.3 Observations

3.3.1 ALMA observations

The work presented in this chapter is mainly based on observations of Par-Lup3-4 performed with ALMA during Cycles 3 and 5¹, in Bands 6 and 7, respectively.

The ALMA Band 6 observations were part of a continuum survey that aimed at studying the formation mechanisms and evolution of BDs. These observations comprised more than 60 substellar object candidates covering different stages of evolution, from the pre-stellar core phase to Class II objects (a full description of the observations and the sample was presented in Chapter 2). Par-Lup-3-4 was included in the list of objects to study and we present here the continuum emission and CO(2-1) gas emission associated with this source.

ALMA Band 7 observations were performed in Cycle 5 on the 24th of March 2018, as part of the ALMA program 2017.1.01401.S. Two individual executions were obtained to achieve the requested rms. The allocated time for the program was 1.77 hours including overheads, with a time on source of \sim 140 min. Data were taken using 45 antennas with maximum and minimum baselines of 15 and 783 respectively, which provided an angular resolution of \sim 0.25 arcsec and a largest angular scale of 7.29 arcsec. The weather conditions were excellent during these observations, with a PWV \sim 0.60 mm. The FoV was 16 arcsec. We observed a single field in dual polarization mode, dedicating one spectral window of 0.469 GHz bandwidth to observe CO(3-2) with a velocity resolution of 0.11 km/s. The other three spectral windows were selected to study continuum emission with a bandwidth of 1.875 GHz. These three spectral windows covered transitions of ¹³CO(3-2), CS(7-6), and SO₂(4(3,1)-3(2,2)) for serendipitous detection of gas tracers with a velocity resolution of 0.44 km/s, as well as centering at strategical frequencies to get the best atmospheric transmission. Bandpass and flux calibrations were done using the QSO J1517-2422, while the QSO J1610-3958 was used as the phase calibrator.

Data were processed using The Common Astronomy Software Applications package (CASA). We used the pipeline version 4.5.3 for the Cycle 3 observations, and version 5.3.0 for Cycle 5 observations. The task CLEAN was used to produce continuum and spectral line images. We used Briggs weighting with different robust parameters in

¹This chapter makes use of the following ALMA data: ADS/JAO.ALMA#2015.1.00512.S and ADS/JAO.ALMA#2017.1.01401.S. ALMA is a partnership of ESO (representing its member states), NSF (USA) and NINS (Japan), together with NRC (Canada), MOST and ASIAA (Taiwan), and KASI (Republic of Korea), in cooperation with the Republic of Chile. The Joint ALMA Observatory is operated by ESO, AUI/NRAO and NAOJ.

order to obtain the best compromise between resolution and signal-to-noise-ratio, varying from 0.5 for CO gas emission lines to 2 for the ^{13}CO (see table 3.1 for more details). Primary beam correction was applied before inferring physical parameters from any of the images.

3.4 Results

3.4.1 Continuum emission

ALMA continuum emission images in Band 6 at 1.3 mm and Band 7 at 0.89 mm were generated considering all spectral channels from all spectral windows, but excluding those channels with spectral line emission. The gas emission lines identified were CO ($v=0$ 2-1) in Band 6 and CO ($v=0$ 3-2) and $^{13}\text{CO}(3-2)$ in Band 7. Details of the continuum emission properties are included in Table 3.1.

We detect dust continuum emission at 1.3 mm (225.27 GHz) at the position R.A.= 16h08m51.426s, Dec=-39°05'30.82". The ALMA Band 6 continuum image with best sensitivity was obtained using natural weighting (Robust value = 2). Par-Lup-3-4 was detected at a 6σ level with a flux density of 0.30 ± 0.06 mJy, including a flux calibration error of 10 %. The synthesized beam size is $0.93 \times 0.84''$, and the source is spatially unresolved. Our results are compatible with previous existing observations reported by Ansdell et al. (2018), who measured a flux of 0.35 ± 0.11 mJy.

Dust continuum emission at 0.89 mm (338.15 GHz) is clearly detected at more than 50σ (see right panel Fig.3.1) at the (J2000) position R.A.= 16:08:51.424, Dec=-39:05:30.91. The best quality image (prioritizing signal-to-noise while optimizing angular resolution to resolve the spatial structure) was obtained using a robust parameter value of 1.5, yielding an unresolved source with a flux density of 0.59 ± 0.06 mJy, including a flux calibration error of 10 %. Ansdell et al. (2016) showed the first ALMA continuum image of this source in Band 7, where dust properties were constrained with a flux density of 0.91 ± 0.26 mJy. Our results are compatible with theirs within 1σ uncertainty. In an attempt to improve the spatial resolution, we generated an image using uniform weighting, but still did not resolve the source, and therefore we adopt the value of the synthesized beam (~ 0.24 arcsec) of the image with uniform weighting as an upper limit of the dust disk size (59.8 au diameter at 155.22 pc).

Assuming the ALMA continuum emission comes from thermal dust, and considering optically thin emission, and a dust-to-gas ratio of 100, the total dust and gas mass can be derived from Hildebrand (1983) as:

$$M = \frac{S_\lambda D^2}{B_\lambda(T_d) \kappa_\lambda}. \quad (3.1)$$

Where S_λ is the flux density from Tab. 3.1, D is the distance to the sources (155.2 pc), and $B_\lambda(T_d)$ is the Planck function at a temperature of 20 K for a Class II source (Pascucci et al. 2016). κ_λ is the absorption coefficient obtained from Ossenkopf & Henning (1994), Table 1, column for thin ice mantles and density of 10^6 cm^{-3} .

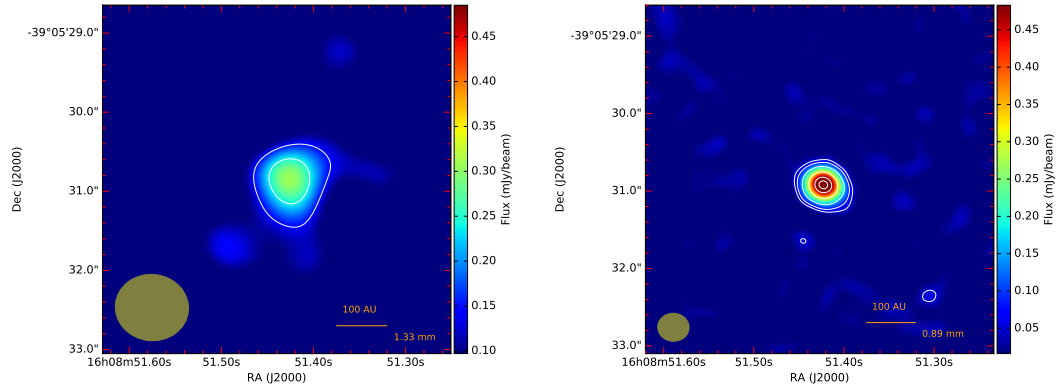


Figure 3.1: Left panel: 1.3 mm ALMA continuum image using natural weighting. The white scale contour is 3, 5 σ , where σ is the rms noise level of the map (4.85×10^{-5} Jy/beam). Right panel: 0.89 mm ALMA continuum image using a robust value of 1.5. The white scale contour is 3, 5, 10, 20, 30, 35 σ , where σ is the rms noise level of the map 1.61×10^{-5} Jy/beam). Beam size is represented by the yellow ellipse in the bottom left corner in both panels.

Table 3.2: Gas properties of the ALMA detection

Molecular transition	Robust	rms [Jy/beam km/s]	Integrated intensity [Jy km/s]	Peak intensity [Jy/beam]	Beam Size		
					Major axis [arcsec]	Minor axis [arcsec]	PA [$^{\circ}$]
CO(3-2)	1	1.57×10^{-2}	3.79	0.99	0.38	0.35	80.56
CO(2-1)	1	3.12×10^{-2}	1.97	0.89	0.79	0.71	82.61
$^{13}\text{CO}(3-2)$	2	4.07×10^{-3}	8.16×10^{-2}	5.50×10^{-2}	0.41	0.37	87.68

We interpolate for the wavelength of 1.3 mm and for 0.89 mm obtaining values of $\kappa = 8.519 \times 10^{-3} \text{ cm}^2 \text{ g}^{-1}$ and $1.813 \times 10^{-2} \text{ cm}^2 \text{ g}^{-1}$, respectively. The derived mass for the gas and dust are $0.19 \pm 0.05 M_{\text{Jup}}$ for Band 6 and $0.27 \pm 0.06 M_{\text{Jup}}$ for Band 7. Using the fluxes from [Ansdell et al. \(2016\)](#) and [Ansdell et al. \(2018\)](#) with a distance of 155.2 pc instead of their assumed 200 pc, and the opacity law from [Ossenkopf & Henning \(1994\)](#), our results are compatible with theirs.

3.4.2 Gas emission lines

We detected for first time with ALMA three different gas emission lines towards this source. The results for the CO(2-1), CO(3-2) and ^{13}CO (3-2) are summarized in Table 3.2.

CO(2-1)

The first molecular gas emission detection (bottom panel in Fig. 3.2) surrounding Par-Lup3-4 was at the frequency of CO (2-1) as part of our ALMA Band 6 Lupus 1 and 3 dataset. The CO(2-1) emission spans a total velocity of ~ 13 km/s, in velocity channels ranging from -3.2 to 10.0 km/s (see Fig 3.3).

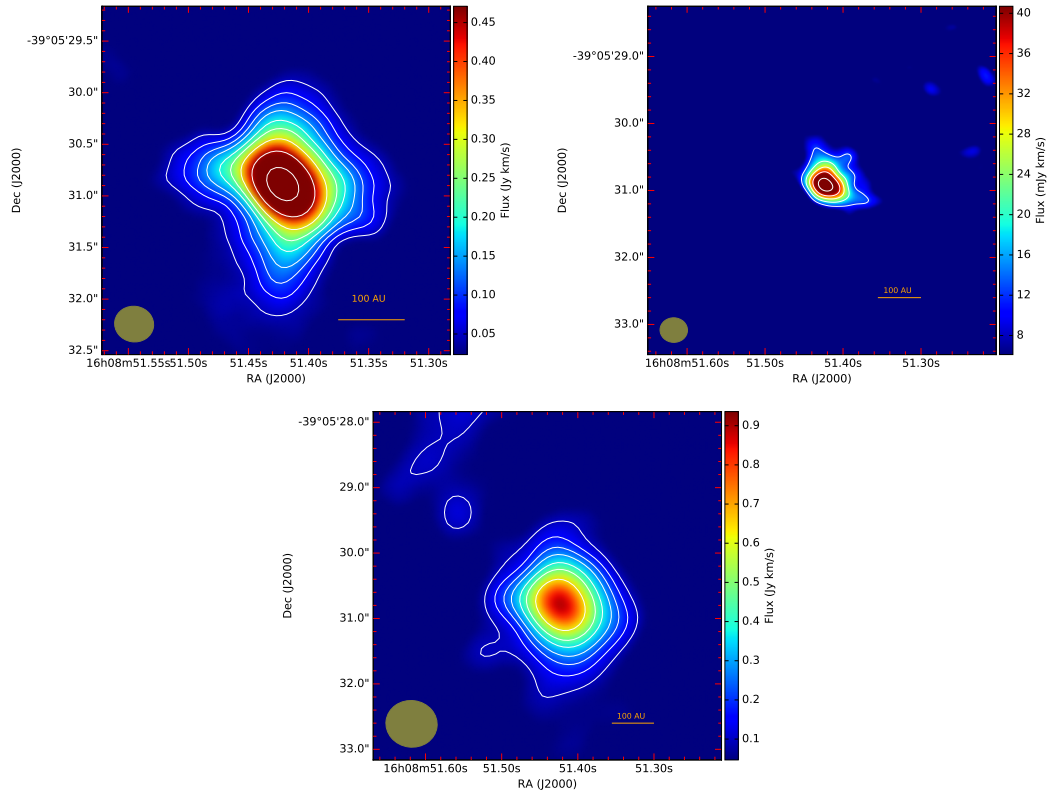


Figure 3.2: Top left panel: CO ($v=0$ 3-2) flux integrated ALMA map from velocity -3 to 11 km/s with a robust value of 1. The white contours are 3, 5, 7, 9, 12, 15, 20, 30 and 50 times the rms (1.57×10^{-2} Jy/beam). Top right panel: ¹³CO flux integrated ALMA map from velocity -0.08 to 7.44 km/s. The white contours are 3, 5, 7, 9 and 12 times the rms ($\times 10^{-3}$ Jy/beam). Bottom panel: CO(2-1) flux integrated ALMA map from velocity -2.62 to 10.08 km/s. The white contours are 3, 5, 7, 9, 12, 15 and 20 times the rms (3.12×10^{-2} Jy/beam). Beam size is represented by a yellow ellipse in the bottom left corner of the three panels.

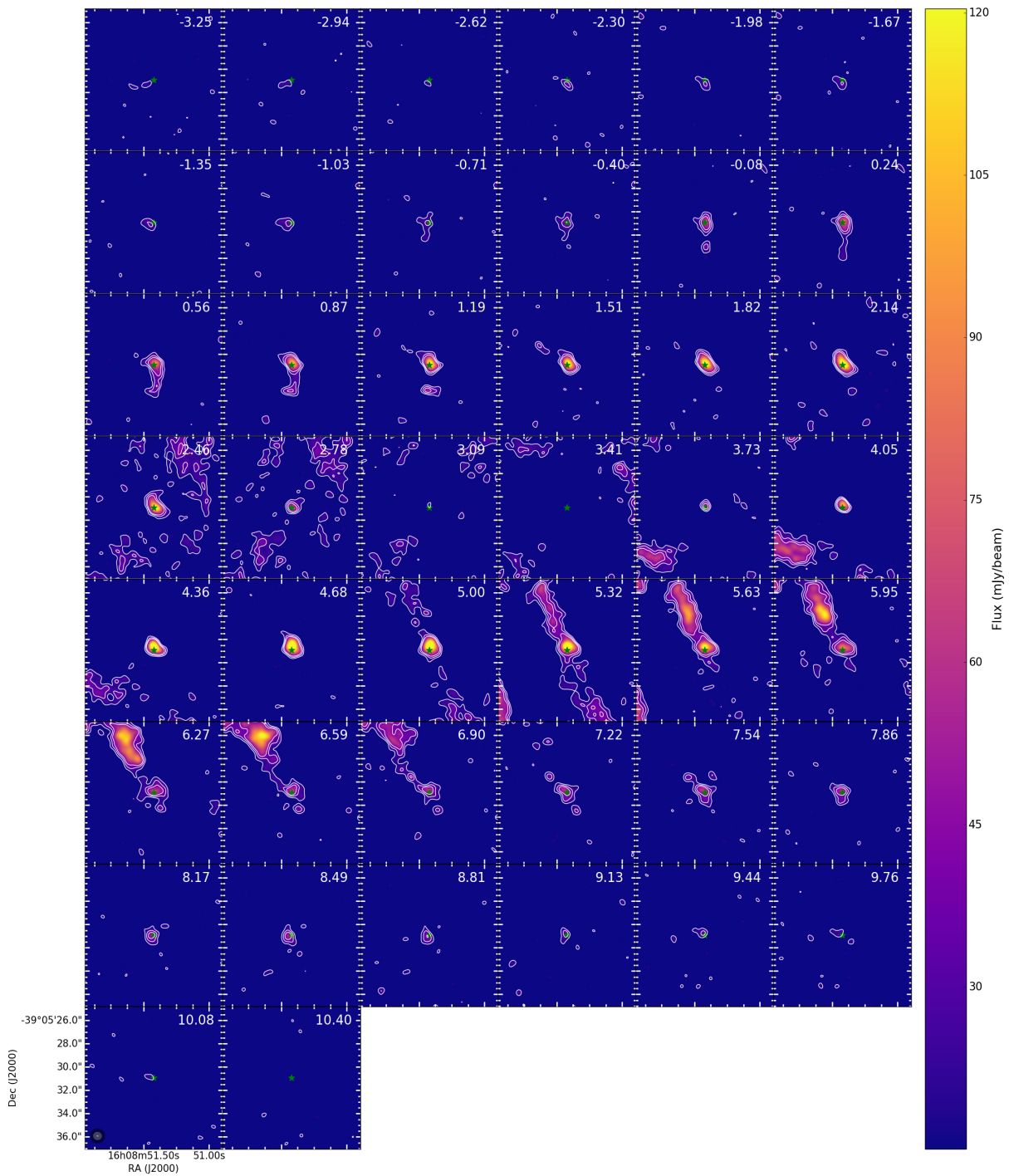


Figure 3.3: CO (2-1) channel emission maps towards Par-Lup3-4. Contour levels are 3, 5, 7 times the rms (6.02×10^{-3} Jy/beam). The green star marks the position of the peak intensity of the continuum image. These maps have been obtained using a robust parameter equal to 1.

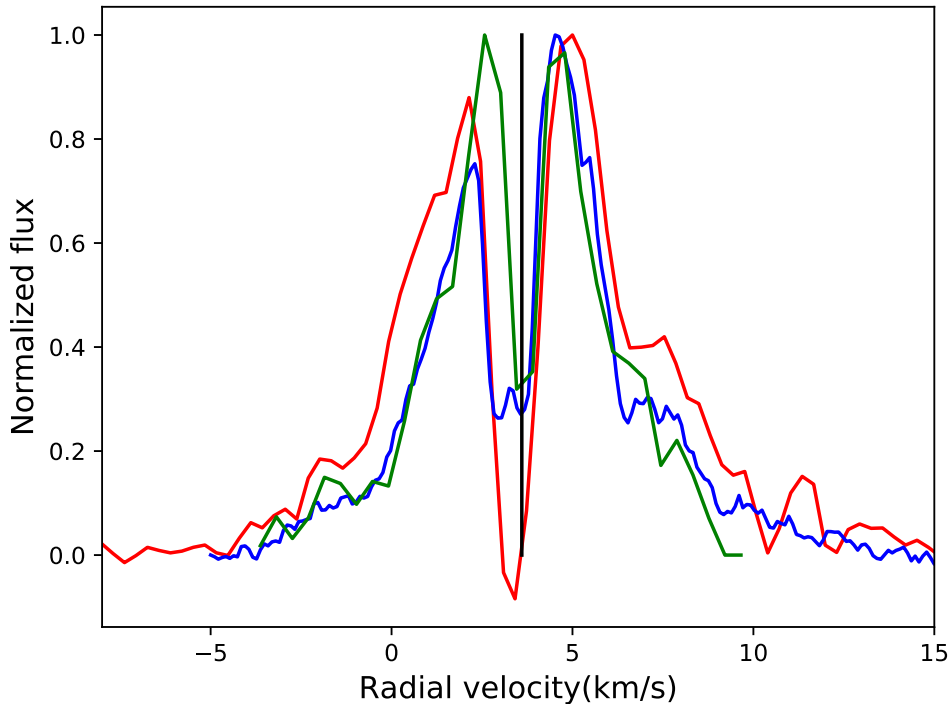


Figure 3.4: ^{13}CO (green), CO(2-1) (red) and CO(3-2) (blue) spectra averaged over the 5σ contour level in the integrated flux maps for each line applied to the spectral cube and centered on Par-Lup3-4. Black line represent the local standard velocity obtained from the ^{13}CO .

Par-Lup3-4 is a compact source extending less than 3 arcsec. ($< 3''$). Its spectrum displays a double peak profile with blueshifted and redshifted wings and a self-absorption feature at ~ 3.4 km/s (see Fig. 3.4), probably due to the cold foreground parental molecular cloud. The self-absorption feature is close to the systemic velocity (3.46 to 3.90 km/s, see Sect. 3.4.2). Blueshifted emission spans velocities between -3.2 to 2.8 km/s with two spatial components that show an arc-like structure in the South-west direction (from -3.2 to 1.5 km/s) and in the North-east (from 1.8 to 2.5 km/s). Redshifted emission (velocities between 3.7 to 10 km/s) shows a similar trend, tracing an arc-like shape in the North-east direction between ~ 4 to 6.6 km/s and in the South-west direction between 7.0 to 10 km/s. These blue and redshifted structures suggest for the first time the presence of a compact low-velocity bipolar molecular outflow near the plane of the sky powered by Par-Lup3-4, with the Southern lobe showing higher velocities with respect to the systemic velocity than the Northern lobe. Extended emission and negative features due to the effects of filtering large scale structures by the interferometer are present near 2.7, 4, and 5 km/s. In particular, a shell-like clumpy distribution is seen in velocity channels from 3.4 to 4.3 km/s, and this could be a remnant of the envelope in which the source was originally embedded.

There is an elongated and clumpy structure North-east of Par-Lup3-4 with a size of $\sim 5''$ and a velocity gradient from 5.6 to 7.2 km/s, whose origin is unknown (see Fig 3.5). This structure seems to originate close to the position of Par-Lup3-4, with

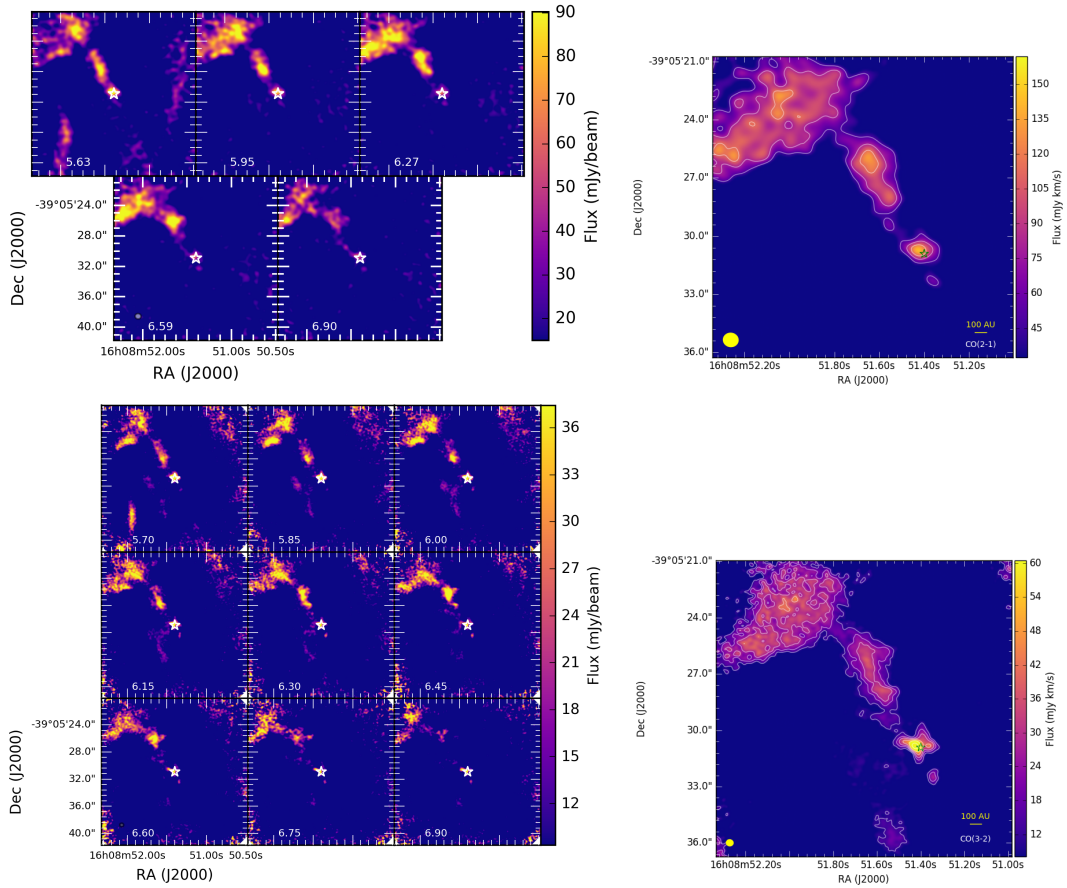


Figure 3.5: Left top panel: CO ($v=0$ 2-1) ALMA channel maps towards Par-Lup3-4 and the secondary possible outflow following the direction North-east, all the maps share the same linear color scale with a robust value of 1. Right top panel: ALMA integrated emission of CO ($v=0$ 2-1) from a velocity of 5.63 to 6.90 km/s. Contours shows 3, 5, 7 times the rms (6.02×10^{-3} Jy/beam). Left bottom panel: Similar to Left top panel but with CO(3-2), all the maps share the same linear color scale with a robust value of 1. Right top panel: ALMA flux integrated flux of CO ($v=0$ 3-2) from a velocity of 5.70 to 6.90 km/s. Contours shows 3, 5, 7 times the rms (4.03×10^{-3} Jy/beam). The white or green star shows the peak intensity in the continuum source position for all the images.

a velocity that increases with distance. It collides in the North with a more extended clump, which may be part of the surrounding parental molecular cloud. We will discuss the possible nature of this feature in the next section.

CO(3-2)

The CO(3-2) (top left panel in Fig. 3.2) emits in a velocity interval between -2.92 to 11.6 km/s and it shows similar spatial and spectral characteristics as CO(2-1). Its spectrum has a double peak profile, with a more intense red wing and a self-absorption feature between 2.3 to 4.5 km/s (see Fig. 3.4). The CO (2-1) emission detailed in the previous sub-section suggests the existence of a compact bipolar outflow, which is confirmed by the CO(3-2) emission line detected in our Band 7 data

(see Fig. 3.6). The CO(3-2) traces low velocity outflowing material with an inclination near the plane of the sky, as revealed by the different arc-like quasi-symmetric structures with superimposed blue- and red-shifted emission that trace the base of a compact bipolar outflow very close to the position of Par-Lup3-4. This outflow has the same orientation as the jet and the counterjet detected by [Fernández & Comerón \(2005\)](#). The CO(3-2) lobe structures clearly delineate the South-west and the North-east side of the outflow cavities that result from the interaction between the ejected material with the surrounding envelope.

CO(3-2) blue-shifted emission spans velocities between -2.92 to 2.80 km/s and the red-shifted emission is between 3.68 to 10.72 km. The blue-shifted arc-like structures are seen from -2.92 to 2.36 km/s in the South-west and from 0.60 to 2.80 km/s to the North-east. The red-shifted emission comes from a North-east arc-like structure that emits between 3.68 to 6.32 km/s, and a South-west one that extends from 5.00 to 10.72 km/s.

Cloud emission is seen as an inhomogeneous distribution of material spread randomly in the whole map at certain velocities. Cloud emission can be seen between 2.51 km/s to 4.41 km/s and between 5.26 km/s and 5.58 km/s, beyond 5.90 km/s and below 7.20 km/s we can not distinguish clearly between cloud emission and outflow emission.

The Northern stream of clumpy material observed in CO (2-1) at velocities between 5.6 to 7.2 km/s is also detected in the CO (3-2) transition, with similar characteristics in terms of speed and location (see Fig. 3.7 and Fig. 3.7). The nature of this structure will be discussed in Sect.3.5.2.

¹³CO (3-2)

¹³CO (3-2) emission is detected very close to Par-Lup3-4 in a velocity range of 0.96 - 7.12 km/s (see Fig. 3.8). ¹³CO (3-2) traces a more compact and denser structure than the one observed with the CO isotope, where the presence of the North-eastern outflow cavity is still well perceived (top right panel in Fig. 3.2).

Given the optically thin nature of the ¹³CO line, its spectrum is less affected by possible emission of the surrounding cloud and we use it to infer a more accurate value of the systemic velocity of the source, which we found between 3.46 to 3.90 km/s (see left panel Fig. 3.9). The velocity map of the most intense and compact gas close to Par-Lup3-4 suggests a rotation pattern with redshifted material in the North-east and blueshifted material in the South-west, in a flattened structure perpendicular to the direction of the molecular outflow well detected in the other CO transitions. The spatial and spectral resolution as well as the sensitivity of our data do not allow to confirm a Keplerian nature of this rotation. Future ALMA observations will be needed to confirm and study properly this structure.

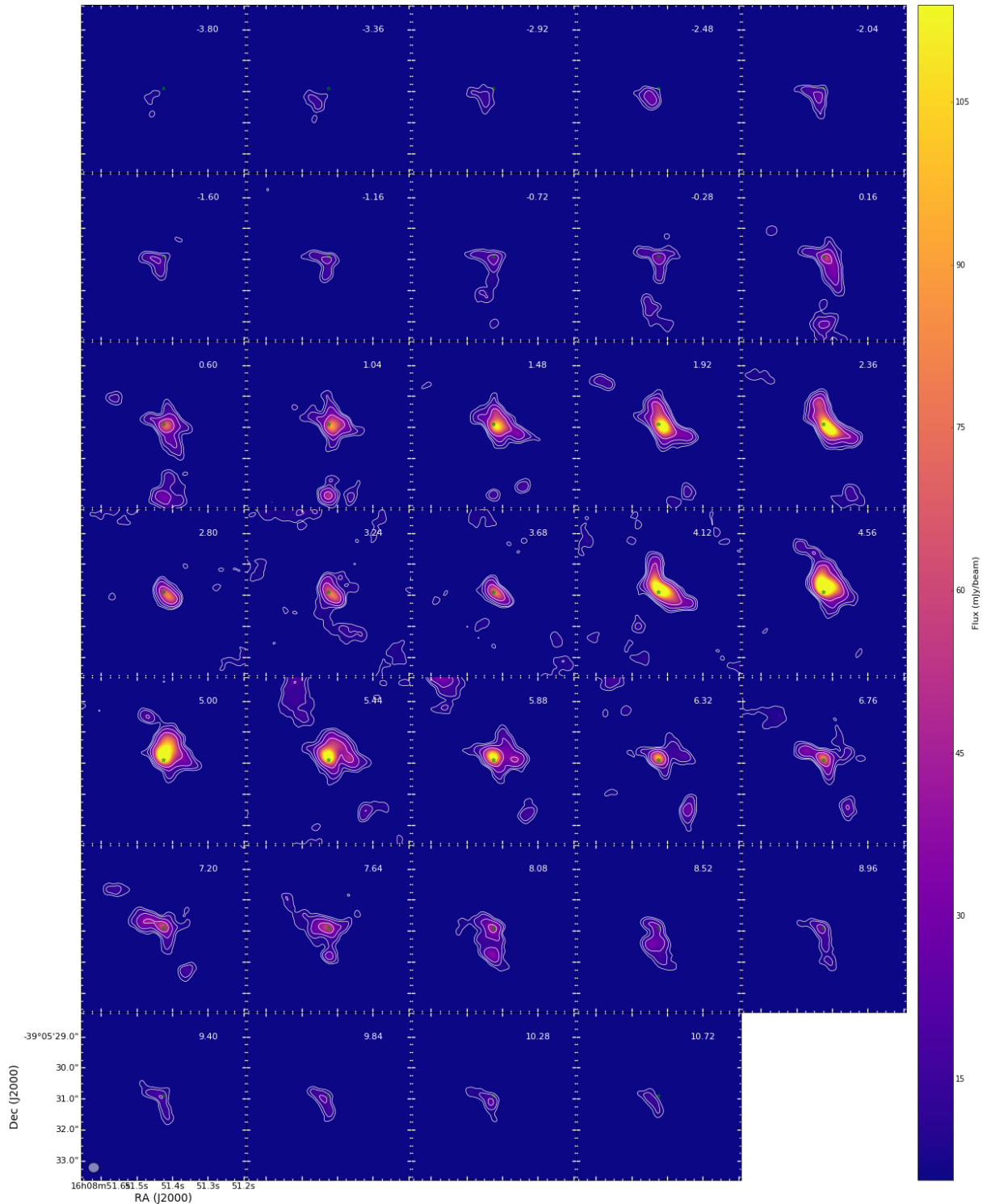


Figure 3.6: CO ($v=0$ 3-2) channel maps towards Par-Lup3-4 using robust value of 1. We used a uv taper >50 $k\lambda$. We binned the image to a velocity resolution of 0.44 km/s. The velocity of the channels is shown in the LSR frame, centered at the frequency of CO (3-2). All maps share the same linear color scale. White contour levels are 3, 5, 9, 17 σ . σ is the rms noise level of the map (2.28×10^{-3} Jy/beam). The green star marks the position of the peak intensity in the continuum image.

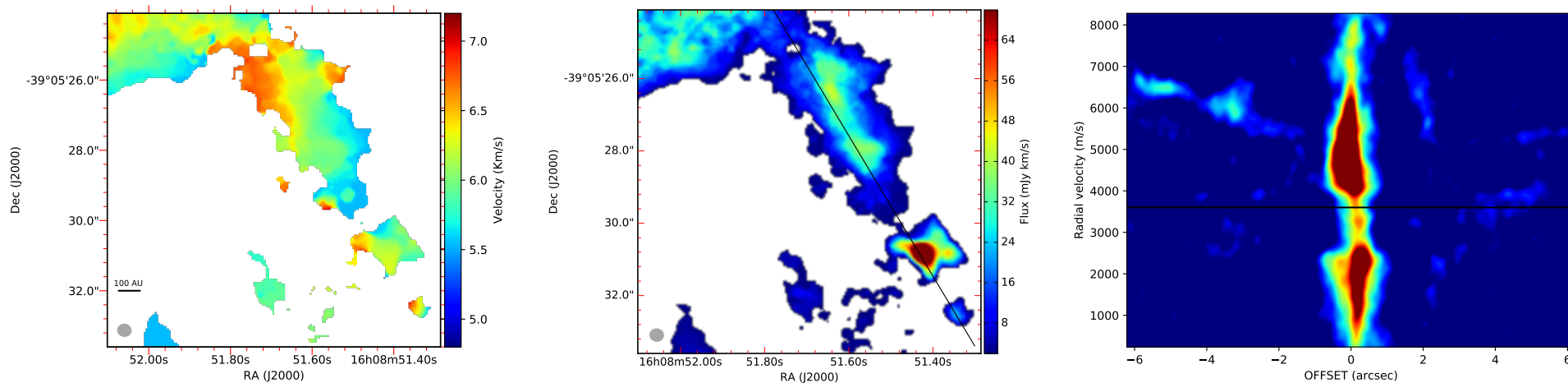


Figure 3.7: Left panel: CO ($v=0$ 3-2) ALMA velocity map. Middle panel: CO ($v=0$ 3-2) ALMA flux integrated map with threshold above 5σ , black line mark the position where the position diagram map on the right panel was located. Right panel: Position-velocity diagram for the CO ($v=0$ 3-2) assuming a PA of 30.48 deg and a width of ~ 1.2 arcsec. The horizontal black lines shows the LSR. In the three images the beam size is represented by the grey ellipse in the bottom left corner. Only pixel values above 5σ are included.

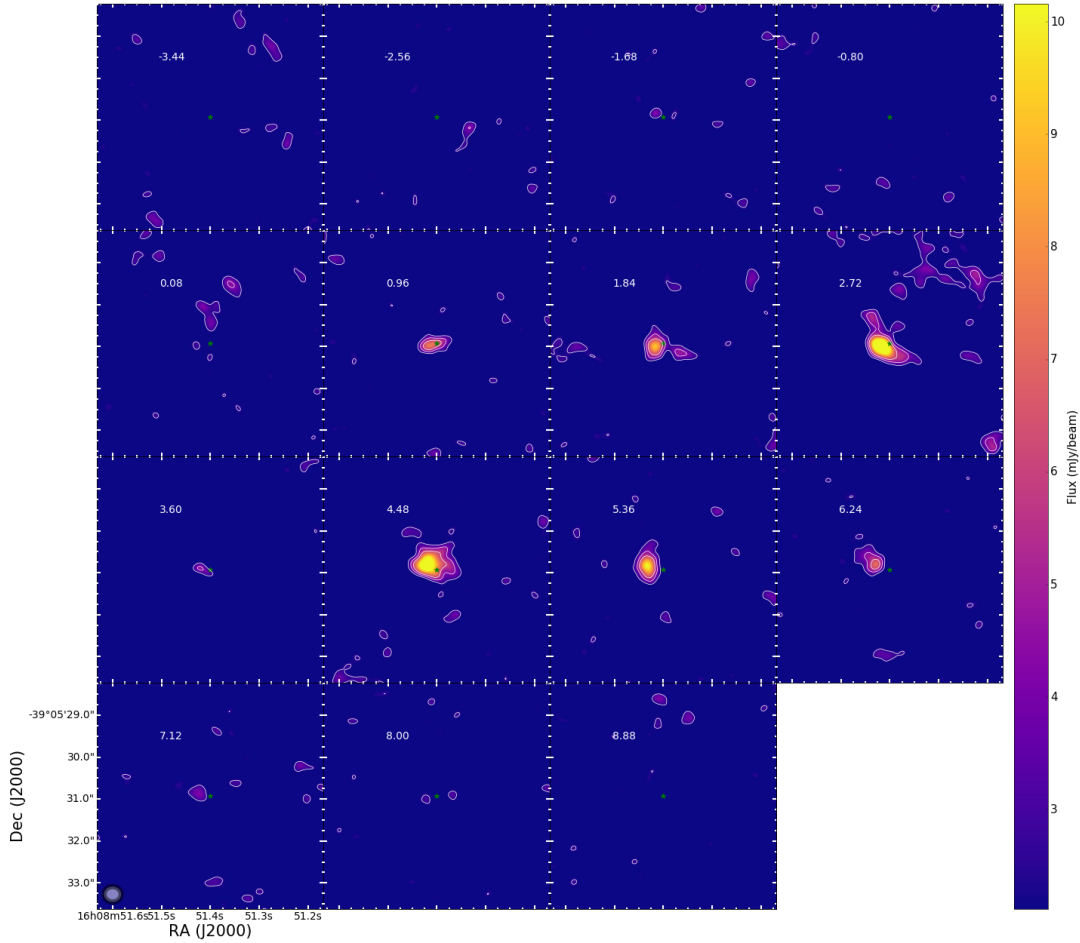


Figure 3.8: ^{13}CO channel maps towards Par-Lup3-4 using robust value of 2. The velocity of the channels is shown in the LSR frame, centered at the frequency of ^{13}CO . Channels are binned to 0.88 km/s. All maps share the same linear color scale. White contour levels are 3, 5, 7 times the rms (8.47×10^{-4}). The black star represents the position of the peak intensity in the continuum image.

3.4.3 Outflow geometrical and dynamical properties

We derive the geometrical and dynamical outflow properties of Par-Lup3-4 in an attempt to contribute to the characterization of the properties of outflows surrounding VLMs. We admit that the values and conclusions drawn from our observations must be considered with some caution as the entire outflow structure is not detected and molecular cloud contamination affects several emission channels.

The geometrical properties we calculated are the opening angle, the average length, and the position angle of the outflow, which were measured by hand for both lobes. Our ALMA observations show (see section 3.4.2) that we are witnessing the base of the molecular outflow, but neither the ellipsoidal full lobe nor the shockwave front are detected. Therefore, we can only obtain a lower limit for the average lobe length. The average length was measured using the CASA VIEWER ruler and the 3σ contour of the CO(3-2) flux integrated map (Fig. 3.10), obtaining values of 2.50 arcsec for the

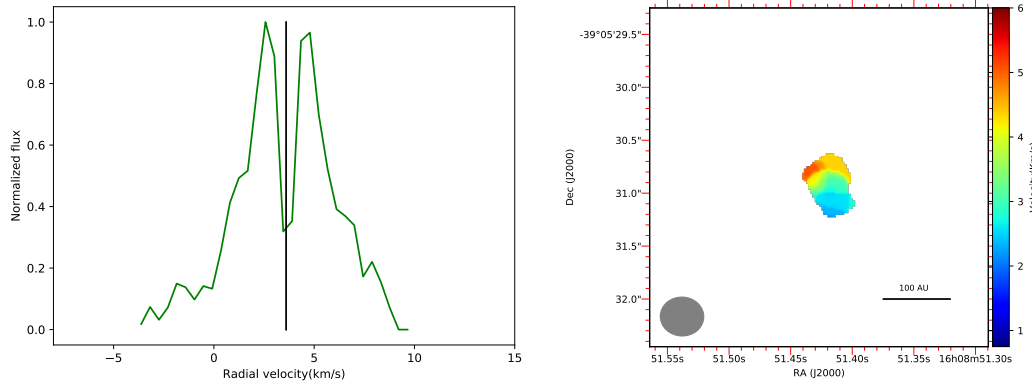


Figure 3.9: Left panel: ^{13}CO spectral profile of the right panel image. Right panel: Velocity map of the ^{13}CO emission line with a threshold of seven times the rms (4.07×10^{-3} Jy/beam). Beam size is represented by the grey ellipse in the bottom left corner.

South-west lobe and 1.14 arcsec for the North-east lobe. The average size value is 1.8 arcsec. The opening angle was calculated in the aforementioned map, providing an angle of 108° for the Southern lobe and 116° for the Northern lobe. Additionally, we measured a position angle of 116° and 307° for the Southern and Northern lobes respectively.

The dynamical properties that we study comprises the outflow mass (M_{outflow}), dynamical time (τ_{dyn}), momentum (P_{outflow}), kinetic energy (E_{outflow}), luminosity (L_{outflow}) and force (F_{outflow}).

The brightness temperature of the CO(3-2) line peak (20.6 K) is similar to the kinetic temperature, which indicates that at systemic velocities the line is optically thick ($\tau \gg 1$). We therefore derived a T_{ex} of ~ 26.4 K from that spectrum. This value is similar to the one obtained in previous studies of similar sources (Phan-Bao et al. 2008, 2011, 2014), where T_{ex} ranges between 20 to 35 K.

The column density and the mass of the CO outflow are calculated following the prescription in Scoville et al. (1986) and Palau et al. (2007) for the CO(3-2) transition. The opacity, measured channel by channel in the four arc-like outflow structures, provides values of $\tau \ll 1$. We obtained a mean opacity value of 0.25 for both the blueshifted and redshifted South-west cavity as well as the redshifted North-east cavity, and a value of 0.15 for the blueshifted North-east cavity. Therefore, we consider that the wings of the CO(3-2) emission line are in the optically thin regime. Emission close to the position of the central object is optically thick, and therefore this emission was excluded from calculations. Consequently, it is possible that we are missing a part of the outflow mass because the border between the central object and the base of the outflow is almost indistinguishable.

We obtained a total outflow mass of $9.5 \times 10^{-7} M_{\odot}$ as the sum of the mass of the four arc-like structures: the sum of $3.4 \times 10^{-7} M_{\odot}$ and $2.3 \times 10^{-7} M_{\odot}$ for the blueshifted and redshifted components of the South-west lobe respectively, plus the sum of $9.8 \times 10^{-8} M_{\odot}$ and $2.8 \times 10^{-7} M_{\odot}$ for the blueshifted and redshifted components in the North-east lobe. The outflow velocities extend to -2.7 km/s in the blue-shifted lobe, and 9.3 km/s in the redshifted lobe, resulting in a v_{max} of ~ 6 km/s. In our

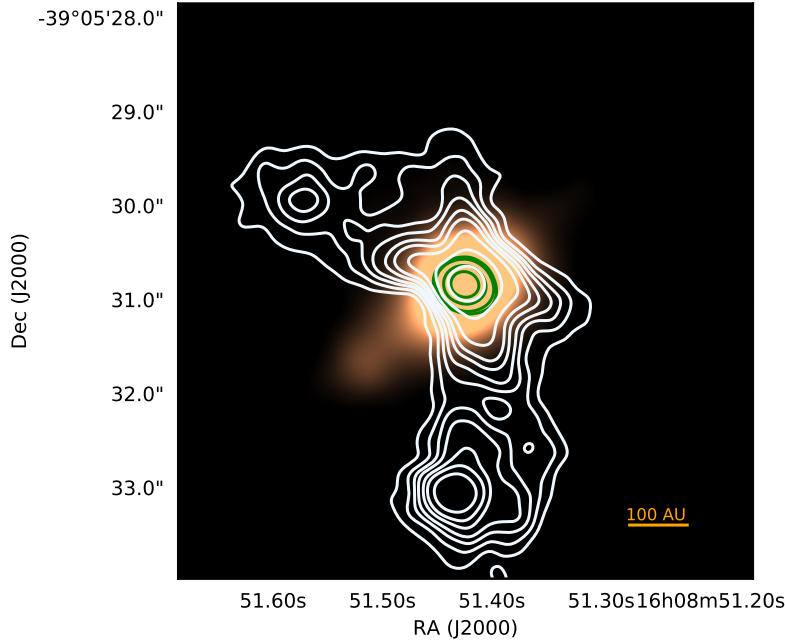


Figure 3.10: Left bipolar outflow cavity contour in white at 3, 5, 7, 9, 12, 15, 20 and 30 times the rms (1.88×10^{-3} Jy/beam) with robust of 2. Green contours are the ALMA continuum image at 0.89 mm using 5, 7, 15 and 25 times the rms value of (1.61×10^{-5} Jy/beam) with a robust value of 1.5. σ is the rms noise level of the map. Background color image is the [SII] optical jet from [Comerón & Fernández \(2011\)](#).

calculations we do not apply outflow inclination correction since due to the geometry of the outflow, close to the plane of the sky, the emission the CO(3-2) is very likely dominated by material lying close to the plane of the sky due to projection and opacity effects (our line of sight intercepts an amount of material larger at positions closer to the plane of the sky than at positions closer to the pole).

The rest of the dynamical parameters were obtained using the formulas in Tab. 3.3 and their values are: $\tau_{\text{dyn}} = 223$ yr, $P_{\text{outflow}} = 5.72 \times 10^{-7} M_{\odot} \text{ km/s}$, $E_{\text{outflow}} = 3.41 \times 10^{38}$ erg, $L_{\text{outflow}} = 1.21 \times 10^{-5} L_{\odot}$ and $F_{\text{outflow}} = 2.56 \times 10^{-8} M_{\odot} \text{ km/s yr}$.

Table 3.3: Outflow geometrical and dynamical properties

Derived properties	Formula
Length	R_{lobe}
Velocity	v_{max}
Dynamical time	$\tau_{\text{dynamical}} = R_{\text{lobe}} / v_{\text{max}}$
Mass-loss rate	$\dot{M} = M_{\text{outflow}} / \tau_{\text{dynamical}}$
Momentum	$P_{\text{outflow}} = M_{\text{outflow}} \times v$
Energy	$E_{\text{outflow}} = 1/2 M_{\text{outflow}} \times v^2$
Luminosity	$L_{\text{outflow}} = E_{\text{outflow}} / \tau_{\text{dynamical}}$
Force	$F_{\text{outflow}} = P_{\text{outflow}} / \tau_{\text{dynamical}}$

3.5 Discussion

3.5.1 Spectral index

The spectral index (α) at millimeter frequencies together with high angular resolution millimeter observations can be a powerful tool to infer the presence of grain growth signatures under the assumptions of the emission being in the Rayleigh-Jeans regime and optically thin emission. The spectral index, in the optically thin regime, provides information on the dust opacity index (β), where different values indicate different dust sizes and consequently of the presence of grain growth in the case of large dust particles. Typical values for the ISM are close to 1.7 (Draine 2006), while lower values ≤ 1 are indicative of the existence of grain growth (Ricci et al. 2010b,a; Ribas et al. 2017). Assuming the emission corresponding to the Rayleigh-Jeans regime and optically thin emission α is associated with the flux as $F_\nu \propto \nu^\alpha$ where $\beta = \alpha - 2$.

The spectral index, α , obtained from the SED is defined as:

$$\alpha = \frac{\log \frac{F_{328}}{F_{225}}}{\log \frac{328\text{GHz}}{225\text{GHz}}} \quad (3.2)$$

where F is the flux density at a certain frequency. Using the values given in Tab. 3.1 we obtained that the Par-Lup3-4 spectral index is 1.60 ± 0.95 (or $\beta = -0.40 \pm 0.95$). We use as flux uncertainty $2\times$ the rms. This value is in agreement with the grain growth scenario as it was proposed by (Fernández & Comerón 2005) even if we use just one σ errors. On the other hand, α values below 2 may also point to a framework where the assumed conditions, Rayleigh Jeans regime or optically thin disks, are incorrect (Ansdell et al. 2018). Additionally, grain growth in the (sub)mm regime can only be confirmed when the disk is resolved, which is not the case here. Thus, the α value might be related to a cold compact thick disk instead of dust grain growth.

The spectral index for Par-Lup3-4 of 2.34 ± 1.37 derived from the ALMA observations by Ansdell et al. (2016) and Ansdell et al. (2018) is compatible with our measurement inside the errors. We did not find any spectral index reported in the literature for any other VLM star, but we found the values obtained for BDs in other SFRs for comparison. Specifically, ρ Oph and Taurus (Ricci et al. 2014; Testi et al. 2016a) have sources with spectral indices $\sim 2-2.4$, pointing to the presence of large grains. Our result is compatible with these two studies. On the other hand the number of sources with measured spectral index is too small to draw definitive conclusions.

Finally, we note that the high inclination of the disk may affect the spectral index value that we measure. According to the models by (Galván-Madrid et al. 2018, Fig. 10), there is a dependence between the inclination and the spectral index, which may also contribute to the explanation of the low value that we obtained.

Furthermore, the spectral index has been measured just in a small frequency interval and future observations with ALMA covering a wider range of frequencies at higher spatial resolution are needed to measure more accurately the spectral index.

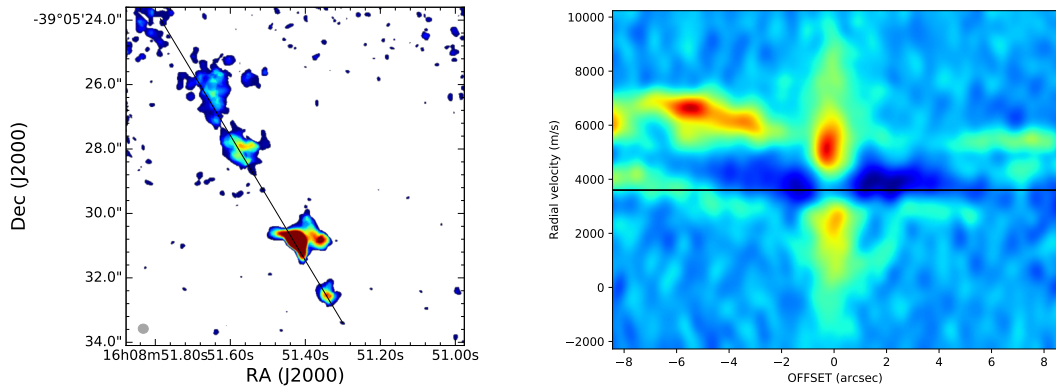


Figure 3.11: Left panel: CO ($v=0$ 2-1) ALMA velocity map towards Par-Lup3-4, black line mark the position where the position diagram map on the right panel was located. Right panel: Position-velocity diagram for the CO ($v=0$ 2-1) assuming a PA of 32.19 deg and a width of ~ 2.6 arcsec.

3.5.2 A possible secondary molecular outflow?

This subsection discusses the nature of the elongated and clumpy structure observed in Fig. 3.7 and Fig. 3.11. The structure is propagating from the center towards the North-west side of the field of view. Here we discuss four possible origins of this structure.

First, it is possible that this structure is a second molecular outflow originating from Par-Lup3-4. This can be explained by a close binary, and that possibility should not be excluded given that we are not resolving the dust disk and despite the fact that no binary companion could be detected so far. Additionally, another argument in favour of this possibility is that the emission is extending from the location of Par-Lup3-4. The emission is detected with a velocity of ~ 5.4 km/s at a distance of ~ 2 arcsec (310 au) North-east of the source; and up to ~ 6.7 km/s at a distance of ~ 6 arcsec (930 au) from the source, as seen especially in the position-velocity diagram of Figure 3.11. Both Band 6 and 7 show very similar morphologies and velocity patterns. The outflow appears monopolar, as there is no counterpart with emission moving towards the South-west. Monopolar outflows are not uncommon in the literature for low-mass stars (Codella et al. 2014; Louvet et al. 2018). Although the position of this second molecular outflow, perpendicular to the optical jet, is less likely, a similar scenario with two perpendicular outflows has been seen previously in other sources (Tobin et al. 2015); this could be interpreted as another indication of the binary nature of the central source.

A second possibility is that we are observing cloud contamination. In support of this hypothesis, we note that the velocity of the structure is very close to the velocity of the second component of the cloud. In the same low-velocity regime, we also detect extended cloud emission compatible with the cloud velocity. However, we detect very compact structures when we do a visibility taper over the shorter baselines (see Fig. 3.12), and inhomogeneities with this morphology in molecular clouds, although possible, they are not common. It is also not expected that we see clear strips in the field of view pointing towards Par-Lup3-4 along several channels instead

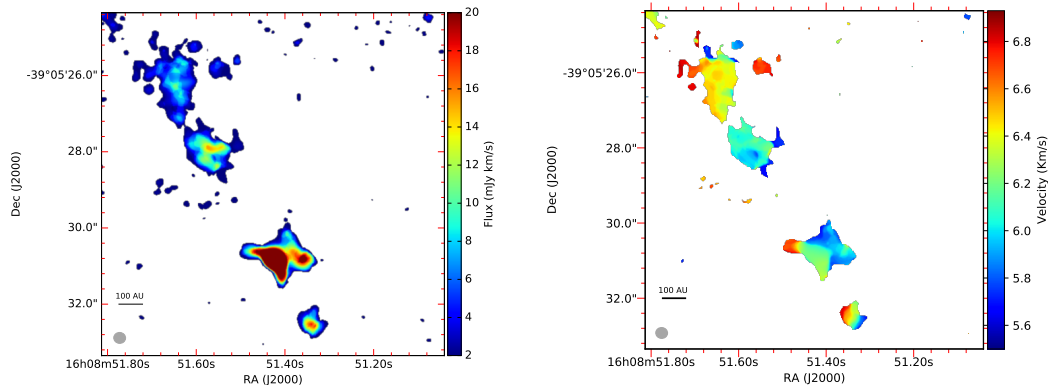


Figure 3.12: Left panel: CO ($v=0$ 3-2) integrated ALMA map. Right panel: CO ($v=0$ 3-2) ALMA velocity map. Beam size is represented by the grey ellipse in the bottom left corner. Only pixel values above 5σ are included in both panels. We used a uv taper >50 k λ .

of randomly distributed material as we can see in the channels with a velocity higher than 5.70 km/s in Fig. 3.13.

A third scenario is that the outflow is coming from another source that is neither Par-Lup3-4 nor a close companion. In this case a visual binary would be responsible for the molecular outflow.

Finally, a fourth scenario is that the outflow originates from the same source associated with unresolved H α emission detected by Fernández & Comerón (2005). H α emission is usually related to magnetospheric accretion in young stellar objects (Koenigl 1991) or in BDs as companions (Santamaría-Miranda et al. 2018). This H α emission is located at a distance of 4.2 arcsec from Par-Lup 3-4 with a PA ~ 30 or ~ 210 , in the direction of the emission that we detected. The nature of this source is unconfirmed, but Fernández & Comerón (2005) suggest that it could be a very low-mass brown dwarf, if its association to the Lupus 3 cloud can be assured. In our case, we do not find any detection in continuum from either ALMA Band 6 nor Band 7 coincident with the location of the H α emission. There is also no detection at optical or infrared wavelengths. Based on the rms of our ALMA Band 6 and Band 7 observations, we set an upper limit for the mass of the potential source of $0.05 \pm 0.01 M_{\text{Jup}}$ or $0.09 \pm 0.02 M_{\text{Jup}}$, respectively.

The current (sub)mm and optical observations cannot discriminate between the four scenarios. Future studies using ALMA should be able to unveil the origin of the moving structure. Higher angular resolution observations may be able to detect a close binary; observations with better velocity resolution and higher sensitivity may also help to distinguish between outflow and cloud emission in the second scenario.

3.5.3 SED Fitting

We aimed at fitting the SED of Par-Lup3-4 using the newly available data. For this purpose, we first compiled the photometric data of the target from the optical to the mm, including data from the Herschel Space Observatory (Herschel Pilbratt et al.

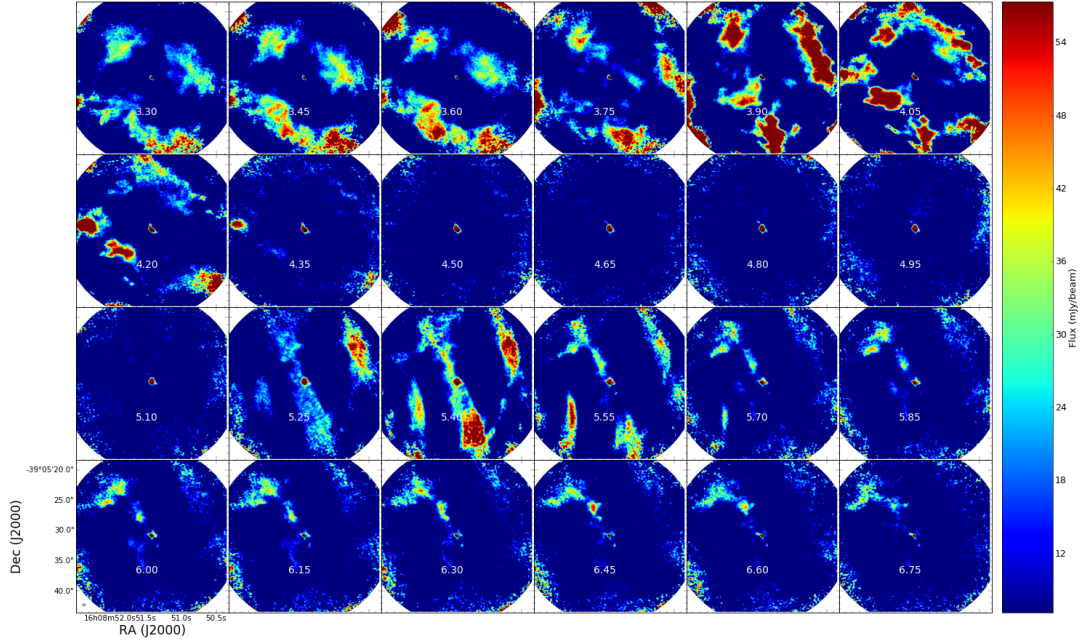


Figure 3.13: CO ($v=0$ 3-2) channel maps towards Par-Lup3-4 and the second outflow. The velocity of the channels is shown in the LSR frame, centered at the frequency at the velocity of CO (3-2). All maps share the same linear color scale. Black star is the position of the peak intensity in the continuum image.

Table 3.4: Best-fit parameters from SED modeling.

Parameter	JHK from 2MASS	JHK from Comerón et al. (2003)
Stellar radius (R_{\odot})	2.0	2.0
Disk dust mass (M_{\odot})	5×10^{-7}	1×10^{-7}
Maximum grain size (mm)	10	0.5
Scale height at 100 au (au)	20	20
Flaring index	1.2	1.1
Surface density index	-1.5	-1.0
Inclination (deg)	82.5	85
Interstellar extinction (mag)	3.5	2.5

2010), and the new ALMA observations. Then, we used the radiative transfer code MCFOST (Pinte et al. 2006, 2009) to infer disk properties.

Modeling protoplanetary disks involves defining several free parameters, many of which are highly uncertain or degenerate. Such a scenario is better dealt with within a Bayesian framework and using statistical tools such as Markov Chain Monte Carlo methods, but this approach is computationally very demanding and has only been applied in a small number of cases (e.g. Ribas et al. 2016; Wolff et al. 2017). Given the limited amount of data available at long wavelengths for Par-Lup3-4, we chose to run a grid of models to obtain a general idea of the system parameters.

Our initial attempts at fitting the SED of Par-Lup3-4 used fixed stellar parameters from the BT-Settled models (Allard et al. 2012; Baraffe et al. 2015) based on previous studies. The stellar temperature was set to 3200 K (Alcalá et al. 2017), and age estimates for the source range from 1 to 3 Myr (Comerón et al. 2003; Alcalá et al. 2017). Assuming 2 Myr and using the BT-Settled models, we derived a stellar radius and a mass of $1.1 R_{\odot}$ and $0.2 M_{\odot}$, respectively. Based on the Gaia DR2 (Gaia Collaboration et al. 2018) catalog (parallax = 6.63 ± 0.61), the distance to the source was set to $d \sim 155$ pc. This setup resulted in a significant underestimation of the optical fluxes, even assuming no extinction. Huélamo et al. (2010) found a similar problem in their modeling efforts of this source, but attributed it to an uncertain distance value. However, the distance measurement and uncertainty in the distance estimate by *Gaia* clearly show that this is not the case, and the source must be intrinsically more luminous in order to reproduce the observed fluxes. For this reason, we included the stellar radius as a parameter in the modeling process. Regarding the disk parameters, we have fixed the disk inner radius and the minimum grain size to 0.05 au and $0.005 \mu\text{m}$, respectively, following Huélamo et al. (2010).

For our model, we have defined eight free parameters and explored them within reasonable ranges:

- the stellar radius, including the value of $1.1 R_{\odot}$ derived from isochrones, plus 1.5, 2, and $2.5 R_{\odot}$ as additional values,
- disk dust mass, from 1×10^{-7} to $1 \times 10^{-5} M_{\odot}$ in steps of 0.5 dex,
- maximum grain size, from $500 \mu\text{m}$ to 1 cm in steps of 0.5 dex,
- scale height at 100 au, from 5 to 20 au in steps of 5 au,
- flaring index, with values 1.0, 1.1, and 1.2,
- surface density index, with values -0.5, -1.0, and -1.5,
- inclination, with values 80, 82.5, and 86 deg, based on the inclination derived from the optical jet. Fernández & Comerón (2005) derived a jet inclination less than 8° , and (Comerón & Fernández 2011) derived a jet inclination value of $6^{\circ}7 \pm 1^{\circ}4$.
- interstellar extinction values, from 0 to 5 mag in steps of 0.5 mag.

χ^2 values were then computed for each model. We note that there are two different results from near-IR observations (one from 2MASS and from Comerón et al. 2003),

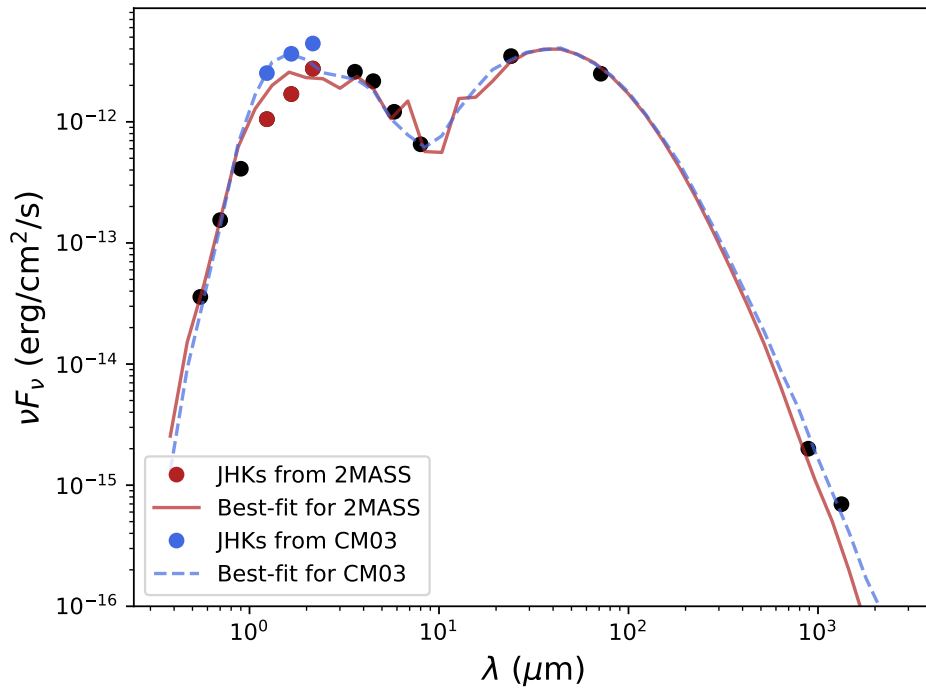


Figure 3.14: SED and modeling results for Par-Lup3-4. Dots are photometric observations. Red and blue dots are the 2MASS and the Comerón et al. (2003, CM03) observations, respectively. The best-fit models from our modeling efforts are also shown with a similar color code.

possibly reflecting the variable nature of Par-Lup3-4. Thus, two different χ^2 values were computed for each model.

The results from the SED modeling are shown in Table 3.4 and Fig. 3.14. While most of the fitted parameters are highly degenerate and unconstrained, one crucial result of the modeling process is the fact that a radius of $2 R_{\odot}$ is required in both cases. In fact, different tests varying the source distance/radius showed that it is not possible to fit the optical part of the observed SED with a source of 3200 K and a radius of $1.1 R_{\odot}$ at the distance of 155 pc estimated by *Gaia*, since the source is simply not bright enough. Given the small uncertainties associated with the parallax in the *Gaia* DR2 catalog, and the fact that its distance is compatible with that of other sources in the region, a plausible explanation is that the radius of Par-Lup3-4 is larger, and thus it is younger than the median age of Lupus. This idea is also supported by the presence of a molecular outflow, and by the fact that the source appears to be still embedded in the cloud. If this is the case, it is likely that Par-Lup3-4 is still surrounded by a substantial amount of material from the envelope.

A second explanation for the observed luminosity of Par-Lup3-4 is that the source is a binary system. If this is the case, the perpendicular structure described in section 3.5.2 could be an outflow originating from the companion. The secondary outflow is highly collimated, indicating a Class 0/I evolutionary stage. In that case, the SED is the combination of the SED of an evolve source with maximum in the optical/near infrared and the SED of a Class 0/I source that mostly contributes in the mm wavelength regime. However, no clear signature of a companion has been found so

far. If any of these two scenarios applies, the disk parameters derived from our modeling process should be treated with caution, since the models used may not reflect the true nature of the source.

We note that there is a factor of 2 to ~ 10 in difference between the dust disk mass obtained from the SED and the values obtained in Section 3.4.1. We acknowledge that the model itself may need to be refined in order to minimize this discrepancy, although the optically thin emission assumption may be another source of incompatibility.

The SED fitting done in Huélamo et al. (2010) showed some degeneracies between age and distance. Now that we are certain that the distance is not the main problem, then either the source is younger than expected, or it is actually a combination of two sources that a simple model as done in Huélamo et al. (2010) or this work, cannot solve.

3.5.4 Characterizing the molecular outflow cavity

Par-lup3-4 is the first VLM star to date for which we detected the base of a bipolar molecular outflow at (sub)mm-wavelengths, and for which the highly supersonic outflow (jet) has been detected at optical wavelengths (see Fig. 3.10). Following the low-mass star outflow model, the interaction between the jet or the wide-angle outflow and the envelope creates the detected cavities (Li & Shu 1996). The expelled gas and material is carving out the cavities in the envelope, and the interaction in the boundary between the outflowing gas and the envelope material creates the physical conditions for exciting the CO transitions that we detected. In this section, we characterize the VLM outflow of Par-Lup3-4 in the context of mass ejection from low-mass stars.

The first property that we use to characterize the outflow is the outflow size, which in the case of Par-Lup3-4 is ~ 1.8 arcsec (~ 295 au). This size considering the errors in the measurement is similar to the length of other VLM sources, such as ISO-Oph 102, GM Tau, MHO 5 (Phan-Bao et al. 2014), IC348-SMM2E (Palau et al. 2014) or L1148-IRS (Kauffmann et al. 2011), which have outflows between 500 to 1800 au. While the outflow size for low-mass stars is between 0.1 to 10 pc (20626.5 and 2062650 au) (Arce et al. 2007b, and references therein), one order of magnitude higher than the sizes that are found in VLM sources. Therefore, Par-Lup3-4 size is similar to other VLM sources and scaled-down from that of low-mass stars.

The outflow velocity measured for Par-Lup3-4 is slightly higher (6 km/s) but of the same order as the velocities observed for other VLMs, which are between 1 to 4.7 km/s (Phan-Bao et al. 2008; Kauffmann et al. 2011; Phan-Bao et al. 2014). Low-mass stars have velocities in the range between 10-100 km/s (Arce et al. 2007b, and references therein). Par-lup3-4 velocity is closer to the VLM regime than that of low-mass stars.

The disk mass of Par-Lup3-4 is $(2.0 - 2.3) \times 10^{-4} M_{\odot}$. Low-mass star disk masses are in the range of 10^{-3} to $10^{-1} M_{\odot}$ and the theoretical values obtained for VLM disks using radiative transfer algorithms extends from 10^{-6} to $10^{-3} M_{\odot}$. The disk

mass measured for Par-Lup3-4 therefore points towards a scaled-down version of the low-mass star disks, although we may be facing optically thick emission which might imply that the mass inferred from our ALMA observations may represent a lower limit.

Par-Lup3-4 has a molecular outflow mass of $\sim 10^{-6} M_{\odot}$ that is in the range of the observed values for other VLM sources that span 10^{-4} to $10^{-6} M_{\odot}$ (Phan-Bao et al. 2014). As pointed out by Phan-Bao et al. (2014), the VLM outflow values are at least one order of magnitude lower than the values obtained for low-mass stars in a similar evolutionary status.

The mass-loss rate from Par-Lup3-4 ($\dot{M}_{\text{outflow}} = M_{\text{outflow}} / \tau_{\text{dyn}}$) is $4.27 \times 10^{-9} M_{\odot} / \text{yr}$. The outflow mass-loss rate for a typical low-mass protostar ranges from $10^{-4} M_{\odot} \text{ yr}^{-1}$ to $8.9 \times 10^{-9} M_{\odot} \text{ yr}^{-1}$, although the median value is $10^{-7} M_{\odot} \text{ yr}^{-1}$ (Levreault 1988b). The mass-loss rate for VLM sources is lower, with values lying between 2×10^{-7} and $0.25 \times 10^{-8} M_{\odot} \text{ yr}^{-1}$ (Phan-Bao et al. 2014). The mass-loss rate for Par-Lup3-4 is even lower than the expected value for VLM sources, but this could be an effect of the potentially missed flux emission from the whole outflow extension that we are not observing.

The mass-loss rate of the stellar wind was obtained as $\dot{M}_{\text{wind}} = M_{\text{outflow}} v_{\text{max}} / \tau_{\text{dyn}} v_{\text{wind}}$ [M_{\odot} / yr] (Phan-Bao et al. 2014). We used a wind velocity of $168 \pm 30 \text{ km/s}$ (Comerón & Fernández 2011). We assumed that the momentum from the jet is completely transferred to the molecular outflow, as it may happen in Class II sources. The wind mass-loss rate derived for Par-Lup3-4 is $1.53 \times 10^{-10} M_{\odot} / \text{yr}$, very similar to the value of MH5, another VLM star in (Phan-Bao et al. 2014). We compare the outflow mass against the mass-loss rate of the stellar wind for Par-Lup3-4 along with other VLMs and low-mass stars using low resolution observation in Fig. 3.15 and it seems to be the case that Par-Lup3-4 is following the trend of more massive sources pointing to a similar formation mechanism to low-mass stars.

Accretion and outflow/jet/winds are phenomena that are deeply linked (Hartigan et al. 1995; Calvet et al. 1997; Rigliaco et al. 2013; Natta et al. 2014). As the material infalls from the envelope/disk onto the central source, a jet - perpendicular to the disk - is launched on account of angular momentum conservation. The accretion rate in combination with the outflow properties can give us information about the history of the sources, especially about the episodic accretion, and therefore it can be related to the outflow properties; this has been shown in the case of the disk wind and EXor outburst in EXLup (Sicilia-Aguilar et al. 2012). The accretion rate of Par-Lup3-4 has varied in the last years: $1.4 \times 10^{-9} M_{\odot} \text{ yr}^{-1}$ (Comerón et al. 2003), $7.9 \times 10^{-10} M_{\odot} \text{ yr}^{-1}$ (Bacciotti et al. 2011), $5.0 \times 10^{-10} M_{\odot} \text{ yr}^{-1}$ (Whelan et al. 2014) and $4.3 \times 10^{-12} M_{\odot} \text{ yr}^{-1}$ (Alcalá et al. 2014). The first three measurements are compatible within the uncertainties but not with the last result. These measurements were using different extinction values but the difference with the last measurement can only be explained by episodic accretion. The ratio $\dot{M}_{\text{wind}} / \dot{M}_{\text{acc}}$ for VLMs is between 0.05 to 100 (see Table 3 in Phan-Bao et al. (2014)) while for low-mass stars the expected value is in the range of ~ 0.0003 -0.4 (Hartigan et al. 1995). Using the obtained wind mass-loss rate and the accretion rates from the literature the relation $\dot{M}_{\text{wind}} / \dot{M}_{\text{acc}}$ spans between 0.07 to 22, in the expected range for VLMs.

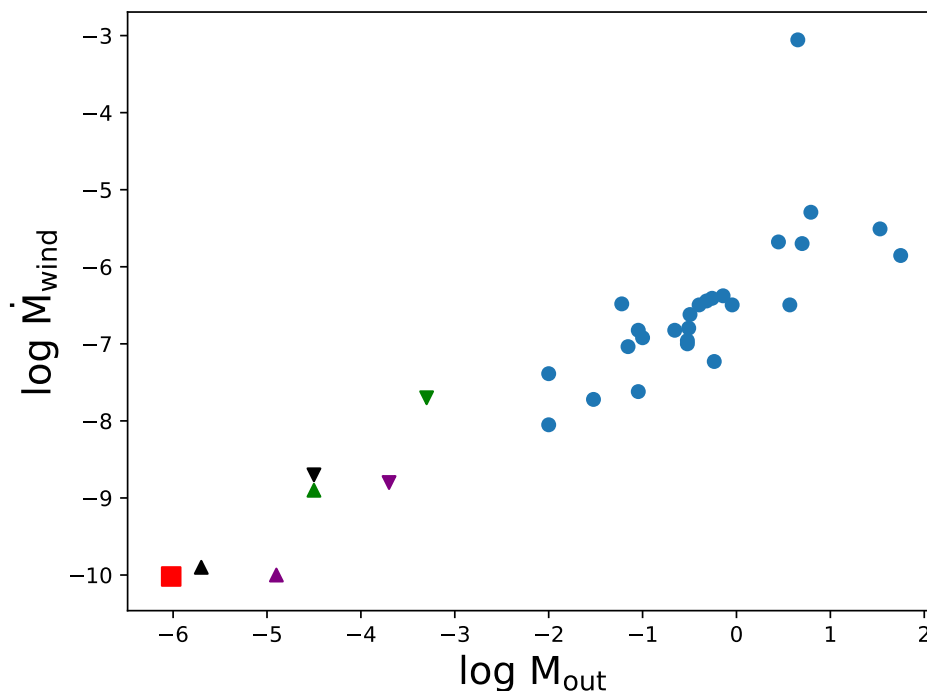


Figure 3.15: Molecular outflow mass versus wind mass-loss rate of Par-Lup3-4 (red), very low-mass sources (upper and lower limit triangles) from Phan-Bao et al. (2014) and Class II young stellar objects (blue circles) (Levreault 1988a).

Additionally, we investigated another parameter – opening angle – that can be used for evolutionary classification. The wide opening angle of the outflow, described in section 3.4.3, has an average value of 112° between both lobes. Previous studies in low-mass stars have discussed the relation between the age or evolutionary classification and the opening angle, as the angle broadens with age (Offner et al. 2011). Arce & Sargent (2006) classify low-mass stars as: Class 0 with opening angles $\leq 55^\circ$, Class I if the angle is $\geq 75^\circ$ and Class II when the outflow has no clear structure. A year later, Arce et al. (2007b) defined the boundary for Class I as $\geq 90^\circ$. Par-lup3-4 is consistent with Class I based on these studies, near to the transition to Class II given the wide opening angle, although these values are still under discussion in the field and cannot be considered as the only parameter to classify the evolutionary stage of the source. Unfortunately, there are no previous records in the literature about the opening angle in VLM sources. Future studies should correlate opening angle and classification in VLM sources, to test if they are indeed formed following a scaled-down version of low-mass star formation.

3.5.5 VLMs as a scale down version of low-mass?

In the previous section, we reviewed the outflow properties of Par-Lup3-4. Properties such as the outflow size, the velocity, outflow mass, wind mass and the disk mass are in the expected range for VLM sources. Previous studies on VLM sources (e.g. Phan-Bao et al. (2014)) point out that the formation of VLM sources follows a scaled-down version of low-mass star formation.

While these characteristics hint at a scaled-down version of star formation, there are still several uncertainties in the measurements that may further constrain this. For example, there are uncertainties related to the outflow mass calculation, such as the excitation temperature or the CO abundance relative to the H_2 , that can vary a factor of three (Dunham et al. 2014, and references therein). In the case of Par-Lup3-4, one of the main source of errors comes from the geometry of the outflow, which is not fully revealed with our interferometric ALMA data. This directly impacts the average length of the outflow and the dynamical time (propagating the uncertainties into the dynamical parameters), which may not be that short if we are able to reveal the whole extension and shape of both outflow lobes. Another important source of uncertainty is the missing flux of possible faint extended emission in our observations; the maximum outflow size that we detect is 2.9 arcsec but the largest recoverable scale for the used ALMA configuration is 7.29 arcsec. Therefore, we might be suffering from both effects, filtering extended flux with the interferometer, as well as and not having enough sensitivity.

Additionally, previous studies of VLM sources are biased due to low sensitivity observations, showing a smaller velocity range, thus affecting the dynamical properties. Another important bias in the previous studies comes from the inclusion of face-on disks or disks inclinations up to 30° , because it is easier to detect such system than in edge on disks. Previous observation of molecular outflows in VLMs sources could be affected by the limited sensitivity affecting the low detection rate found so far (e.g. Phan-Bao et al. (2014)). With this work we proved that we can detect a very faint amount of expelled mass due to the high ALMA sensitivity with enough resolution to observe the base of the outflow. Therefore, we conclude more sensitive observations are a must to infer more realistic detection rates of the presence of outflows in these sources.

In spite of the uncertainties and the small and biased sample of VLMs with outflows, the main conclusion that the formation of VLMs can be understood as a scaled-down version of low-mass stars still remains.

3.5.6 Revealing the true nature of Par-Lup3-4

Par-Lup3-4 is a complex source that may help to understand the formation of VLM sources. Previous SED fitting (Huélamo et al. 2010) showed degeneracies between age and distance. The last Gaia data release broke the degeneracy thanks to a precise distance value. Our SED fitting was underluminous in the optical and this can only be explained with two main possibilities either the source is younger than expected or it is a binary. The presence of a bipolar molecular outflow, which is more common in Class 0 and I sources, with the opening angle of the outflow points to a younger nature than Class II and this is in agreement with one of the modelling results. We detected a possible secondary outflow, among the four possible explanations that we discuss one of them is the existence of a binary that is in agreement with the SED fitting. If the source is younger than expected then the moving structure will be cloud material.

Future observations may help to disentangle the true nature of Par-Lup3-4. Higher velocity resolution observation with ALMA may help to differentiate between outflow material and cloud contamination or denser tracers that are not expected in the ambient cloud. Higher spatial resolution observation might be able to reveal the existence of a binary in Band 3, or similar frequency where the dust it is not optically thick.

3.6 Conclusions

Par-Lup3-4 is a very low-mass star located in the Lupus 3 cloud. It has an edge on disk with an optical jet. We observed Par-Lup3-4 using ALMA Band 6 and 7, and we detected continuum and gas emission for three molecular lines (CO J=2-1, CO J=3-2 and ^{13}CO J=3-2). These observations revealed for the first time the faint base of a molecular outflow and the cavity walls associated with this source, and a rotation pattern is seen with ^{13}CO near location of the continuum source. The main results from this work are the following:

- The dust disk is faint and unresolved. The total mass of the disk is between 0.21 and 0.24 M_{Jup} .
- The spectral index of 1.60 ± 0.95 is compatible with grain growth, as well as the optically thick regime. This value is influenced by the high disk inclination.
- SED fitting shows that the source is underluminous in the optical. This can be related to a younger age than previously expected or to the presence of a binary companion.
- The maximum extent of the outflow is ~ 450 au, a relatively small length for an outflow in the very low-mass regime. The outflow mass is found to be $9.54 \times 10^{-7} M_{\odot}$ and the maximum outflow velocity we derive is 6 km/s. We may not be observing the full extent of the outflow, and as a consequence a portion of the outflow mass is also missed. Our observations put lower-limits on these outflows quantities.
- We detected a secondary structure that is moving from the location of Par-Lup3-4 to the North-west side, and perpendicular to the molecular outflow. Its nature can be related to a secondary outflow originating from Par-Lup3-4, an envelope remnant, or an outflow originating from a second source – either a true binary or a visual binary.

Based on these results we propose two scenarios: in one scenario this may be a very young source, and the secondary structures is in fact cloud contamination; in an alternative scenario, a binary is driving the secondary outflow, and also contributes to the SED that we measure. In addition to measuring particular characteristics of this VLM source, including the outflow length, mass and maximum velocity, we consider this source in the context of formation scenarios for substellar objects. We suggest that the derived quantities are all consistent with the formation of Par-Lup3-4 as a scaled-down version of low-mass star formation.

Chapter 4

Accretion signatures in the X-shooter spectrum of the substellar companion to SR 12

Published as [Santamaría-Miranda et al. \(2018\)](#) in MNRAS 475, 2994

Abstract

Brown Dwarfs (BDs) can be companions to stellar objects. In this chapter, we study if they are formed by disk fragmentation or as isolated BDs. About a dozen substellar companions orbiting young stellar objects or pre-main sequence stars at several hundred au have been identified in the last decade. These objects are interesting both due to the uncertainties surrounding their formation, and because their large separation from the host star offers the potential to study the atmospheres of young giant planets and brown dwarfs. Here, we present X-shooter spectroscopy of SR 12 C, a ~ 2 Myr young brown dwarf orbiting SR 12 at an orbital separation of 1083 au. We determine the spectral type, gravity, and effective temperature via comparison with models and observational templates of young brown dwarfs. In addition, we detect and characterize accretion using several accretion tracers. We find SR 12 C to be a brown dwarf of spectral type $L0 \pm 1$, $\log g = 4 \pm 0.5$, an effective temperature of 2600 ± 100 K. Our spectra provide clear evidence for accretion at a rate of $\sim 10^{-11} M_{\odot} \text{yr}^{-1}$. This makes SR 12 one of the few substellar companions with a reliable estimate for its accretion rate. A comparison of the ages and accretion rates of substellar companions with young isolated brown dwarfs does not reveal any significant differences. If further accretion rate measurements of a large number of substellar companions can confirm this trend, this would hint towards a similar formation mechanism for substellar companions at large separations and isolated brown dwarfs.

4.1 Introduction

In this Chapter, we study a BD in the boundary with the planetary regime. We investigate if planet formation theories can be applied to BDs in a protoplanetary disk instead of the theories explained in Chapter 1. Planetary mass or brown dwarf companions which orbit their host stars at separations exceeding 100 au are intriguing objects that may provide the potential to perform detailed investigations of the atmospheres of young giant planets and brown dwarfs. However, how these interesting substellar companions (SSCs) formed at separations of several hundred au (i.e. much

larger than most known exoplanets or brown dwarf companions) remains a mystery. The currently most accepted planet formation scenario of in-situ core accretion is unlikely to occur because the time required for core growth at these large distances significantly exceeds the typical lifetime of protoplanetary disks. Instead, several alternative scenarios have been suggested. [Pollack et al. \(1996\)](#) proposed that rocky planetesimals could grow to solid cores which are then scattered to larger separations where they accrete gaseous material to become the gas giant planets or brown dwarfs at large separations we observe. Alternatively, SSCs could represent the low-mass end of multiple stars that formed similar to stellar binary stars, i.e. their formation mechanism could be fragmentation of collapsing protostellar clouds (e.g. [Cha & Whitworth 2003](#)). Accretion in very young single brown dwarfs is consistent with direct fragmentation from collapsing molecular cores ([Thies et al. 2015](#)). SSCs could thus form the same way as single brown dwarfs as scaled-down version of low-mass stars with the only difference that they are members of multiple systems.

However, [Kratter et al. \(2010\)](#) pointed out that while this scenario offers a reasonable explanation for brown dwarf or stellar companions, it only works for the planetary mass companions if the companion forms at nearly exactly the time the circumstellar envelope is exhausted which can be considered rather unlikely. Another scenario that has been suggested for the formation of SSCs are gravitational instabilities (GI). If a massive gaseous disk becomes gravitationally unstable and fragments into a number of self-gravitating bound structures ([Boss 1997](#)), these structures can then further collapse to become giant planets or brown dwarfs. However, models suggest that while the disk instability can indeed form planets at separations 30-70 au ([Boss 2011](#)), it is unclear if the mechanism also works at separations of several hundred au (e.g. [Rafikov 2007](#)). To overcome this problem, SSCs could form closer and be ejected to large orbital separations ([Whitworth & Stamatellos 2006](#); [Stamatellos et al. 2007](#)). In addition, [Meru & Bate \(2010\)](#); [Kratter & Murray-Clay \(2011\)](#) find that gravitational instabilities only occur for a certain and rather narrow set of conditions.

Despite the increasing number of SSCs detected at more than 100 au from their host systems and masses below $30 M_{\text{Jup}}$ ([Neuhäuser et al. 2005](#); [Lafrenière et al. 2008](#); [Schmidt et al. 2008](#); [Deacon et al. 2016](#); [Naud et al. 2014](#)), we struggle to understand which formation mechanism is most appropriate. An important trait to study in order to progress with our understanding of SSC formation is whether they are still accreting gas and at what rate this accretion proceeds. Accretion plays a key role in the formation of all stars, brown dwarfs, and giant planets. Unfortunately, clear evidence based on spectroscopy for accretion in SSCs has been reported only for FW Tau b, CT Cha b and GSC 06214-00210 B ([Bowler et al. 2014, 2011](#); [Wu et al. 2015b](#)).

Throughout this work we thus assume an age of ~ 2 Myrs keeping in mind that this value represents a very rough estimate. The projected separation between SR 12 C and the central T Tauri star on the sky is ~ 8.7 arcsec, which corresponds to $\sim 1083 \pm 217$ au at 125 ± 25 pc ([de Geus et al. 1989](#)). [Kuzuhara et al. \(2011\)](#) obtained NIR spectra of SR 12 C with CISCO mounted on the Subaru telescope. They further showed that the probability of an arbitrary alignment between SR 12 C and SR 12 AB is ~ 1 per cent. Based on theoretical age-luminosity relations the mass of SR 12 C has been estimated to be $0.013 \pm 0.007 M_{\odot}$ ([Kuzuhara et al. 2011](#)). [Bowler et al. \(2014\)](#) observed SR 12 C with IRTF/SpeX and obtained spectra that matched an $M9 \pm 0.5$

spectral type, corresponding to a $T_{\text{eff}} = 2400_{-100}^{+155}$ K using $SpT - T_{\text{eff}}$ relation provided by [Luhman et al. \(2003\)](#).

SR 12 C is an ideal object to test for accretion in SSCs because of its large separation from the central binary. We here present X-shooter spectroscopy of SR 12 C and provide clear evidence for ongoing accretion based on several accretion indicators. This makes SR 12 C just the fourth SSC with clear evidence for accretion. We also find that SSCs accrete at a rate similar to isolated objects and that accretion might perhaps cease at about the same age as in isolated low-mass objects.

4.2 Observations

The large spectral coverage of X-Shooter ([Vernet et al. 2011](#)), extending from the UVB to NIR, allows to probe simultaneously several accretion features (e.g. [Rigliaco et al. 2012](#); [Manara et al. 2013](#); [Alcalá et al. 2014](#)). We observed SR12 with X-Shooter on the second of May 2016. The weather conditions were photometric with good seeing (less than 1 arcsec). We used slit widths of 1.3, 1.5 and 1.2 arcsec for the UVB, VIS and NIR arm, respectively. The exposure time was 4000 s in total with a resolution of $R \sim 4000$ for the UVB, $R \sim 5400$ for the VIS, $R \sim 3890$ for NIR. Although SR 12 C is separated from the central binary by a few times the seeing, the large flux contrast with the primary precludes us from detecting it on the acquisition images. To obtain the required spectrum we thus applied blind offsets to the acquisition images to place the slit on the companion using the position angle and separation values provided by [Kuzuhara et al. \(2011\)](#). The obtained data were reduced with the X-shooter pipeline using the *stare* mode. The obtained SNR for the UVB were 2.3, 12.57 for the VIS arm, and 19.02 for the NIR arm. Telluric correction and sky subtraction was implemented with *molecfit* ([Kausch et al. 2015](#); [Smette et al. 2015](#)) and *Skycorr* ([Noll et al. 2014](#)). The σ clipping method was implemented to remove pixels deviating by more than 2.4σ from the median. To evaluate whether contamination from the central binary system affected our spectrum we fitted a combination of a Gaussian and a straight line to the 2D spectrum after binning 5 pixels in the dispersion direction. We do not find any evidence for a flux gradient in the background, which clearly confirms that contamination from the central binary is negligible.

4.3 Characterizing SR 12 C

The obtained X-shooter spectrum of SR 12 C covers the UV to NIR simultaneously and allows us to derive tight constraints on the physical properties of this young brown dwarf. To that end we fit both theoretical and observational templates to the X-shooter spectrum and derive spectral type, surface gravity, and temperature of the SSC.

4.3.1 Fitting model templates

We used a grid of spectra based on BT-SETTL models (Allard 2014) to fit the X-shooter spectrum. These model spectra assume solar abundances and cover near infrared to visible wavelengths. Our grid covered values of T_{eff} ranging from 1600 to 3000 K and gravities between $\log g = 2.5$ and 5.5 with a step sizes of 100 K and $\log g=0.5$, respectively. To isolate the purely photospheric features that should be reproduced by the models, we masked telluric regions in the IR and the most prominent emission lines, which were $H\alpha$, the Ca II triplet ($\lambda\lambda 8662, 8542, 8498 \text{ \AA}$), and the OI line at $\lambda 8446 \text{ \AA}$. We also resampled the theoretical spectra in order to obtain the same spectral resolution as the observed spectrum. We used the extinction law from Fitzpatrick (1999) with a fixed ratio of total to selective extinction ($R_V = A_V/E_{B-V} = 5.1$) leaving A_V as a free parameter to account for the intrinsic dust expected in the photosphere of brown dwarfs with effective temperature in the range from 2500 to 2700 K. This dust and its effect on the emitted spectrum is known to be not accurately described by the theoretical models (Manjavacas et al. 2014; Bayo et al. 2017). We furthermore added a component for the interstellar extinction with $R_V = 3.1$ and a fixed colour excess of $E_{B-V} = 0.4$ that was obtained fitting only the visual part of the spectrum where the extinction curve is in the linear regime (see Fig. 1 in Fitzpatrick 1999). For each theoretical spectrum we used least square minimization with the extinction produced by the dust in the photosphere of the brown dwarf and the scaling factor as free parameters. The best fit had a temperature of 2600 K and a surface gravity of $\log g = 4.0$ with reduced $\chi^2 = 10.3$. However, we note that models in the range of 2500 K to 2800 K and with $\log g$ between 3.5 and 4.5 fit almost equally well the observations with χ^2 values in the range of $\sim 10.5 - 11.0$. Based on visual inspection focusing on the shape of the spectrum in the J and H band, we finally estimate $T_{\text{eff}} = 2600 \pm 100 \text{ K}$ and $\log g = 4.0 \pm 0.5$. Combining these values for the effective temperature and the gravity with the isochrones from the BT-Settl models we derived an age estimate of 2 to 15 Myr (which is consistent with the 2 Myrs we assume throughout this work). The mass of SR 12 C we estimate this way is slightly larger (but still within 2σ) than previously estimated. Figure 4.1 compares the observed spectrum and the best-fitting model. The observed spectrum is plotted in red while the best fitting model spectrum is represented by the black line. In the wavelength range from 0.66 to $2.0 \mu\text{m}$ the model reproduces well the observations. However, in the K band the model predicts too much flux. As mentioned above, this effect is well-known and generally explained by the presence of dust in the atmosphere of the brown dwarf which increases extinction and which is not properly included in the models (Manjavacas et al. 2014; Marocco et al. 2014; Hiranaka et al. 2016). Our simple addition of an extra-extinction cannot entirely solve this issue most likely because extinction laws assume grain size distributions that do not need to match those of substellar atmospheres. In the H band, the spectrum shows a triangular profile previously reported by Bowler et al. (2014) and Kuzuhara et al. (2011). This feature is a commonly known indicator of low surface gravity (Martín & Zapatero Osorio 2003; Kirkpatrick et al. 2006) in agreement with the age derived for SR 12.

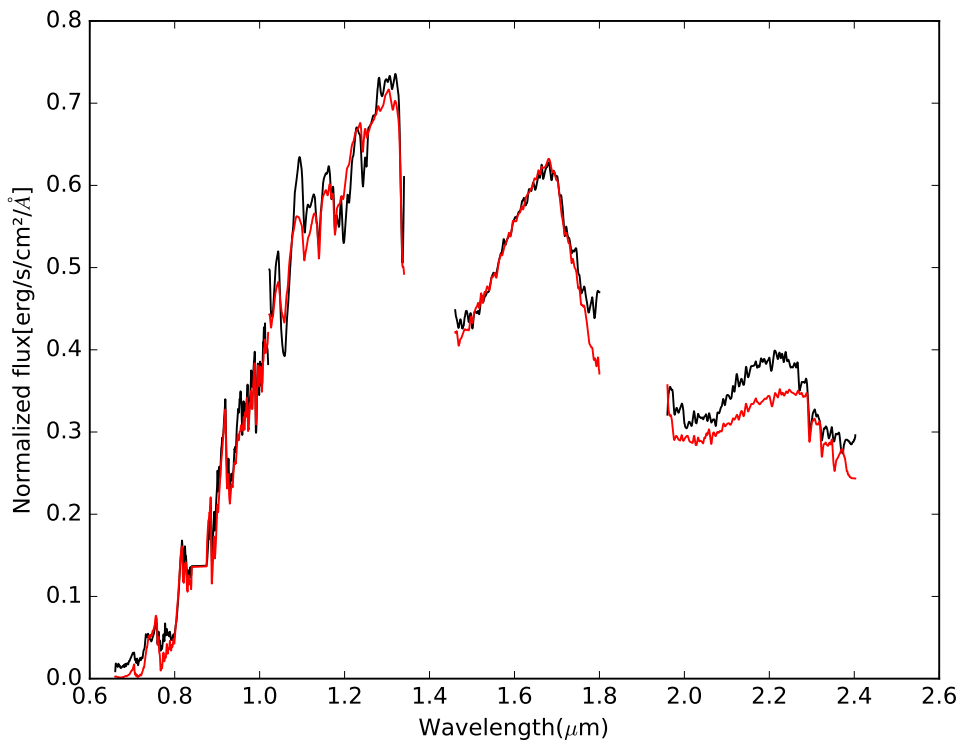


Figure 4.1: Theoretical spectrum (red line) fitted to the observed spectrum (black line). In general, the agreement is reasonable with exception of the *K* band, where the influence of the dust creates a higher level of extinction.

4.3.2 Observational template fitting

We used two sets of observational templates to determine the spectral type of SR 12 C. First we used a library of near-infrared (1.1–2.45 μm) integral field spectra of young M-L dwarfs with a resolution of $R \sim 1500\text{--}2000$ (Bonnefoy et al. 2014). These spectra were obtained with the Spectrograph for INtegral Field Observations in the Near Infrared (SINFONI) mounted at the VLT/UT4. The second set of spectra that we used was the SpeX prism Library (Rayner et al. 2003) which is a repository of low-resolution spectra, primarily of low-temperature brown dwarfs, obtained with the SpeX spectrograph on the 3m NASA Infrared Telescope Facility on Mauna Kea, Hawaii. The wavelength coverage of these spectra is 0.65 – 2.55 μm . We used both libraries as the SINFONI spectra have a resolution similar to our observations but cover just the near-infrared while the SpeX spectra cover the same wavelength range as our spectrum but with a significantly lower resolution. The combination of both libraries may provide the most accurate constraints on the spectral type of SR 12 C.

In both cases we resampled the observed SR 12 C spectrum to obtain the same resolution as the templates. We also de-reddened SR 12 C with $A_V = 1.24$ and $R_V = 3.1$. The value for A_V was obtained as explained in Sect. 4.3.1. The $\text{H}\alpha$ line and the Ca II triplet were masked out in the case of the SpeX prism Library. Using the SINFONI spectra we obtained the best fit ($\chi^2 = 5.6$) with 2M40141, a brown dwarf classified as L0. While the spectrum of the M9.5 object OTS 44 still provides a reasonable fit ($\chi^2 = 6.6$) the fit gets much worse if we move to earlier spectral types ($\chi^2 = 14.8$ for 2M1207 A with a spectral type M8.5). The library does not contain complete

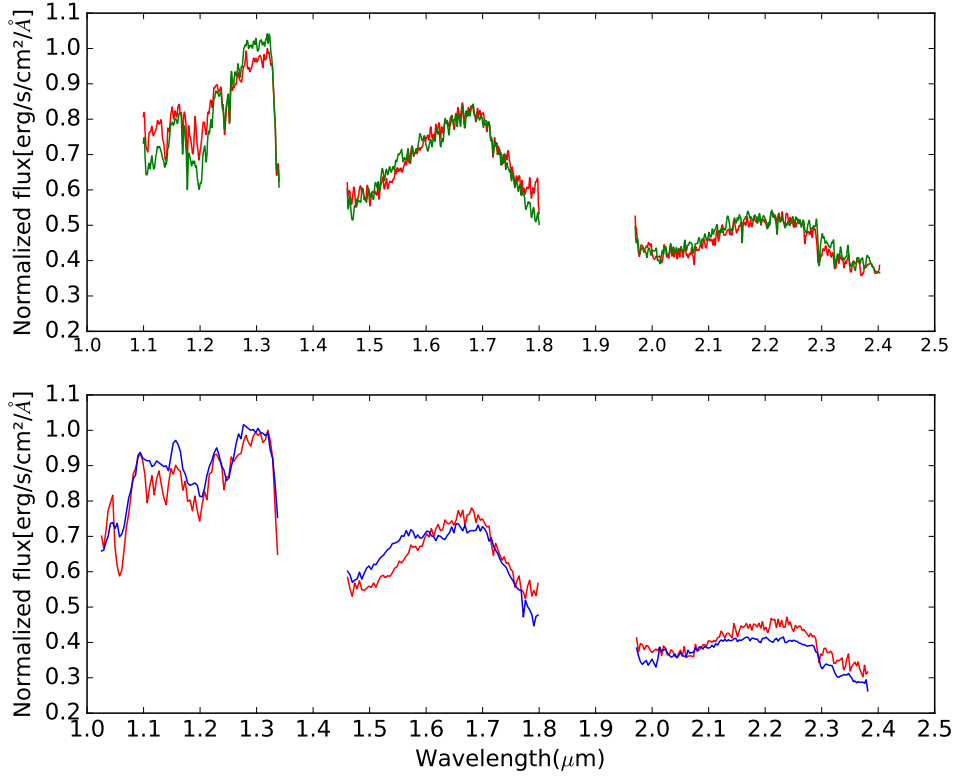


Figure 4.2: Top panel: Bonnefoy’s L0 template (green line) versus SR 12 C (red line). Bottom panel: SpeX Prism L0 template spectrum (blue line) versus SR 12 C (red line)

spectra for L1-L3 objects but the L4 object Gl417B does clearly not provide a good fit ($\chi^2 = 9.4$). The top panel of Fig. 4.2 compares the spectrum of SR 12 C (red line) with the scaled spectrum of 2M40141 (green line).

The best fit ($\chi^2 = 4.0$) using the SpeX library was obtained with 2MASP J0345432+2543023 which is classified as an L0 at optical wavelength and as an L1 \pm 1 brown dwarf in the NIR. While using M9 and L1 spectra available in the library (objects LHS 2924 and 2MASSW J1439284+192915) provides still reasonable agreement ($\chi^2 = 5.1$ and 6.5, respectively), earlier or later spectral types do clearly not provide acceptable approximations of our observations as χ^2 increases by more than a factor of three compared to our best fit.

The bottom panel of Fig. 4.2 shows the spectrum of SR 12 C (red line) versus a scaled version of 2MASP J0345432+2543023 (blue line). Both templates fit the *K* band much better than the theoretical spectrum which indicates that, despite significant recent progress, spectral models probably lack a proper description of the effects of dust in the atmosphere of brown dwarfs (Manjavacas et al. 2014).

Our results agree with previous studies. Kuzuhara et al. (2011) and also Bowler et al. (2014) obtained a M9 \pm 0.5 for the spectral type of SR 12 C. Using the T_{eff} -spectral type relation provided by Luhman et al. (2003), our spectral type determination converts to 2400 $^{+155}_{-100}$ K, in reasonable agreement with the value we found from fitting theoretical spectra. We conclude that SR 12 C should be classified as an L0 \pm 1 brown dwarf.

4.3.3 Radial velocity measurements

We measured the radial velocity of SR 12 C using two different features, the calcium triplet emission lines ($\lambda\lambda 8662, 8542, 8498 \text{ \AA}$) and the sodium absorption doublet ($\lambda\lambda 5889.9, 5895.9 \text{ \AA}$). We fitted the triplet and the doublet simultaneously and found radial velocities of $-6.1 \pm 1.0 \text{ km/s}$ (calcium triplet) $-7.4 \pm 2.8 \text{ km/s}$ (sodium doublet). We also reduced an archival spectrum of the central binary (SR 12 AB) which had been taken in the framework of ESO project 093.C-0506(A). This spectrum was taken with a position angle of $161^{\circ}.462$ degrees and a total integration time of 120 seconds. We fitted the same lines for the host star and we obtained the following radial velocities: $-6.7 \pm 0.5 \text{ km/s}$ (calcium triplet) and $-7.1 \pm 0.5 \text{ km/s}$ (sodium doublet). We conclude that there is no radial velocity difference between SR 12 C and the central binary system. This indicates that the formation scenario in which PMCs form close to the central object and are then ejected does probably not apply to SR 12 C.

4.3.4 Identification of absorption lines

While the main focus of this work is on accretion signatures and possible constraints on formation theories of PMCs, for the sake of completeness we investigated which photospheric absorption lines are present in our X-shooter spectrum. We used Fig. 2 of [Bayo et al. \(2017\)](#) as a reference for typical spectral features in late M and L dwarfs (see also [Jones et al. 1994](#); [Kirkpatrick et al. 1993](#); [Geballe et al. 1996](#); [Allard et al. 1997](#)). We identified several in the spectrum of SR 12 C that are common in late M and early L stars (see Fig. 4.3). A complete list of these lines together with the measured equivalent widths is given in the appendix D.

4.4 Accretion

As outlined in the introduction, an important parameter for constraining formation scenarios for SSCs is the age range in which these objects accrete and the associated mass accretion rates.

The X-shooter spectrum of the brown dwarf orbiting SR 12 contains clear evidence for ongoing accretion. According to the magnetospheric accretion model ([Koenigl 1991](#)) the stellar magnetosphere truncates the disk near the surface of the star. Material from the inner disk is transferred through magnetic field lines as accretion columns onto the high latitude regions of the star where it dissipates its kinetic energy in standing shocks ([Calvet & Gullbring 1998](#)). Shock fronts at the base of the accretion columns create a high temperature layer ([Koenigl 1991](#); [Gullbring 1994](#); [Lamzin 1995](#)) of $\sim 10^4 \text{ K}$ where the optically thick post shock gas and optically thin pre-shock gas generate emission leading to broad velocity profiles of $H\alpha$ and the CaII IR triplet. Other emission lines that are produced in the shocks at the base of the accretion columns and that are frequently used to measure accretion are the Paschen and the Balmer series, and Oxygen lines. We identified all these accretion

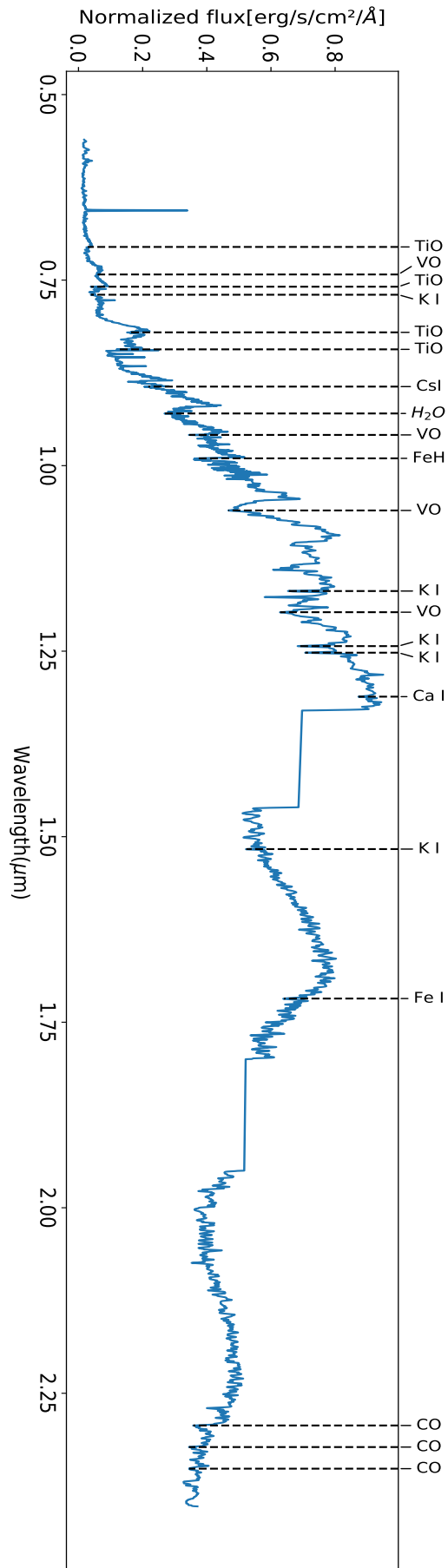


Figure 4.3: Spectral identification of the most common features in late M and early L types.

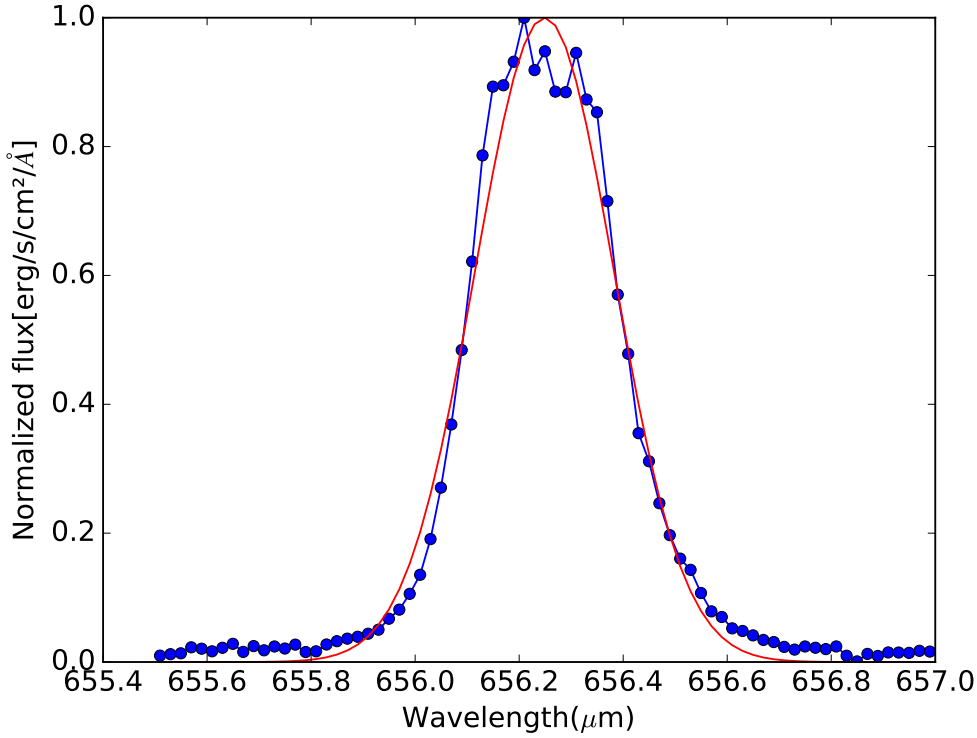


Figure 4.4: The observed $H\alpha$ line (blue) is fitted with a Gaussian profile (red). The irregular shape and top part of the line is related to magnetospheric accretion. The width at 10 per cent of the line corresponds to an accretion rate of $\dot{M}_{\text{acc}} = 10^{-10.31 \pm 0.5} M_{\odot} \text{yr}^{-1}$

tracers in the X-shooter spectrum of SR 12 C and measured the accretion rates using eight of them.

4.4.1 Accretion estimated from $H\alpha$ emission

$H\alpha$ is the most commonly used accretion indicator in Classical T-Tauri stars (CTTS). Accretion rates seem to correlate well with the $H\alpha$ 10 per cent width (Natta et al. 2004) where values $\gtrsim 200$ km/s (Jayawardhana et al. 2003) or $\gtrsim 270$ km/s (Cieza et al. 2010) are considered as evidence for accretion (see also Romero et al. 2012; Cieza et al. 2012, for a discussion). Less broad emission lines can be produced by chromospheric activity and cannot be interpreted as evidence for accretion.

Although this diagnostic was originally developed for CTTS it can be used for objects below the hydrogen burning limit as well. In brown dwarfs, $H\alpha$ has been used to measure accretion adopting the limit of ~ 200 km/s and using the following equation

$$\log \dot{M}_{\text{acc}} = -12.89(\pm 0.3) + 9.7(\pm 0.7) \times 10^{-3} H\alpha 10\% \quad (4.1)$$

where $H\alpha$ is in km s^{-1} and \dot{M}_{acc} in M_{\odot}/yr^{-1} (Natta et al. 2004). Using this method we obtain 266.3 km/s as the 10 per cent width which correspond to a $\dot{M}_{\text{acc}} = 10^{-10.31 \pm 0.5} M_{\odot} \text{yr}^{-1}$ (see Fig. 4.4).

Table 4.1: Characteristics of the observed accretion tracers.

Line (Å)	EW (Å)	Flux line (W/m^2)	$\log(L_{line}/L_{\odot})$	$L_{acc}(L_{\odot})$
H α λ 6562.8	-57.39 ± 17.71	$(1.34 \pm 0.05) \times 10^{-18}$	-6.19 ± 2.13	$(3.42 \pm 0.93) \times 10^{-6}$
H β λ 4861	-46.90 ± 4.21	$(2.19 \pm 0.03) \times 10^{-19}$	-6.64 ± 2.10	$(1.28 \pm 0.36) \times 10^{-7}$
H γ λ 4341	-23.06 ± 2.28	$(6.57 \pm 0.04) \times 10^{-19}$	-6.85 ± 2.10	$(2.53 \pm 0.69) \times 10^{-6}$
H11 λ 3771	-9.37 ± 0.44	$(8.93 \pm 0.12) \times 10^{-20}$	-7.33 ± 2.10	$(3.82 \pm 1.00) \times 10^{-6}$
OI λ 8446	-6.97 ± 0.50	$(1.61 \pm 1.29) \times 10^{-19}$	-7.10 ± 4.69	$(1.34 \pm 0.90) \times 10^{-5}$

Table 4.2: Accretion rates measurements for each emission line

Line	Wavelength (Å)	$\dot{M}_{acc}(M_{\odot}yr^{-1})$
H α	6562.8 ^a	$(4.90 \pm 5.64) \times 10^{-11}$
H α	6562.8 ^b	$(1.61 \pm 1.14) \times 10^{-12}$
H β	4861	$(5.99 \pm 4.25) \times 10^{-13}$
H γ	4341	$(1.18 \pm 0.84) \times 10^{-12}$
H11	3771	$(1.79 \pm 1.26) \times 10^{-12}$
OI	8446	$(6.28 \pm 5.88) \times 10^{-12}$
CaII	8544.2	4.57×10^{-12}
Pa β	12800	$(4.02 \pm 2.95) \times 10^{-13}$

Notes^a Measured as explained in Section 4.4.1^b Measured as explained in Section 4.4.5

4.4.2 Accretion measured with the Ca II triplet

The Ca II triplet emission lines are another frequently used accretion indicator in young stellar objects. These lines are present in SR 12 C and the line flux ratio clearly indicates accretion (see Fig. 4.5). As shown by Comerón et al. (2003), if the line flux ratio is close to 1:1:1, the lines cannot be produced by chromospheric activity because optically thin emission would cause line flux ratios of 1:9:5. Measuring the line flux ratio of the CaII triplet is therefore one of the most reliable accretion tracers. We measured the line flux ratio and obtained 1:1.37:1.09, a clear sign of ongoing accretion in SR 12 C.

Furthermore, Comerón et al. (2003) derived simple equations relating the accretion rate to the line flux based on the theoretical work of Muzerolle et al. (1998). These relations are:

$$\log \dot{M}_{acc} = -34.15 + 0.89 \times \log(F_{CaII(\lambda 8542)}) \quad (4.2)$$

$$\log F_{CaII(\lambda 8542)} = 4.72 \times 10^{33} EW() \times 10^{-0.4(m_{\lambda} - 0.54A_V)} \quad (4.3)$$

where $F_{CaII(\lambda 8542)}$ is the line flux, m_{λ} is the magnitude of the star at $\lambda 8542$, and A_V is the visual extinction at the wavelength of the line. Using the above relations we obtained an accretion rate of $4.57 \times 10^{-12} M_{\odot}yr^{-1}$ for SR 12 C.

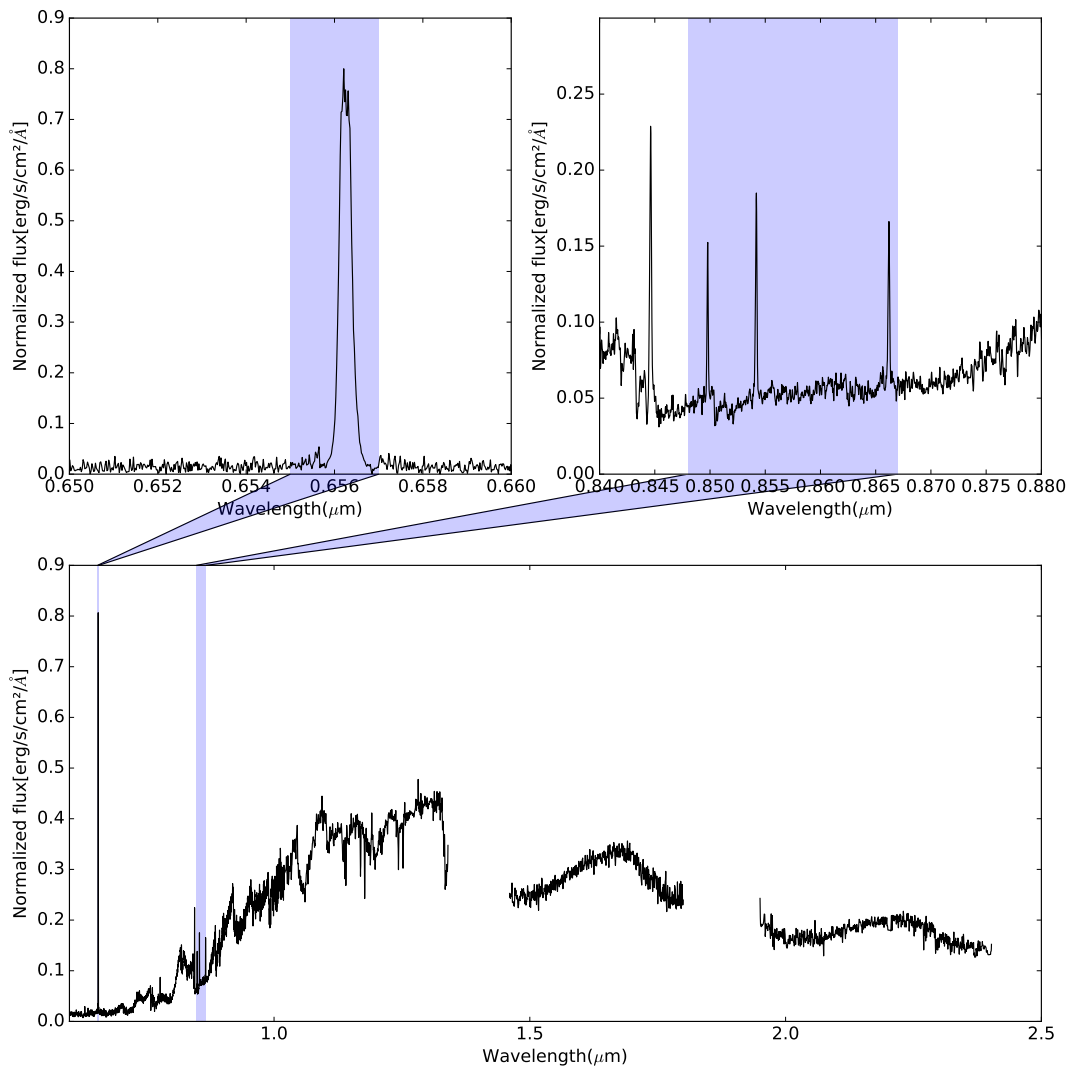


Figure 4.5: The X-shooter spectrum (covering the visible and J, H, K bands) of SR 12 C shows clear evidence for ongoing accretion (bottom pannel). In the top panels, we highlight the strong $H\alpha$ emission (lef-hand panel) and CaII triplet and OI line (right-hand panel).

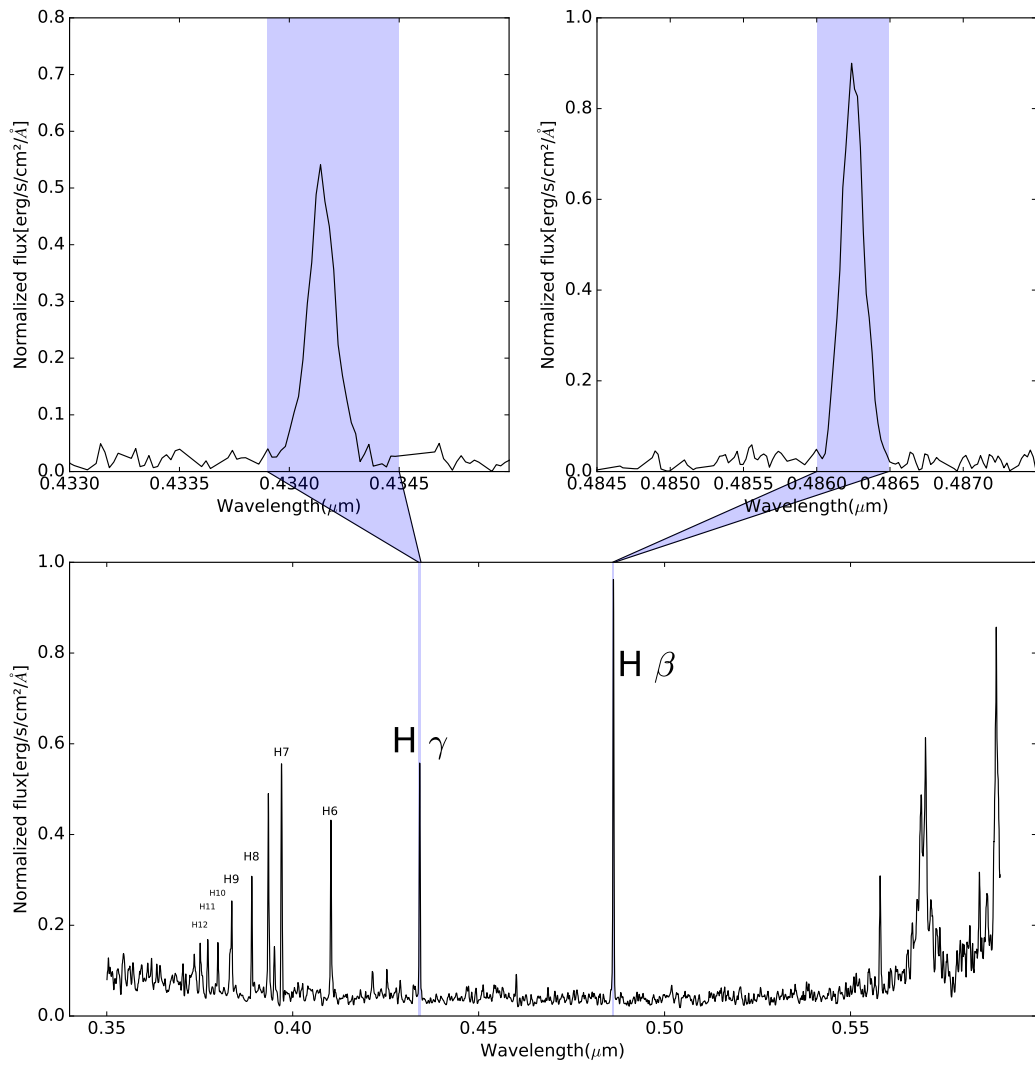


Figure 4.6: Bottom panel: SR 12 C UVB spectra, with the Balmer series labeled. Top left panel: H γ emission line. Top right panel: H β emission line.

Table 4.3: Wide (>100 au) companions under 15 M_{Jup} and younger than 10 Myrs

Object	Mass (M_{Jup})	Age (Myr)	Separation (AU)	SpT	Primary Multiplicity ^a	Accretion ^b	Accretion rate $\log \dot{M}(M_{\odot} \text{yr}^{-1})$	References
IRXS J1609-2105b	8^{+4}_{-2}	~ 5	~ 330	L2±1	S	N	-	1,2,3,4,5
ROXs 42B b	9 ± 3	7^{+3}_{-2}	~ 140	L1±1	B	U	-	6,7
FW Tau b	6-14	$2^{+1}_{-0.5}$	~ 330	-	B	Y	-11.0 ± 1.3^c	6,7,8
ROXs 12 b	12-20	8^{+4}_{-3}	~ 210	-	S	N^d	-	7,9
CHXR 73 B	13^{+8}_{-6}	~ 2	~ 210	$\geq M9.5$	S	U	-	10,11
DH Tau B	12^{+10}_{-4}	$\sim 1-2$	~ 330	$M9.25 \pm 0.25$	S	Y	-9 to -11	9,12,13,14,30
GSC 6214-210 B	14 ± 2	~ 5	~ 320	$M9.5 \pm 1$	S	Y	-10.7 ± 1.3	5,6,15
CT Cha B	17 ± 6	0.9-3	440	-	S	Y	~ -9.22	16,32
WD 0806-661B	8 ± 2	1.5 ± 0.3	2500	Y	S	U	-	17,18
HD 106906 b	11 ± 2	13 ± 2	654 ± 3	$L2.5 \pm 1$	S	U	-	19, 2
Ross 458 C	11 ± 4.5	150-800	1168	$T8.5 \pm 0.5$	B	U	-	20,21,22,23,24,25
AB Pic B	13 ± 0.5	0.9-3	275	$L0 \pm 1$	S	U	-	26,27
SR 12 C	13 ± 7	~ 2	1083 ± 217	$L0 \pm 1$	B	Y	-11.08 ± 0.40	6,28,29
Oph 1622-2405	21 ± 3	11 ± 2	243 ± 55	$\geq L8$	S	U	-	2,33
U Sco CTIO 108 b	16^{+3}_{-2}	11 ± 2	~ 670	M9.5	S	U	-	2,34

Notes

Table based on Table 1 from [Bowler et al. \(2014\)](#) ^a Single ("S") or Binary ("B") ^b Yes("Yes"), No("N"), Unknown or non reported ("U") ^c [Bowler et al. \(2014\)](#) They also calculated $\log \dot{M} = 11.4 \pm 1.3 (M_{\odot} \text{yr}^{-1})$ depending on the calculation of the Mass. ^d [Kraus et al. \(2014\)](#) describes H α line weak as a WTTS, accretion was discarded. GSC 6214-210 B and FW TAU B accretion rate are based on Paschen β . In the case of DH TAU B the accretion rate is based on its optical excess emission. Accretion rate of CT Cha B measured from excess emission in r'.

References.

- (1) [Wu et al. \(2015b\)](#); (2) [Pecaut et al. \(2012\)](#); (3) [Lafrenière et al. \(2008\)](#); (4) [Lafrenière et al. \(2010\)](#); (5) [Ireland et al. \(2011\)](#); (6) [Bowler et al. \(2014\)](#); (7) [Kraus et al. \(2014\)](#); (8) [Caceres et al. \(2015\)](#); (9) [Bouvier & Appenzeller \(1992\)](#); (10) [Luhman \(2004\)](#); (11) [Luhman et al. \(2006\)](#); (12) [Itoh et al. \(2005\)](#); (13) [White & Ghez \(2001\)](#); (14) [Bonnefoy et al. \(2014\)](#); (15) [Bowler et al. \(2011\)](#); (16) [Schmidt et al. \(2008\)](#); (17) [Rodriguez et al. \(2011\)](#); (18) [Luhman et al. \(2011\)](#); (19) [Bailey et al. \(2014\)](#); (20) [Goldman et al. \(2010\)](#); (21) [Dupuy & Kraus \(2013\)](#); (22) [Scholz et al. \(2012\)](#); (23) [Burgasser et al. \(2010\)](#); (24) [Burningham et al. \(2011\)](#); (25) [Beuzit et al. \(2004\)](#); (26) [Chauvin et al. \(2005\)](#); (27) [Perryman et al. \(1997\)](#); (28) [Kuzuhara et al. \(2011\)](#); (29) this work; (30) [Zhou et al. \(2014\)](#); (31) [Neuhäuser et al. \(2005\)](#); (32) [Wu et al. \(2015a\)](#); (33) [Close et al. \(2007\)](#); (34) [Béjar et al. \(2008\)](#)

4.4.3 Accretion rate based on Paschen β

One of the regularly used accretion tracers in low-mass stars is Paschen β . [Natta et al. \(2004\)](#) found that the Pa β luminosity correlates with the accretion luminosity. We measured the Pa β luminosity in SR 12 C and obtained $\log(L_{\text{Pa}\beta}/L_{\odot}) = -7.16 \pm 2.25 L_{\odot}$. The empirical relation found by [Natta et al. \(2004\)](#) and revised by [Rigliaco et al. \(2012\)](#) is $\log L_{\text{acc}} = (1.49 \pm 0.04) \times \log L(\text{Pa}\beta) + 4.59 \pm 0.14$ which gives $L_{\text{acc}} = (-8.59 \pm 2.90) \times 10^{-7} L_{\odot}$ for SR 12 C. Assuming a mass of SR 12 C of $0.013 \pm 0.007 M_{\odot}$ ([Kuzuhara et al. 2011](#)) and a radius of $0.19 \pm 0.07 R_{\odot}$ (derived from the gravity values we obtained by spectral fitting) finally results in a mass accretion rate of $\dot{M} = (4.02 \pm 2.95) \times 10^{-13} M_{\odot} \text{yr}^{-1}$.

4.4.4 Accretion rate based on the OI line

Additional emission lines that can be related to accretion are those from OI (e.g. [Joergens et al. 2012a](#)). Our X-shooter spectrum contains a strong OI $\lambda 8446$ emission line that we here use to add another measurement of the accretion rate in SR 12 C. First, we calculate the line luminosity in a similar fashion as in the previous subsection. We then use Fig. 10 from [Herczeg & Hillenbrand \(2008\)](#) to estimate the accretion luminosity of SR 12 C (note that the coefficients for the shown linear correlation are not

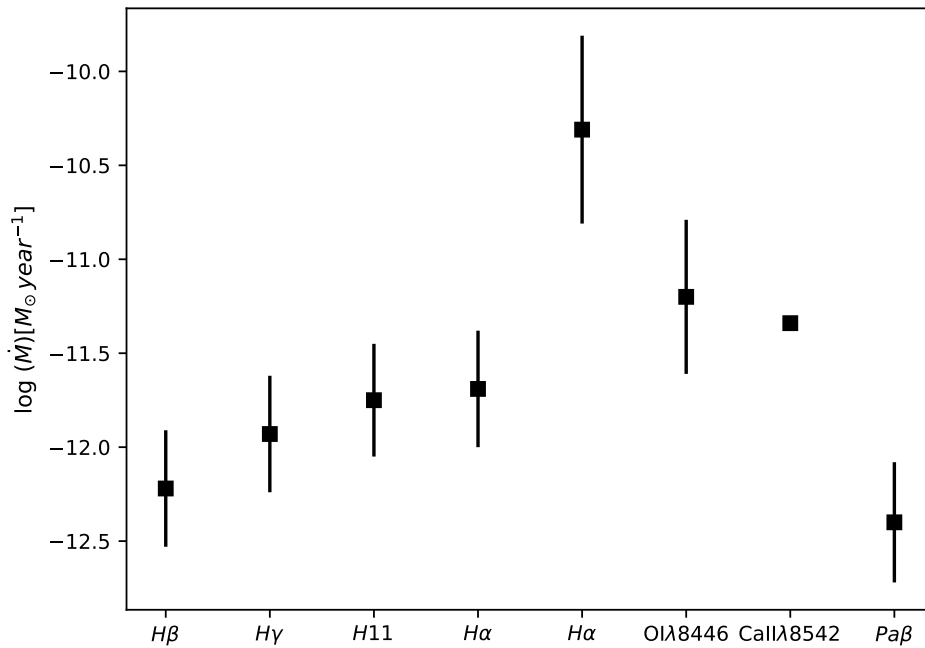


Figure 4.7: Accretion rates obtained from different emission lines. Apparently, the obtained values agree very with each other. The only exception is the accretion derived from H α which is significantly higher.

given) and finally obtain an accretion rate of $\dot{M} = (6.28 \pm 5.88) \times 10^{-12} M_{\odot} \text{ yr}^{-1}$ using the mass and radius of SR 12 C as above. The given uncertainty does not take into account the standard deviation of the linear fit from [Herczeg & Hillenbrand \(2008\)](#) as these values are not available to us. However, the included uncertainties related to the mass and radius of SR 12 C likely dominate the error estimate.

4.4.5 Accretion rates derived from other Hydrogen lines

The entire Balmer and Paschen emission line series has been used to measure accretion ([Ferguson 1997](#)). We used $\log(L_{\text{acc}}/L_{\odot}) = b + a \times \log(L_{\text{line}}/L_{\odot})$ to relate the accretion luminosity and the luminosities of the lines (see [Herczeg & Hillenbrand 2008](#); [Fang et al. 2009](#) and Table 6 and 8 from [Rigliaco et al. 2012](#)). We applied this method to the H α , H β , H γ and H11 lines identified in the spectrum of SR 12 C. Figure 4.6 shows the UV spectrum (bottom panel) of SR 12 C. Equivalent width, flux line (W m^{-2}), $\log(L_{\text{Pa}\beta}/L_{\odot})$ and accretion luminosity in solar units are given in Table 4.1. The resulting accretion rates can be found in Table 4.2.

4.5 Discussion

We have measured accretion rates for the SSC to the young binary SR 12 using eight different methods. In general, the measured accretion rates are similar and

agree with each other. However, the accretion rate measurement based on $H\alpha$ described in Section 4.4.1 is significantly higher than the other values we obtain, as illustrated in Fig. 4.7. The accretion rates obtained for SR 12 C is very similar to the values obtained for other SSCs. Accretion rate measurements exist for three other SSCs (CT Cha b, GSC 6214-210 B and FW Tau B). For GSC 6214-210 B and FW Tau B published accretion rate measurements are based on $Pa\beta$ emission and the obtained values are very similar to the one obtained for SR 12 C, i.e. -10.7 ± 1.3 and -11.0 ± 1.3 respectively. For CT Cha b Wu et al. (2015b) estimate a relatively high accretion rate of $\log \dot{M} (M_{\odot} \text{yr}^{-1}) = -9.22$ from interpreting excess emission in the r' -band as caused by $H\alpha$ emission. This is similar to the value we obtained for SR 12 C using $H\alpha$ (i.e. $\log \dot{M} (M_{\odot} \text{yr}^{-1}) \sim -10$). Thus one might get the impression that indeed be that $Pa\beta$ accretion rates of SSCs are systematically lower. However, Joergens et al. (2013) investigated accretion on the isolated brown dwarf OTS 44 and find that the rate derived from $Pa\beta$ is significantly *larger* than the one obtained from $H\alpha$. Thus, further simultaneous measurements of accretion rates based on different lines are needed before any firm conclusions can be drawn.

Nevertheless, we conclude that the values we obtain for SR 12 C with 8 different methods probably represent a more reliable estimate of the accretion rate in SR 12 C. The currently available accretion rate measurements for SSCs as listed in Table 4.3. In addition to the three objects mentioned above, two more objects have accretion rate estimates based on the accretion luminosity from excess continuum emission (Zhou et al. 2014).

In Fig. 4.8 we show accreting and non accreting systems as a function of age and mass. Objects in red are those that are accreting, objects in green have been reported as non-accreting in the literature, and the objects in blue lack accretion measurements. While more measurements are clearly needed before we can draw firm conclusions, this figure illustrates that SSCs younger than 10 Myr seem to be generally accreting. A similar tendency is observed in isolated brown dwarfs. For example, Liu et al. (2003) identify a decreasing disk fraction around low-mass objects and brown dwarfs supporting the idea that disks do usually not survive longer than 10 Myr. The potential similarity between isolated low-mass objects and SSCs is further supported by Figure 4.9 where we show the position of the SSCs with accretion measurements in the $\log \dot{M} - \log M$ diagram together with young isolated low-mass stars and brown dwarfs. SSCs seems to follow the usual correlation between mass and accretion rate (see also Bowler et al. 2014).

In summary, SSCs seem to share two accretion traits with young isolated brown dwarfs. These are their similar accretion rates, as well as the observation that both are accreting if they are younger than 10 Myrs. Although we are in an early stage concerning the understanding of these objects and only few observational constraints are available, the measured accretion rates might indicate that SSCs perhaps form in a similar way as isolated brown dwarfs. For example, if SSCs are originally formed close to the host star due to core accretion, one would expect the circumplanetary disks to be severely affected (see Bowler et al. 2011, for details) and would thus not expect the accretion on the companions to follow the same trend as observed in single low-mass objects. For the remaining two scenarios, disk fragmentation and

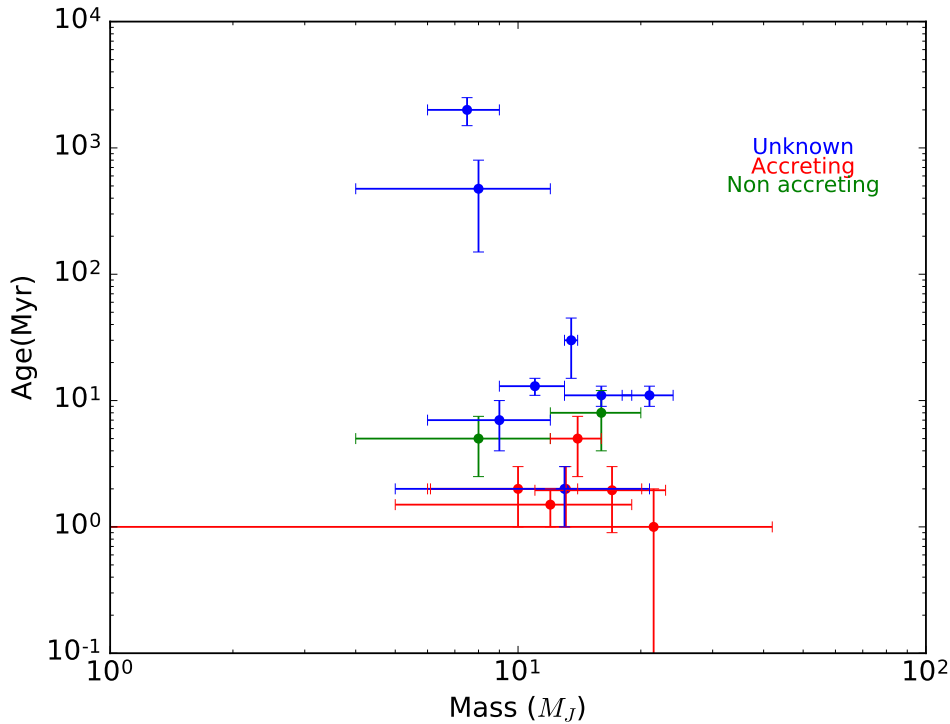


Figure 4.8: Age in Myr versus mass of the SSCs listed in 4.2. Red indicates that the objects are accreting, green represents non accreting objects and in blue we show SSCs without information on their accretion status. It seems that objects younger than 10 Myrs are usually accreting.

collapsing protostellar clouds, the predicted accretion rates are quite similar (Stamatellos & Herczeg 2015). The currently available measurements accretion rates of SSCs do not allow to distinguish between the two scenarios although the larger accretion rates predicted by disk fragmentation model fit as well as the formation of its own molecular cloud. However, if radiation feedback is included disk fragmentation has general problems in producing planetary mass companions at large separations (Mercer & Stamatellos 2017). The least problematic formation scenario therefore seems to be collapsing prestellar clouds, i.e. SSCs represent just the low-mass end of companions in multiple stellar systems.

4.6 Conclusion

SR 12 C is a substellar companion orbiting the binary system SR 12 AB at a projected separation of 1083 ± 217 in the ρ Ophiuchus star forming cloud. We observed SR 12 C using X-Shooter and fitted the resulting spectrum with a set of theoretical templates and two different sets of observational templates and find that SR 12 C is best described as brown dwarf with surface gravity $\log g = 4$, a temperature of 2600 K and that its spectral type is L0. These results agree well with previous studies of the object.

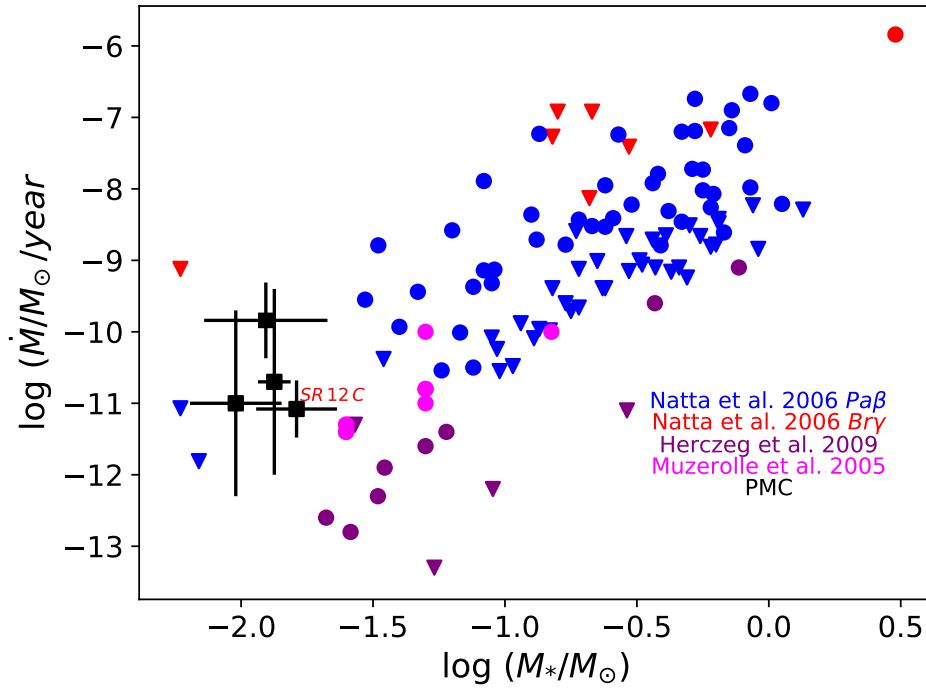


Figure 4.9: Based on Fig. 6 from [Bowler et al. \(2011\)](#). Mass accretion rates vs stellar mass. Triangles shows upper limits. We include FW TAU b, GSC 06214-00210 b, CT Cha B and SR 12 C as black squares. Data shown in blue are accretion rates given in [Natta et al. \(2006\)](#), which are measured using $Pa\beta$ while those in red are measured with $Br\gamma$. Purple symbols represent measurements from [Herczeg et al. \(2009\)](#) and pink circles have been obtained from [Muzerolle et al. \(2005\)](#). We selected only class II objects from [Natta et al. \(2006\)](#). Keep in mind that this plot combines accretion rate measurements with different methodologies of objects with different ages. However, it seem that SSCs roughly follow the correlation between mass and accretion rate of young stellar objects.

Investigating several accretion indicators we find that our X-shooter spectrum provides clear evidence for ongoing accretion in SR 12 C. We estimated the accretion rate using different emission lines and different methods and find that the obtained values cluster around $\sim 10^{-11}M_{\odot}/\text{yr}$.

Comparing the accretion rate measured for SR 12 C with those obtained for other SSCs and young isolated brown dwarfs we do not find indications for any significant differences. Indeed, it seems that most SSCs accrete if they are younger than ~ 10 Myrs and with similar rates as young isolated low-mass objects. While further observations of SSCs are clearly needed, this might perhaps indicate that the formation mechanism for isolated brown dwarfs and low-mass stars also produces substellar companions.

Chapter 5

General conclusions and future work

5.1 General conclusions

In this thesis we have covered all the stages (from pre-substellar cores to Class II sources) of the formation of very low-mass objects with the main goal of revealing which formation mechanisms is the dominant one. Most of the work is based on interferometric observations and optical spectroscopy.

In the second chapter we presented our interferometric survey with ALMA in the (sub)mm regime in the Lupus 1 and 3 molecular clouds based on a previous single dish survey with AzTEC/ASTE. We obtained a detection rate of 23.4 %, and most of the detected sources are located in the main filament and all of them are Very Low Luminosity Objects (VeLLOs).

We find eleven pre-substellar cores, that have no optical or infrared counterparts, with masses between 0.50 and 5.43 M_{Jup} . After studying their energetic status and the density profile, it seems that we detected with ALMA very low-mass objects at the very early stages of their formation, i.e. at the beginning of a large scale collapse. Two protosubstellar candidates were found, one of them with several counterparts in the optical/NIR. This source has a very complete SED, similar to other proto-BD candidates. We detected the disks of five Class II BDs. These disk are not resolved, thus we cannot compare our sources with the size predictions of the different formation theories. However, we were able to measure the dust disk masses that cover a range from 0.42 to 3.42 M_{\oplus} . According to the predictions of planet formation theories, it would be impossible to form planets in a disk containing that little mass. We can not exclude, however, that planets have formed earlier. We compared our ALMA Class II disks in Lupus with ALMA Class II disks in ρ Oph, Upper Scorpius, Taurus and Chameleon I, and we conclude that one of five disks could have formed by disk fragmentation. However, the whole sample seems to follow the scaling relation between disk mass and the mass of the central objects obtained from the stellar regime. The AzTEC cores in which we have ALMA detections have a mass between 11 to 180 M_{Jup} and sizes between ~ 3000 to ~ 7000 au without any specific trend in size or mass. The AzTEC cores without ALMA detection seem to be transient cores.

In the third chapter we detected for the first time the base of a molecular bipolar outflow from a VLM star (Par-Lup3-4), which turned out to be the faintest molecular outflow in a VLM source. Furthermore, we detected three molecular lines (CO(3-2), CO(2-1) and $^{13}\text{CO}(3-2)$) in a VLM source detected so far.

The spectral index of the continuum emission is compatible with grain growth, as

previous studies at optical wavelengths indicated, but it is also compatible with a compact disk, probably related to a high disk inclination. We detected a secondary moving structure whose nature is still uncertain. This structure is perpendicular to the molecular bipolar outflow. We proposed four scenarios to explain this feature:

- A second monopolar outflow originating from a close binary
- Cloud contamination
- An outflow originating from a visual binary
- Emission coincident with H α emission detected several years ago whose origin could be a young stellar object or BD companion.

With the data at hand today, we are unable to discriminate between these possibilities. SED fitting showed that the radius is twice the expected value for this source. This can only be explained if the object is younger than previously thought or due to the presence of a binary that would also explain the presence of the moving structure.

We characterized the bipolar molecular outflow with an average size of ~ 295 au, a velocity of 6 km/s and an average opening angle of 112° . We derived an outflow mass $\sim 6 \times 10^{-6} M_\odot$ and other dynamical parameters such as the dynamical time and the outflow mass rate. All parameters derived for the outflow observed in Par-Lup3-4 are consistent with it being a scaled down version of more massive forming objects. This finding is in agreement with previous studies of outflows of VLM sources. We do not see any difference in the outflow properties of BDs and VLM stars.

The fourth chapter is focused on the study of the substellar companion SR 12 C. It is orbiting at separation of 1083 au around a stellar binary system. This separation was crucial to obtain a pure spectrum of the BD using X-Shooter. The spectrum covers emission from near-ultraviolet to near-infrared. We fit the source using theoretical templates and find it to be a young source with an effective temperature of 2600 K and log gravity of 4. Then we fit the spectrum using observational templates obtaining that the source has a spectral type of L0. The radial velocity between the binary system and the companion is the same discarding the possibility of ejection. It is more likely that the object formed in situ. We constrained the accretion rate to be $10^{-11} M_\odot/\text{yr}$ using the same accretion indicators typically used for young stellar objects. The accretion rate is similar to previous studies based on only one accretion indicator. The accretion rate compared with the mass of the source seems to be an extension of the trend that is found for young stellar objects. Current predictions that include radiative feedback showed that BDs formed by disk fragmentation at high separation are probably ejected, which did apparently not happen in the case of SR 12 C. We conclude that it is more likely that the source is formed in situ from its own parental cloud. Finally, we remark that Chapter 4 presented the first work using several accretion indicators for a forming BD companion.

The fact that the outflow properties of VLM sources are a downsized version of the ones observed in low-mass stars; the fact that the accretion rate of BDs, even as a companion of stars, is consistent with the relation obtained for low-mass stars between accretion rate and mass of the accreting object; the fact that we identify several pre-substellar candidates that are in contraction and isolated, leads us to the conclusion that the main formation mechanism of BDs is the scaled-down version of low-mass star formation, i.e. the main formation mechanism is most likely turbulent fragmentation.

5.2 Future work

The results of this thesis provide clues about the main formation mechanism of BDs, at the same time that the study of BD disks with ALMA is opening new questions in this framework. My future research will be an extension of my work, presented in this thesis, opening new lines of research related to planet formation in BDs. The next paragraph is a brief description of my future projects.

All the candidates presented in Chapter 2 need to be confirmed through the detection of gas at a velocity near the V_{LSR} , in order to confirm their galactic nature. Medium scale observations with ALMA are also needed to constrain the envelope sizes. We recently received new ALMA data in two different wavelengths, and their study can be crucial to confirm these sources. We plan to study spectral indexes between both new bands. Finding dust grains from millimeter to centimeter sizes will favour the disk fragmentation and ejection scenario. The absence of processed dust would support the scaled-down version of low-mass stars as a formation scenario.

I plan to replicate the study performed in Lupus in other star forming regions such as ρ Ophiuchus to extend the number of pre-and proto-BDs as well as to check if there is any difference in size or percentage between different SFR. [Testi et al. \(2016b\)](#) showed how disks in Ophiuchus and Taurus have very different structures, with the ρ Ophiuchus BD disks being smaller and truncated compared to those in Taurus. [Testi et al. \(2016b\)](#) speculated that differences in the cloud environment between ρ Ophiuchus and Taurus might be the reason for this result.

I plan to follow up the study on Par-Lup3-4 using higher angular resolution to detect a possible close binary and to reveal the nature of the moving structure we detected. I also plan to extend the sample of VLM outflows detections with ALMA and study their properties in order to better understand the ejection mechanism, as well as to gain further insights into BD formation.

Finally, I plan to study possible planet formation in BD. For this ambitious goal, I will need higher spatial resolution and higher sensitivity observations in order to find the same structures that are found in protoplanetary disks including narrow gaps ([ALMA Partnership et al. 2015](#); [Andrews et al. 2016](#)), the water snow line ([Cieza et al. 2016](#)) or dust rings ([Canovas et al. 2016](#)). Grain growth studies and the comparison of the amount of dust in their disks are also interesting for our understanding of possible planet formation around substellar objects.

Appendix A

Lupus 1 and 3 survey: ALMA detections and non detections

Name ¹	Ra(J2000) [h m s]	Dec(J2000) ² [° ' '']	rms ³ (Jy/beam) × 10 ⁻⁴	Classification ⁴	References ⁵
153701.1-332	15:37:01.10	-33:22:55.00	1.04	Class II	1
ALMA J153702.653-331924.92 ⁶	15:37:03.10	-33:19:27.00	0.96	Class II	
153709.9-330	15:37:09.90	-33:01:29.00	0.85	Class II	1
AzTEC-lup1-99	15:38:04.40	-34:52:28.24	0.54	Starless core	
AzTEC-lup1-103	15:38:12.90	-34:56:23.70	0.56	Starless core	
AzTEC-lup1-109	15:38:27.44	-35:12:40.90	0.57	Starless core	
AzTEC-lup1-72	15:38:46.93	-33:23:36.38	0.92	Class I	
AzTEC-lup1-111	15:38:59.73	-33:29:50.16	0.55	Starless core	
AzTEC-lup1-57	15:39:04.25	-35:06:43.0	0.69	Starless core	
ALMA J153914.996-332907.62 ⁶	15:39:15.84	-33:28:58.50	0.94	Starless core	
153921.8-340	15:39:21.80	-34:00:20.00	0.85	Class II	1
AzTEC-lup1-67	15:39:21.17	-34:43:37.52	0.71	Starless core	
AzTEC-lup1-114	15:39:49.35	-34:49:26.22	0.63	Starless core	
AzTEC-lup1-84	15:40:09.15	-33:32:20.16	0.57	Starless core	
AzTEC lup1-90	15:40:18.86	-33:41:00.09	0.61	Class 0	
AzTEC-lup1-40	15:40:46.65	-33:43:17.88	1.01	Class I	
AzTEC-lup1-104	15:41:15.39	-33:46:41.34	0.57	Starless core	
AzTEC-lup1-101	15:41:28.04	-33:41:51.37	0.59	Starless core	
154140.8-334	15:41:40.80	-33:45:19.00	0.89	Class II	1,2
AzTEC-lup1-119	15:42:05.21	-33:45:59.71	0.58	Starless core	
ALMA J154228.675-334230.18 ⁶	15:42:29.56	-33:42:39.94	1.44	Class 0	
ALMA J154229.778-334231.86 ⁶	15:42:29.56	-33:42:39.94	1.06	Class 0	
AzTEC-lup1-124	15:42:38.60	-33:48:52.24	0.55	Starless core	
AzTEC-lup1-52	15:42:45.21	-33:58:43.41	0.65	Starless core	
AzTEC-lup1-54	15:42:45.02	-34:12:01.36	0.75	Starless core	
AzTEC-lup1-94	15:43:50.32	-34:01:59.60	0.67	Starless core	
154433.9-335254	15:44:33.90	-33:52:54.00	1.08	Class II	1
ALMA J154456.522-342532.99 ⁶	15:44:57.22	-34:25:31.55	0.68	Starless core	
ALMA J154458.061-342528.51 ⁶	15:44:57.22	-34:25:31.55	0.97	Starless core	
AzTEC-lup1-71	15:44:59.34	-34:20:55.49	0.91	Class 0	
ALMA J154506.515-344326.15 ⁶	15:45:06.45	-34:43:16.23	0.52	Starless core	
AzTEC-lup1-123	15:45:40.24	-35:04:56.61	0.62	Starless core	
ALMA J154634.169-343301.90 ⁶	15:46:33.47	-34:33:05.10	0.83	Starless core	
160545.8-385	16:05:45.80	-38:54:54.00	0.62	Class II	1
160658.7-390405 ⁶	16:06:58.70	-39:04:05.00	0.62	Class II	1
AzTEC-lup-3-15	16:07:51.70	-39:07:29.50	0.58	Starless core	
160714.0-385	16:07:14.00	-38:52:38.00	0.60	Class II	1,2
ALMA J160804.168-390452.84 ⁶	16:08:04.80	-39:04:49.00	0.93	Class II	
AzTEC-lup-3-20	16:08:14.40	-39:10:50.89	0.67	Starless core	

¹Name as appear in the literature. AzTEC-lup is a denomination for the non ALMA detection pointings based on AzTEC detections.

²Phase center of the observation

³rms is measured at the phase center, except for the ALMA detected sources

⁴Previous classification before the ALMA observation based on AzTEC data and optical/infrared counterparts.

⁵Specific references used to obtain spectroscopically confirmed Class II sources in the ALMA pointing: (1) [Comerón et al. \(2009\)](#), (2) [Merín et al. \(2008\)](#), (3) [Mužić et al. \(2014\)](#)

⁶Sources detected. See table 2.2

160816.0-39	16:08:16.00	-39:03:04.00	0.57	Class II	1,2,3
160826.8-384101 ⁶	16:08:26.80	-38:41:01.00	0.59	Class II	1
LABOCA-lup3-12	16:08:32.70	-39:04:39.80	0.61	Starless core	
160833.1-385	16:08:33.05	-38:52:22.40	0.66	Class II	1,3
160835.5-390	16:08:35.48	-39:00:35.80	0.67	Class II	1,3
Lup-706 ⁶	16:08:37.33	-39:23:10.90	0.90	Class II	1,3
LABOCA-lup3-10	16:08:41.60	-39:05:23.91	0.58	Starless core	
160848.2-39	16:08:48.20	-39:09:19.00	0.51	Class II	1,2,3
LABOCA-lup3-5	16:08:48.50	-39:07:27.97	0.66	Starless core	
Par-Lup3-4 ⁶	16:08:51.44	-39:05:30.50	0.52	Class I/II	1,2,3
AzTEC-lup-3-14	16:08:54.60	-39:12:26.90	0.52	Starless core	
AzTEC-lup-3-19	16:08:55.40	-39:05:59.89	0.60	Starless core	
SONYC-Lup3-7 ⁶	16:08:59.53	-38:56:27.80	0.55	Class I/II?	1,2,3
LABOCA-lup3-4	16:09:13.60	-39:07:43.95	0.59	Starless core	
SONYC-lup3-10	16:09:13.43	-38:58:04.90	0.62	Class I/II?	3
LABOCA-lup3-8	16:09:14.30	-39:05:23.95	0.65	Starless core	
LABOCA-lup3-13	16:09:36.60	-39:03:59.64	0.69	Starless core	
ALMA J160920.089-384515.92 ⁶	16:09:20.80	-38:45:10.00	0.78	Class II	
ALMA J160920.171-384456.40 ⁶	16:09:20.80	-38:45:10.00	1.75	Class II	
ALMA J160932.167-390832.27 ⁶	16:09:32.80	-39:08:44.11	1.28	Starless core	
SONYC-lup3-29	16:10:01.33	-39:06:45.10	0.57	Class II	1,2
LABOCA-lup3-9	16:10:05.90	-39:10:54.84	0.61	Starless core	
AzTEC-lup-3-21	16:10:08.22	-39:02:51.68	0.53	Class I	
AzTEC-lup-3-16	16:10:19.80	-39:11:51.07	0.67	Starless core	
ALMA J161030.273-383154.52 ⁶	16:10:30.60	-38:31:51.00	0.64	Class II	
161144.9-383234	16:11:44.88	-38:32:44.90	0.59	Class II	1,2,3
161225.6-381742	16:12:25.60	-38:17:42.00	0.56	Class II	1,3
161210.4-390904	16:12:10.46	-39:09:04.00	0.51	Class II	1,3

Table A.1: List of the ALMA pointings based on the AzTEC detections. The position and the rms are measured in the phase center. We included the previous classification based on the AzTEC detections and the SED from the SOLA catalog. Class II and some Class I/II sources were obtained from the literature

Appendix B

Flux and wavelength for each source in the Lupus sample

The following table present the fluxes and wavelength used to build the SED for each source detected with ALMA

Wavelength [μm]	Flux [mJy]		
ALMA J153702.653-331924.92			
70	≤ 25.61		
160	≤ 37.7		
250	≤ 135		
350	≤ 123		
500	≤ 122		
1100	111 ± 0.011		
1330	0.45 ± 0.10		
ALMA J153914.996-332907.62			
0.64	0.0013 ± 0.0003		
0.80	0.0071 ± 0.0013		
0.96	0.0165 ± 0.0027		
70	≤ 26.0		
100	≤ 32.1		
160	≤ 47.4		
250	≤ 1100		
350	≤ 1266		
500	≤ 820		
1100	40 ± 4		
1330.8	0.73 ± 0.09		
ALMA J154228.675-334230.18			
70	≤ 23.0		
100	≤ 33.5		
160	≤ 35.8		
250	≤ 110		
350	≤ 180		
500	≤ 114		
1100	25 ± 3		
1330	2.84 ± 0.14		
ALMA J154229.778-334341.86			
0.64	0.0010 ± 0.0002	-	
0.80	0.0049 ± 0.0011	-	
0.96	0.013 ± 0.003	-	
3.4	0.092 ± 0.007	0.4	
4.6	0.142 ± 0.013	0.4	
4.5	0.14 ± 0.01	0.1	
8	0.13 ± 0.04	0.1	
22	≤ 4.7	0.4	
23.67	1.41 ± 0.28	0.1	
70	≤ 21.3	2.9	
100	≤ 34.4	-	
160	≤ 38.0	2.9	
250	82 ± 15.3	2.9	
350	106.4 ± 21.2	2.9	
500	79.1 ± 15.9	2.9	
1100	38 ± 4	3.3	
1330	4.1 ± 0.1		

ALMA J154456.522-342532.99		ALMA J160804.168-390452.84	
70	≤ 5.4	0.79	≤ 0.02
100	≤ 27.4	1.23	≤ 0.08
160	≤ 27.5	2.16	≤ 0.06
250	≤ 2950	70	≤ 26.5
350	≤ 1570	100	≤ 36.1
500	≤ 1080	160	≤ 46.3
1100	46 ± 5	250	≤ 378
1330	2.50 ± 0.07	350	≤ 338
ALMA J154458.061-342528.51		500	≤ 324
70	≤ 6.0	868.96	≤ 30
100	≤ 33.2	1330	0.87 ± 0.09
160	≤ 39.80	160826.8-384101	
250	≤ 1070	0.64	0.250 ± 0.004
350	≤ 1520	0.80	1.30 ± 0.02
500	≤ 920	0.96	2.88 ± 0.04
1100	$\leq 46 \pm 5$	0.82	1.48 ± 0.07
1330	1.42 ± 0.01	1.25	5.65 ± 0.47
ALMA J154506.515-344326.15		1.23	6.95 ± 0.15
70	≤ 23.3	1.66	8.06 ± 0.19
100	≤ 31.7	2.15	7.59 ± 0.70
160	≤ 37.9	2.16	7.04 ± 0.19
250	≤ 240	3.4	5.04 ± 0.11
350	≤ 310	3.6	6.19 ± 0.43
500	≤ 260	4.6	4.50 ± 0.09
1100	48 ± 5	5.8	4.9 ± 0.27
1330	0.26 ± 0.09	12	3.11 ± 0.19
ALMA J154634.169-343301.90		22	2.67 ± 1.11
70	≤ 25.9	23.67	2.62 ± 0.33
100	≤ 29.6	70	≤ 26
160	≤ 40.7	160	≤ 43.53
250	≤ 1750	1100	≤ 194
350	≤ 2110	1330	1.57 ± 0.06
500	≤ 1990	V1094Sco	
1100	170 ± 17	0.64	8.97 ± 0.025
1330	0.75 ± 0.08	0.80	46.50 ± 0.128
160658.7-390405		0.96	82.91 ± 0.153
0.65	0.29	0.82	81.99 ± 2.27
0.77	1.99	1.25	193 ± 8.88
0.96	4.32	2.15	259.4 ± 11.9
1.25	10.5	1.23	177 ± 4.25
1.65	12	1.66	247 ± 5.24
2.15	10.6	2.16	229 ± 4.44
70	≤ 26.91	3.4	229.77 ± 4.87
100	≤ 35.5	4.6	280.38 ± 3.32
160	≤ 29.84	12	96.09 ± 1.41
250	≤ 116	22	112.5 ± 3.2
350	≤ 91	3.6	153 ± 10.1
500	≤ 63		
1330	0.48 ± 0.06		

4.5	138 ± 7.48		
5.8	132 ± 6.31	1.66	2.02 ± 0.07
8	132 ± 6.41	2.15	2.45 ± 0.43
9	155.9 ± 24.2	2.16	3.18 ± 0.12
23.675	113 ± 10.4	3.4	3.09 ± 0.07
71.42	462 ± 80	4.6	3.43 ± 0.07
70	448.0 ± 39.8	3.6	2.80 ± 0.15
100	766.3 ± 9.5	4.5	2.88 ± 0.15
160	1364.9 ± 42.4	5.8	2.24 ± 0.13
250	2164 ± 429	8	1.730 ± 0.105
350	2467 ± 493	12	≤ 4.22
600	1989 ± 398	23.67	26.6 ± 2.6
868	438.3 ± 8.6	70	59.7 ± 3.0
1100	218 ± 6	100	≤ 35.41
1330	244.05 ± 0.22	160	≤ 86.1
Lup706		250	≤ 1215
0.64	0.016 ± 0.001	350	≤ 1455
0.80	0.102 ± 0.005	500	≤ 1102
0.96	0.42 ± 0.01	868	≤ 13.5
0.82	0.10 ± 0.02	1100	≤ 357.61
1.25	1.68 ± 0.20	1330	0.31 ± 0.05
1.23	1.36 ± 0.07	SONYC-lup3-7	
2.15	2.74 ± 0.45	0.64	0.06 ± 0.03
1.66	2.06 ± 0.09	0.80	0.42 ± 0.01
2.16	1.96 ± 0.08	0.96	1.19 ± 0.02
3.6	2.18 ± 0.11	1.23	4.38 ± 0.12
4.5	1.08 ± 0.11	1.66	4.93 ± 0.14
5.8	1.77 ± 0.11	2.16	4.90 ± 0.14
8	1.940 ± 0.108	3.4	3.49 ± 0.08
23.67	1.62 ± 0.34	4.6	3.55 ± 0.07
71.42	≤ 50	3.6	3.89 ± 0.21
70	≤ 21.1	4.5	3.69 ± 0.19
100	≤ 33.3	5.8	3.77 ± 0.23
160	≤ 58.4	8	4.31 ± 0.21
250	≤ 1905	12	4.31 ± 0.20
350	≤ 2427	22	8.24 ± 1.22
500	≤ 1983	23.67	5.4 ± 0.6
1100	318 ± 32	70	9.5 ± 0.7
1330	0.22 ± 0.09	100	≤ 29.4
Par-lup3-4		160	≤ 10.5
0.64	0.08 ± 0.04	868	≤ 24
0.80	0.13 ± 0.01	1330	0.32 ± 0.06
0.96	0.16 ± 0.01	ALMA J160920.089-384515.92	
0.55	0.007 ± 0.002	0.64	0.0229 ± 0.001
0.65	0.038 ± 0.005	0.79	0.047 ± 0.005
0.80	0.13 ± 0.01	0.80	0.041 ± 0.003
1.23	1.04 ± 0.06		
1.25	0.61 ± 0.12		

0.96	0.047 ± 0.005
1.23	0.121 ± 0.012
2.16	0.10 ± 0.01
70	≤ 23.6
100	≤ 50.2
160	≤ 41.1
350	≤ 22.70
500	≤ 15.62
1330	0.90 ± 0.08

ALMA J160920.171-384456.40

1.23	8.37 ± 0.18
1.66	9.91 ± 0.21
2.16	7.74 ± 0.16
3.4	4.18 ± 0.09
4.6	2.19 ± 0.05
12	≤ 0.48
22	≤ 2.35
70	≤ 27.1
100	≤ 69.7
160	≤ 45.6
1330	0.91 ± 0.18

ALMA J160932.167-390832.27

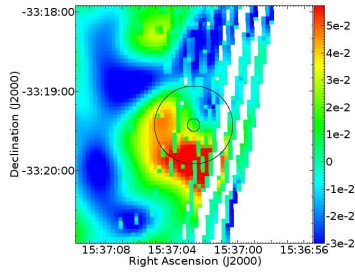
0.79	≤ 0.02
1.23	≤ 0.08
2.16	≤ 0.06
70	≤ 28.29
100	≤ 31.3
160	≤ 34.41
250	≤ 1180
350	≤ 1572
500	≤ 1119
1100	89 ± 9
1330	0.62 ± 0.13

ALMA J161030.273-383154.52

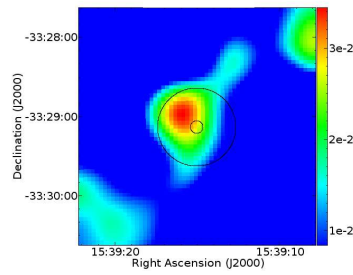
0.79	≤ 0.024
1.23	≤ 0.076
2.16	≤ 0.061
70	≤ 30.22
160	≤ 40.3
1330	0.70 ± 0.06

Appendix C
AzTEC images of the Lupus sample

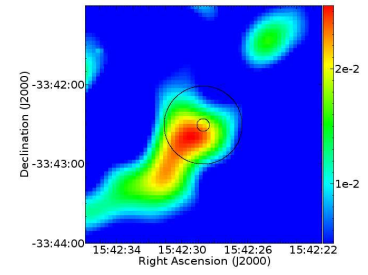
ALMA J153702.653-331924.92



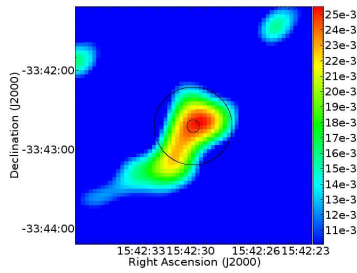
ALMA J153914.996-332907.62



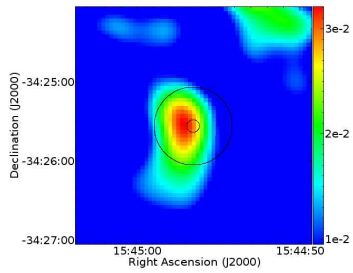
ALMA J154228.675-334230.18



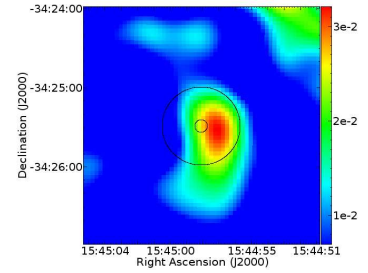
ALMA J154229.778-334231.86



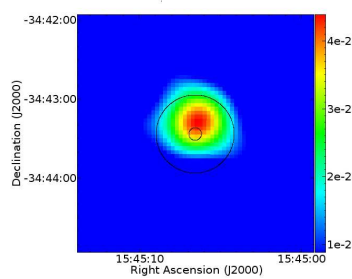
ALMA J154456.522-342532.99



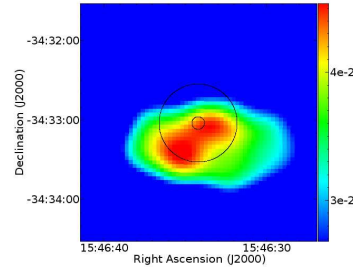
ALMA J54458.061-342528.41



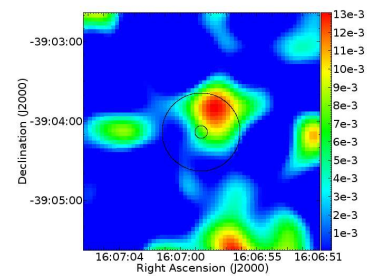
ALMA J154506.515-344326.15



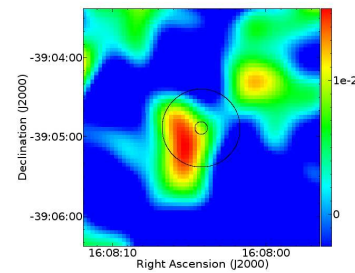
ALMA J154634.169-343301.90



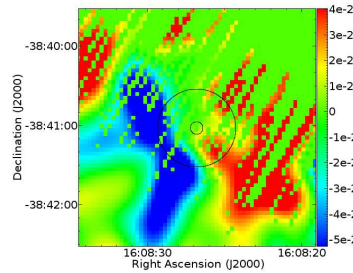
160658.7-390405



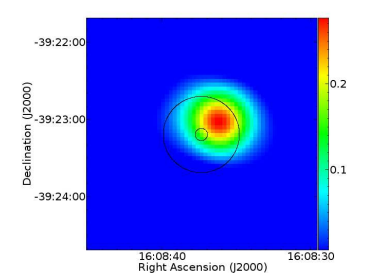
ALMA J160804.168-390452.84



160826.8-384101



Lup706



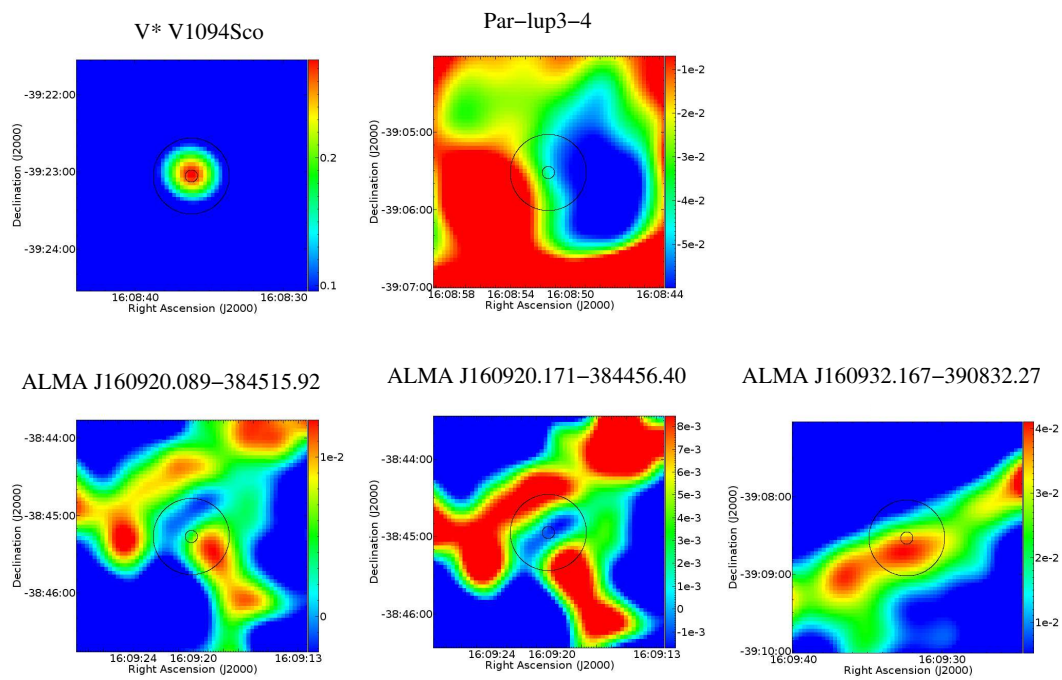


Figure C.1: AzTEC maps at 1.1 mm centered at the position of the ALMA detections. The position is in RA vs DEC (J2000). The wedge color bar at the right shows the flux (mJy/ per beam). Smaller circle represent radius 5 arcsec and the greater circle represent 30 arcsec. SONYC lup3-7 and 161030.6-383151 have no images

Appendix D

Equivalent width of photospheric features in SR 12 C

We identified the several absorption features common in late M and early L stars. The lines and the equivalent width are given in the table below.

Line	Wavelength (Å)	Equivalent Width (Å)
TiO	7053	0.83 ± 0.04
VO	7424	0.14 ± 0.01
TiO	7589	0.59 ± 0.01
K I	7697	0.47 ± 0.07
TiO	8204	0.62 ± 0.01
TiO	8433	0.72 ± 0.03
FeH	9901	0.82 ± 0.27
VO	9586	0.21 ± 0.01
CsI	8935	1.33 ± 0.09
VO	10604	0.31 ± 0.01
K I	11690	1.41 ± 0.16
K I	12432	1.26 ± 0.02
VO	11975	0.37 ± 0.01
K I	12520	1.78 ± 0.05
Ca I	13113	2.08 ± 0.01
K I	15167	1.81 ± 0.13
Fe I	17181	0.28 ± 0.01
CO	22934	2.10 ± 0.06
CO	23225	1.02 ± 0.06
CO	23516	0.86 ± 0.06

Bibliography

- Alcalá, J. M., Manara, C. F., Natta, A., et al. 2017, *A&A*, 600, A20
- Alcalá, J. M., Natta, A., Manara, C. F., et al. 2014, *A&A*, 561, A2
- Allard, F. 2014, in *IAU Symposium, Vol. 299, Exploring the Formation and Evolution of Planetary Systems*, ed. M. Booth, B. C. Matthews, & J. R. Graham, 271–272
- Allard, F., Hauschildt, P. H., Alexander, D. R., & Starrfield, S. 1997, *ARA&A*, 35, 137
- Allard, F., Homeier, D., & Freytag, B. 2012, *Royal Society of London Philosophical Transactions Series A*, 370, 2765
- ALMA Partnership, Brogan, C. L., Pérez, L. M., et al. 2015, *The Astrophysical Journal*, 808, L3
- Alves de Oliveira, C., Moraux, E., Bouvier, J., & Bouy, H. 2012, *A&A*, 539, A151
- Alves de Oliveira, C., Moraux, E., Bouvier, J., et al. 2010, *Astronomy and Astrophysics*, 515, A75
- Andre, P. & Montmerle, T. 1994, *ApJ*, 420, 837
- André, P., Motte, F., & Bacmann, A. 1999, *ApJ*, 513, L57
- Andre, P., Ward-Thompson, D., & Barsony, M. 2000, in *Protostars and Planets IV*, ed. V. Mannings, A. P. Boss, & S. S. Russell, 59
- André, P., Ward-Thompson, D., & Greaves, J. 2012, *Science*, 337, 69
- Andrews, S. M., Huang, J., Pérez, L. M., et al. 2018, *The Astrophysical Journal*, 869, L41
- Andrews, S. M., Rosenfeld, K. A., Kraus, A. L., & Wilner, D. J. 2013, *The Astrophysical Journal*, 771, 129
- Andrews, S. M., Wilner, D. J., Zhu, Z., et al. 2016, *The Astrophysical Journal*, 820, L40
- Ansdell, M., Williams, J. P., Trapman, L., et al. 2018, *ApJ*, 859, 21
- Ansdell, M., Williams, J. P., van der Marel, N., et al. 2016, *ApJ*, 828, 46
- Apai, D., Pascucci, I., Sterzik, M. F., et al. 2004, *A&A*, 426, L53
- Arce, H. G. & Sargent, A. I. 2006, *ApJ*, 646, 1070
- Arce, H. G., Shepherd, D., Gueth, F., et al. 2007a, in *Protostars and Planets V*, ed. B. Reipurth, D. Jewitt, & K. Keil, 245
- Arce, H. G., Shepherd, D., Gueth, F., et al. 2007b, *Protostars and Planets V*, 245
- Baade, D., Meisenheimer, K., Iwert, O., et al. 1999, *The Messenger*, 95, 15
- Bacciotti, F., Whelan, E. T., Alcalá, J. M., et al. 2011, *ApJ*, 737, L26

- Bailer-Jones, C. A. L. 2015, *PASP*, 127, 994
- Bailey, V., Meshkat, T., Reiter, M., et al. 2014, *ApJ*, 780, L4
- Bally, J. 2016, *ARA&A*, 54, 491
- Baraffe, I., Homeier, D., Allard, F., & Chabrier, G. 2015, *A&A*, 577, A42
- Barnard, E. 1927, Univ. of Chicago Press
- Barrado, D., de Gregorio Monsalvo, I., Huéramo, N., et al. 2018, *A&A*, 612, A79
- Barrado, D., Morales-Calderón, M., Palau, A., et al. 2009, *A&A*, 508, 859
- Barrado y Navascués, D., Stauffer, J. R., Bouvier, J., Jayawardhana, R., & Cuillandre, J.-C. 2004, *ApJ*, 610, 1064
- Basri, G., Marcy, G. W., & Graham, J. R. 1995, in *Bulletin of the American Astronomical Society*, Vol. 27, American Astronomical Society Meeting Abstracts #186, 1214
- Basu, S. & Vorobyov, E. I. 2012, *ApJ*, 750, 30
- Bate, M. R. & Bonnell, I. A. 2005, *MNRAS*, 356, 1201
- Bate, M. R., Bonnell, I. A., & Bromm, V. 2002, *MNRAS*, 332, L65
- Bate, M. R., Bonnell, I. A., & Bromm, V. 2003, *MNRAS*, 339, 577
- Bayo, A., Barrado, D., Allard, F., et al. 2017, *MNRAS*, 465, 760
- Bayo, A., Barrado, D., Stauffer, J., et al. 2011, *A&A*, 536, A63
- Béjar, V. J. S., Zapatero Osorio, M. R., Pérez-Garrido, A., et al. 2008, *ApJ*, 673, L185
- Beuzit, J.-L., Ségransan, D., Forveille, T., et al. 2004, *A&A*, 425, 997
- Bonnefoy, M., Chauvin, G., Lagrange, A.-M., et al. 2014, *A&A*, 562, A127
- Bonnell, I. A., Bate, M. R., Clarke, C. J., & Pringle, J. E. 1997, *MNRAS*, 285, 201
- Bonnor, W. B. 1956, *MNRAS*, 116, 351
- Bontemps, S., Andre, P., Terebey, S., & Cabrit, S. 1996, *A&A*, 311, 858
- Boss, A. P. 1997, *Science*, 276, 1836
- Boss, A. P. 2011, *ApJ*, 731, 74
- Boss, A. P., Butler, R. P., Hubbard, W. B., et al. 2007, *Transactions of the International Astronomical Union, Series A*, 26, 183
- Bourke, T. L., Crapsi, A., Myers, P. C., et al. 2005, *ApJ*, 633, L129
- Bourke, T. L., Myers, P. C., Evans, II, N. J., et al. 2006, *ApJ*, 649, L37
- Bouvier, J. & Appenzeller, I. 1992, *Astronomy and Astrophysics, Supplement*, 92, 481
- Bouy, H., Huéramo, N., Martín, E. L., et al. 2007, *A&A*, 463, 641
- Bowler, B. P., Liu, M. C., Kraus, A. L., & Mann, A. W. 2014, *ApJ*, 784, 65
- Bowler, B. P., Liu, M. C., Kraus, A. L., Mann, A. W., & Ireland, M. J. 2011, *ApJ*, 743, 148

- Burgasser, A. J., Simcoe, R. A., Bochanski, J. J., et al. 2010, *ApJ*, 725, 1405
- Burningham, B., Leggett, S. K., Homeier, D., et al. 2011, *MNRAS*, 414, 3590
- Caballero, J. A., Béjar, V. J. S., Rebolo, R., et al. 2007, *A&A*, 470, 903
- Caceres, C., Hardy, A., Schreiber, M. R., et al. 2015, *ApJ*, 806, L22
- Cahill, E., Whelan, E. T., Huélamo, N., & Alcalá, J. 2019, *MNRAS*, 484, 4315
- Calvet, N. & Gullbring, E. 1998, *ApJ*, 509, 802
- Calvet, N., Hartmann, L., & Strom, S. E. 1997, *ApJ*, 481, 912
- Cambrésy, L. 1999, *A&A*, 345, 965
- Canovas, H., Caceres, C., Schreiber, M. R., et al. 2016, *Monthly Notices of the Royal Astronomical Society*, 458, L29
- Carpenter, J., Iono, D., Testi, L., et al. 2019, arXiv e-prints, arXiv:1902.02856
- Cha, S.-H. & Whitworth, A. P. 2003, *MNRAS*, 340, 91
- Chabrier, G., Baraffe, I., Allard, F., & Hauschildt, P. 2000, *ApJ*, 542, L119
- Chabrier, G., Baraffe, I., Allard, F., & Hauschildt, P. H. 2005, arXiv e-prints, astro
- Chauvin, G., Lagrange, A.-M., Zuckerman, B., et al. 2005, *A&A*, 438, L29
- Chen, H., Myers, P. C., Ladd, E. F., & Wood, D. O. S. 1995, *ApJ*, 445, 377
- Chen, X., Arce, H. G., Dunham, M. M., & Zhang, Q. 2012, *ApJ*, 747, L43
- Cieza, L. A., Casassus, S., Tobin, J., et al. 2016, *Nature*, 535, 258
- Cieza, L. A., Schreiber, M. R., Romero, G. A., et al. 2010, *ApJ*, 712, 925
- Cieza, L. A., Schreiber, M. R., Romero, G. A., et al. 2012, *ApJ*, 750, 157
- Close, L. M., Zuckerman, B., Song, I., et al. 2007, *ApJ*, 660, 1492
- Codella, C., Maury, A. J., Gueth, F., et al. 2014, *A&A*, 563, L3
- Comerón, F. 2008, *The Lupus Clouds* (Reipurth, B.), 295
- Comerón, F. & Fernández, M. 2011, *A&A*, 528, A99
- Comerón, F., Fernández, M., Baraffe, I., Neuhäuser, R., & Kaas, A. A. 2003, *A&A*, 406, 1001
- Comeron, F., Rieke, G. H., Claes, P., Torra, J., & Laureijs, R. J. 1998, *A&A*, 335, 522
- Comerón, F., Spezzi, L., & López Martí, B. 2009, *A&A*, 500, 1045
- Comeron, F., Spezzi, L., & Lopez Marti, B. 2009, *VizieR Online Data Catalog*, 350
- Cutri, R. M., Skrutskie, M. F., van Dyk, S., et al. 2003, *VizieR Online Data Catalog*, II/246
- de Geus, E. J., de Zeeuw, P. T., & Lub, J. 1989, *A&A*, 216, 44
- de Gregorio-Monsalvo, I., Barrado, D., Bouy, H., et al. 2016, *A&A*, 590, A79
- Deacon, N. R., Schlieder, J. E., & Murphy, S. J. 2016, *MNRAS*, 457, 3191

- Delgado-Donate, E. J., Clarke, C. J., & Bate, M. R. 2003, *MNRAS*, 342, 926
- Delgado-Donate, E. J., Clarke, C. J., & Bate, M. R. 2004, *MNRAS*, 347, 759
- di Francesco, J., Evans, N. J., I., Caselli, P., et al. 2007, in *Protostars and Planets V*, ed. B. Reipurth, D. Jewitt, & K. Keil, 17
- Draine, B. T. 2006, *ApJ*, 636, 1114
- Dressing, C. D. & Charbonneau, D. 2013, *ApJ*, 767, 95
- Dunham, M. M., Arce, H. G., Mardones, D., et al. 2014, *ApJ*, 783, 29
- Dunham, M. M., Crapsi, A., Evans, II, N. J., et al. 2008, *ApJS*, 179, 249
- Dunham, M. M., Evans, N. J., Bourke, T. L., et al. 2010, *ApJ*, 721, 995
- Dupuy, T. J. & Kraus, A. L. 2013, *Science*, 341, 1492
- Enoch, M. L., Evans, II, N. J., Sargent, A. I., & Glenn, J. 2009, *ApJ*, 692, 973
- Epchtein, N., de Batz, B., Copet, E., et al. 1994, *APSS*, 217, 3
- Evans, II, N. J., Rawlings, J. M. C., Shirley, Y. L., & Mundy, L. G. 2001, *ApJ*, 557, 193
- Fadda, D., Jannuzi, B. T., Ford, A., & Storrie-Lombardi, L. J. 2004, *AJ*, 128, 1
- Fang, M., van Boekel, R., Wang, W., et al. 2009, *A&A*, 504, 461
- Ferguson, D. H. 1997, *ApJ*, 486, 987
- Fernández, M. & Comerón, F. 2001, *A&A*, 380, 264
- Fernández, M. & Comerón, F. 2005, *A&A*, 440, 1119
- Ferreira, J. 2013, in *EAS Publications Series*, ed. P. Hennebelle & C. Charbonnel, Vol. 62, 169–225
- Fitzpatrick, E. L. 1999, *PASP*, 111, 63
- Frank, A., Ray, T. P., Cabrit, S., et al. 2014, in *Protostars and Planets VI*, ed. H. Beuther, R. S. Klessen, C. P. Dullemond, & T. Henning, 451
- Frasca, A., Biazzo, K., Alcalá, J. M., et al. 2017, *A&A*, 602, A33
- Gaia Collaboration, Brown, A. G. A., Vallenari, A., et al. 2018, *A&A*, 616, A1
- Galván-Madrid, R., Liu, H. B., Izquierdo, A. F., et al. 2018, *ApJ*, 868, 39
- Geballe, T. R., Kulkarni, S. R., Woodward, C. E., & Sloan, G. C. 1996, *ApJ*, 467, L101
- Goldman, B., Marsat, S., Henning, T., Clemens, C., & Greiner, J. 2010, *MNRAS*, 405, 1140
- Gómez, G. C., Vázquez-Semadeni, E., Shadmehri, M., & Ballesteros-Paredes, J. 2007, *ApJ*, 669, 1042
- Goodwin, S. P. & Kroupa, P. 2005, *A&A*, 439, 565
- Goodwin, S. P., Whitworth, A. P., & Ward-Thompson, D. 2004a, *A&A*, 419, 543
- Goodwin, S. P., Whitworth, A. P., & Ward-Thompson, D. 2004b, *A&A*, 414, 633
- Greaves, J. S., Holland, W. S., & Pound, M. W. 2003, *MNRAS*, 346, 441

- Griffin, M. J., Abergel, A., Abreu, A., et al. 2010, *A&A*, 518, L3
- Grossman, A. S. & Graboske, H. C. 1973, *ApJ*, 180, 195
- Gullbring, E. 1994, *A&A*, 287, 131
- Hartigan, P., Edwards, S., & Ghandour, L. 1995, *ApJ*, 452, 736
- Hartmann, L., Herczeg, G., & Calvet, N. 2016, *ARA&A*, 54, 135
- Hayashi, C. & Nakano, T. 1963, *Progress of Theoretical Physics*, 30, 460
- Hennebelle, P. & Chabrier, G. 2008, *ApJ*, 684, 395
- Herczeg, G. J., Cruz, K. L., & Hillenbrand, L. A. 2009, *ApJ*, 696, 1589
- Herczeg, G. J. & Hillenbrand, L. A. 2008, *ApJ*, 681, 594
- Hester, J. J., Scowen, P. A., Sankrit, R., et al. 1996, *AJ*, 111, 2349
- Hildebrand, R. H. 1983, *Quarterly Journal of the Royal Astronomical Society*, 24, 267
- Hiranaka, K., Cruz, K. L., Douglas, S. T., Marley, M. S., & Baldassare, V. F. 2016, *ApJ*, 830, 96
- Hsieh, T.-H., Hirano, N., Belloche, A., et al. 2019, *ApJ*, 871, 100
- Hsieh, T.-H., Lai, S.-P., Belloche, A., & Wyrowski, F. 2016, *ApJ*, 826, 68
- Huard, T. L., Myers, P. C., Murphy, D. C., et al. 2006, *ApJ*, 640, 391
- Hubber, D. A. & Whitworth, A. P. 2005, *A&A*, 437, 113
- Huélamo, N., Bouy, H., Pinte, C., et al. 2010, *A&A*, 523, A42
- Huélamo, N., de Gregorio-Monsalvo, I., Palau, A., et al. 2017, *A&A*, 597, A17
- Ireland, M. J., Kraus, A., Martinache, F., Law, N., & Hillenbrand, L. A. 2011, *ApJ*, 726, 113
- Itoh, Y., Hayashi, M., Tamura, M., et al. 2005, *ApJ*, 620, 984
- Jayawardhana, R., Mohanty, S., & Basri, G. 2003, *ApJ*, 592, 282
- Joergens, V., Bonnefoy, M., Liu, Y., et al. 2013, *A&A*, 558, L7
- Joergens, V., Kopytova, T., & Pohl, A. 2012a, *A&A*, 548, A124
- Joergens, V., Pohl, A., Sicilia-Aguilar, A., & Henning, T. 2012b, *A&A*, 543, A151
- Jones, H. R. A., Longmore, A. J., Jameson, R. F., & Mountain, C. M. 1994, *MNRAS*, 267, 413
- Kauffmann, J., Bertoldi, F., Bourke, T. L., Evans, II, N. J., & Lee, C. W. 2008, *A&A*, 487, 993
- Kauffmann, J., Bertoldi, F., Bourke, T. L., et al. 2011, *MNRAS*, 416, 2341
- Kauffmann, J., Bertoldi, F., Evans, II, N. J., & C2D Collaboration. 2005, *Astronomische Nachrichten*, 326, 878
- Kausch, W., Noll, S., Smette, A., et al. 2015, *A&A*, 576, A78
- Khanzadyan, T., Gredel, R., Smith, M. D., & Stanke, T. 2004, *A&A*, 426, 171
- Kirkpatrick, J. D., Barman, T. S., Burgasser, A. J., et al. 2006, *ApJ*, 639, 1120

- Kirkpatrick, J. D., Kelly, D. M., Rieke, G. H., et al. 1993, *ApJ*, 402, 643
- Klein, R., Apai, D., Pascucci, I., Henning, T., & Waters, L. B. F. M. 2003, *ApJ*, 593, L57
- Koenigl, A. 1991, *ApJ*, 370, L39
- Kratter, K. M. & Murray-Clay, R. A. 2011, *ApJ*, 740, 1
- Kratter, K. M., Murray-Clay, R. A., & Youdin, A. N. 2010, *ApJ*, 710, 1375
- Kraus, A. L., Ireland, M. J., Cieza, L. A., et al. 2014, *ApJ*, 781, 20
- Kraus, A. L., Ireland, M. J., Martinache, F., & Lloyd, J. P. 2008, *The Astrophysical Journal*, 679, 762
- Krautter, J., Wichmann, R., Schmitt, J. H. M. M., et al. 1997, *Astronomy and Astrophysics, Supplement*, 123, 329
- Kumar, S. S. 1963, *ApJ*, 137, 1121
- Kuzuhara, M., Tamura, M., Ishii, M., et al. 2011, *AJ*, 141, 119
- Lafrenière, D., Jayawardhana, R., & van Kerkwijk, M. H. 2008, *ApJ*, 689, L153
- Lafrenière, D., Jayawardhana, R., & van Kerkwijk, M. H. 2010, *ApJ*, 719, 497
- Lamzin, S. A. 1995, *A&A*, 295, L20
- Larson, R. B. 1969, *MNRAS*, 145, 271
- Lee, C. W., Bourke, T. L., Myers, P. C., et al. 2009, *ApJ*, 693, 1290
- Lee, C. W., Kim, M.-R., Kim, G., et al. 2013, *ApJ*, 777, 50
- Levreault, R. M. 1988a, *ApJS*, 67, 283
- Levreault, R. M. 1988b, *ApJ*, 330, 897
- Li, Z.-Y. & Shu, F. H. 1996, *ApJ*, 468, 261
- Liebert, J. & Probst, R. G. 1987, *ARA&A*, 25, 473
- Liu, M. C., Najita, J., & Tokunaga, A. T. 2003, *ApJ*, 585, 372
- Lomax, O., Whitworth, A. P., & Hubber, D. A. 2016, *MNRAS*, 458, 1242
- Looper, D. L., Mohanty, S., Bochanski, J. J., et al. 2010, *ApJ*, 714, 45
- López Martí, B., Eisloffel, J., & Mundt, R. 2005, *A&A*, 440, 139
- Louvet, F., Dougados, C., Cabrit, S., et al. 2018, *A&A*, 618, A120
- Luhman, K. L. 2004, *ApJ*, 602, 816
- Luhman, K. L., Burgasser, A. J., & Bochanski, J. J. 2011, *ApJ*, 730, L9
- Luhman, K. L., Stauffer, J. R., Muench, A. A., et al. 2003, *ApJ*, 593, 1093
- Luhman, K. L., Wilson, J. C., Brandner, W., et al. 2006, *ApJ*, 649, 894
- Manara, C. F., Prusti, T., Comeron, F., et al. 2018, *A&A*, 615, L1
- Manara, C. F., Testi, L., Rigliaco, E., et al. 2013, *A&A*, 551, A107

- Manjavacas, E., Bonnefoy, M., Schlieder, J. E., et al. 2014, *A&A*, 564, A55
- Marocco, F., Day-Jones, A. C., Lucas, P. W., et al. 2014, *MNRAS*, 439, 372
- Martín, E. L. & Zapatero Osorio, M. R. 2003, *ApJ*, 593, L113
- Maury, A. 2011, in *EAS Publications Series*, ed. C. Charbonnel & T. Montmerle, Vol. 51, 191–209
- Mercer, A. & Stamatellos, D. 2017, *MNRAS*, 465, 2
- Merín, B., Jørgensen, J., Spezzi, L., et al. 2008, *ApJS*, 177, 551
- Meru, F. & Bate, M. R. 2010, *MNRAS*, 406, 2279
- Mohammadpour, M. & Stahler, S. W. 2013, *MNRAS*, 433, 3389
- Mohanty, S., Basri, G., & Jayawardhana, R. 2005, *Astronomische Nachrichten*, 326, 891
- Monin, J. L., Whelan, E. T., Lefloch, B., Dougados, C., & Alves de Oliveira, C. 2013, *A&A*, 551, L1
- Morata, O., Palau, A., González, R. F., et al. 2015, *ApJ*, 807, 55
- Motte, F., Andre, P., & Neri, R. 1998, *A&A*, 336, 150
- Murakami, H., Baba, H., Barthel, P., et al. 2007, *PASJ*, 59, S369
- Mužić, K., Scholz, A., Geers, V. C., & Jayawardhana, R. 2015, *ApJ*, 810, 159
- Mužić, K., Scholz, A., Geers, V. C., Jayawardhana, R., & López Martí, B. 2014, *ApJ*, 785, 159
- Muzerolle, J., Hartmann, L., & Calvet, N. 1998, *AJ*, 116, 455
- Muzerolle, J., Hillenbrand, L., Calvet, N., Briceño, C., & Hartmann, L. 2003, *ApJ*, 592, 266
- Muzerolle, J., Luhman, K. L., Briceño, C., Hartmann, L., & Calvet, N. 2005, *ApJ*, 625, 906
- Myers, P. C., Adams, F. C., Chen, H., & Schaff, E. 1998, *ApJ*, 492, 703
- Myers, P. C. & Ladd, E. F. 1993, *ApJ*, 413, L47
- Nakajima, Y., Tamura, M., Oasa, Y., & Nakajima, T. 2000, *AJ*, 119, 873
- Naranjo-Romero, R., Vázquez-Semadeni, E., & Loughnane, R. M. 2015, *ApJ*, 814, 48
- Natta, A. & Testi, L. 2001, *A&A*, 376, L22
- Natta, A., Testi, L., Alcalá, J. M., et al. 2014, *A&A*, 569, A5
- Natta, A., Testi, L., Comerón, F., et al. 2002, *A&A*, 393, 597
- Natta, A., Testi, L., Muzerolle, J., et al. 2004, *A&A*, 424, 603
- Natta, A., Testi, L., & Randich, S. 2006, *A&A*, 452, 245
- Naud, M.-E., Artigau, É., Malo, L., et al. 2014, *ApJ*, 787, 5
- Neuhäuser, R., Guenther, E. W., Wuchterl, G., et al. 2005, *A&A*, 435, L13
- Noll, S., Kausch, W., Kimeswenger, S., et al. 2014, *A&A*, 567, A25
- Offner, S. S. R., Lee, E. J., Goodman, A. A., & Arce, H. 2011, *ApJ*, 743, 91
- Oppenheimer, B. R., Kulkarni, S. R., Matthews, K., & Nakajima, T. 1995, *Science*, 270, 1478

- Ossenkopf, V. & Henning, T. 1994, *A&A*, 291, 943
- Padoan, P. & Nordlund, Å. 2002, *ApJ*, 576, 870
- Padoan, P. & Nordlund, Å. 2004, *ApJ*, 617, 559
- Palau, A., de Gregorio-Monsalvo, I., Morata, Ò., et al. 2012, *MNRAS*, 424, 2778
- Palau, A., Estalella, R., Ho, P. T. P., Beuther, H., & Beltrán, M. T. 2007, *A&A*, 474, 911
- Palau, A., Zapata, L. A., Rodríguez, L. F., et al. 2014, *MNRAS*, 444, 833
- Pascucci, I., Testi, L., Herczeg, G. J., et al. 2016, *ApJ*, 831, 125
- Pecaut, M. J., Mamajek, E. E., & Bubar, E. J. 2012, *ApJ*, 746, 154
- Perryman, M. A. C., Lindegren, L., Kovalevsky, J., et al. 1997, *A&A*, 323, L49
- Phan-Bao, N., Lee, C.-F., Ho, P. T. P., Dang-Duc, C., & Li, D. 2014, *ApJ*, 795, 70
- Phan-Bao, N., Lee, C.-F., Ho, P. T. P., & Tang, Y.-W. 2011, *ApJ*, 735, 14
- Phan-Bao, N., Riaz, B., Lee, C.-F., et al. 2008, *ApJ*, 689, L141
- Pilbratt, G. L., Riedinger, J. R., Passvogel, T., et al. 2010, *A&A*, 518, L1
- Pinte, C., Harries, T. J., Min, M., et al. 2009, *A&A*, 498, 967
- Pinte, C., Ménard, F., Duchêne, G., & Bastien, P. 2006, *A&A*, 459, 797
- Poglitsch, A., Waelkens, C., Geis, N., et al. 2010, *A&A*, 518, L2
- Pollack, J. B., Hubickyj, O., Bodenheimer, P., et al. 1996, *Icarus*, 124, 62
- Pound, M. W. & Blitz, L. 1995, *ApJ*, 444, 270
- Rafikov, R. R. 2007, *ApJ*, 662, 642
- Rayner, J. T., Toomey, D. W., Onaka, P. M., et al. 2003, *PASP*, 115, 362
- Rebolo, R., Martin, E. L., & Magazzu, A. 1992, *ApJ*, 389, L83
- Rebolo, R., Zapatero Osorio, M. R., & Martín, E. L. 1995, *Nature*, 377, 129
- Reipurth, B. & Clarke, C. 2001, *AJ*, 122, 432
- Ribas, Á., Bouy, H., Merín, B., et al. 2016, *MNRAS*, 458, 1029
- Ribas, Á., Espaillat, C. C., Macías, E., et al. 2017, *ApJ*, 849, 63
- Ricci, L., Isella, A., Carpenter, J. M., & Testi, L. 2013, *ApJ*, 764, L27
- Ricci, L., Testi, L., Natta, A., & Brooks, K. J. 2010a, *A&A*, 521, A66
- Ricci, L., Testi, L., Natta, A., et al. 2010b, *A&A*, 512, A15
- Ricci, L., Testi, L., Natta, A., Scholz, A., & de Gregorio-Monsalvo, I. 2012, *ApJ*, 761, L20
- Ricci, L., Testi, L., Natta, A., et al. 2014, *ApJ*, 791, 20
- Rigliaco, E., Natta, A., Testi, L., et al. 2012, *A&A*, 548, A56
- Rigliaco, E., Pascucci, I., Gorti, U., Edwards, S., & Hollenbach, D. 2013, *ApJ*, 772, 60

- Rilinger, A. M., Espaillat, C. C., & Macías, E. 2019, arXiv e-prints, arXiv:1905.05829
- Rodríguez, D. R., Zuckerman, B., Melis, C., & Song, I. 2011, *ApJ*, 732, L29
- Romero, G. A., Schreiber, M. R., Cieza, L. A., et al. 2012, *ApJ*, 749, 79
- Ruíz-Rodríguez, D., Cieza, L. A., Williams, J. P., et al. 2018, *MNRAS*, 478, 3674
- Rygl, K. L. J., Benedettini, M., Schisano, E., et al. 2013, *A&A*, 549, L1
- Sánchez-Portal, M., Marston, A., Altieri, B., et al. 2014, *Experimental Astronomy*, 37, 453
- Santamaría-Miranda, A., Cáceres, C., Schreiber, M. R., et al. 2018, *MNRAS*, 475, 2994
- Schmidt, T. O. B., Neuhäuser, R., Seifahrt, A., et al. 2008, *A&A*, 491, 311
- Scholz, A., Geers, V., Clark, P., Jayawardhana, R., & Muzic, K. 2013, *ApJ*, 775, 138
- Scholz, A., Jayawardhana, R., Muzic, K., et al. 2012, *ApJ*, 756, 24
- Scholz, A., Jayawardhana, R., & Wood, K. 2006, *ApJ*, 645, 1498
- Scholz, A., Jayawardhana, R., Wood, K., et al. 2007, *ApJ*, 660, 1517
- Scoville, N. Z., Sargent, A. I., Sanders, D. B., et al. 1986, *ApJ*, 303, 416
- Shang, Z., Brotherton, M. S., Wills, B. J., et al. 2011, *ApJS*, 196, 2
- Shirley, Y. L., Claussen, M. J., Bourke, T. L., Young, C. H., & Blake, G. A. 2007, *ApJ*, 667, 329
- Shu, F. H., Adams, F. C., & Lizano, S. 1987, *ARA&A*, 25, 23
- Sicilia-Aguilar, A., Kóspál, Á., Setiawan, J., et al. 2012, *A&A*, 544, A93
- Siringo, G., Kreysa, E., Kovács, A., et al. 2009, *A&A*, 497, 945
- Skrutskie, M. F., Cutri, R. M., Stiening, R., et al. 2006, *AJ*, 131, 1163
- Slesnick, C. L., Hillenbrand, L. A., & Carpenter, J. M. 2008, *The Astrophysical Journal*, 688, 377
- Smette, A., Sana, H., Noll, S., et al. 2015, *A&A*, 576, A77
- Stamatellos, D. & Herczeg, G. J. 2015, *MNRAS*, 449, 3432
- Stamatellos, D., Hubber, D. A., & Whitworth, A. P. 2007, *MNRAS*, 382, L30
- Stamatellos, D. & Whitworth, A. P. 2009, *MNRAS*, 392, 413
- Stutz, A., Launhardt, R., Linz, H., et al. 2010, *A&A*, 518, L87
- Tachihara, K., Dobashi, K., Mizuno, A., Ogawa, H., & Fukui, Y. 1996, *PASJ*, 48, 489
- Tamura, Y., Kawabe, R., Shimajiri, Y., et al. 2015, *ApJ*, 808, 121
- Tarter, J. 2014, in *Astrophysics and Space Science Library*, Vol. 401, 50 Years of Brown Dwarfs, ed. V. Joergens, 19
- Tarter, J. C. 1986, in *Astrophysics of Brown Dwarfs*, ed. M. C. Kafatos, R. S. Harrington, & S. P. Maran, 121–138
- Testi, L., Natta, A., Scholz, A., et al. 2016a, *A&A*, 593, A111

- Testi, L., Natta, A., Scholz, A., et al. 2016b, *A&A*, 593, A111
- Thies, I., Pflamm-Altenburg, J., Kroupa, P., & Marks, M. 2015, *ApJ*, 800, 72
- Tobin, J. J., Dunham, M. M., Looney, L. W., et al. 2015, *ApJ*, 798, 61
- Tobin, J. J., Hartmann, L., Bergin, E., et al. 2012, *ApJ*, 748, 16
- Tobin, J. J., Looney, L. W., Li, Z.-Y., et al. 2016, *ApJ*, 818, 73
- Tsukagoshi, T., Saito, M., Kitamura, Y., et al. 2011, *ApJ*, 726, 45
- Umehata, H., Tamura, Y., Kohno, K., et al. 2014, *MNRAS*, 440, 3462
- van der Plas, G., Ménard, F., Ward-Duong, K., et al. 2016, *ApJ*, 819, 102
- Vernet, J., Dekker, H., D'Odorico, S., et al. 2011, *A&A*, 536, A105
- Ward-Duong, K., Patience, J., Bulger, J., et al. 2018, *AJ*, 155, 54
- Ward-Thompson, D., André, P., & Kirk, J. M. 2002, *MNRAS*, 329, 257
- Ward-Thompson, D., Kirk, J. M., André, P., et al. 2010, *A&A*, 518, L92
- Whelan, E. T., Bonito, R., Antonucci, S., et al. 2014, *A&A*, 565, A80
- Whelan, E. T., Ray, T. P., & Bacciotti, F. 2009, *ApJ*, 691, L106
- Whelan, E. T., Ray, T. P., Bacciotti, F., et al. 2005a, *Nature*, 435, 652
- Whelan, E. T., Ray, T. P., Bacciotti, F., et al. 2005b, in *Protostars and Planets V Posters*, 8073
- Whelan, E. T., Ray, T. P., Comeron, F., Bacciotti, F., & Kavanagh, P. J. 2012, *ApJ*, 761, 120
- Whelan, E. T., Riaz, B., & Rouzé, B. 2018, *A&A*, 610, L19
- White, R. J. & Basri, G. 2003, *ApJ*, 582, 1109
- White, R. J. & Ghez, A. M. 2001, *ApJ*, 556, 265
- Whitworth, A. P. 2018, *Brown Dwarf Formation: Theory*, 95
- Whitworth, A. P. & Stamatellos, D. 2006, *A&A*, 458, 817
- Whitworth, A. P. & Zinnecker, H. 2004, *A&A*, 427, 299
- Wichmann, R., Krautter, J., Covino, E., et al. 1997, *A&A*, 320, 185
- Williams, J. P. & Cieza, L. A. 2011, *ARA&A*, 49, 67
- Wolff, S. G., Perrin, M. D., Stapelfeldt, K., et al. 2017, *ApJ*, 851, 56
- Wright, E. L., Eisenhardt, P. R. M., Mainzer, A. K., et al. 2010, *AJ*, 140, 1868
- Wu, Y.-L., Close, L. M., Males, J. R., et al. 2015a, *ApJ*, 801, 4
- Wu, Y.-L., Close, L. M., Males, J. R., et al. 2015b, *ApJ*, 807, L13
- Young, C. H. & Evans, II, N. J. 2005, *ApJ*, 627, 293
- Young, C. H., Jørgensen, J. K., Shirley, Y. L., et al. 2004, *ApJS*, 154, 396
- Zhou, Y., Herczeg, G. J., Kraus, A. L., Metchev, S., & Cruz, K. L. 2014, *ApJ*, 783, L17